UNIVERSITY OF CALIFORNIA,
IRVINE

Modeling membranes under stress: dynamics and disease

DISSERTATION

submitted in partial satisfaction of the requirements
for the degree of

DOCTOR OF PHILOSOPHY

in Mathematical, Computational and Systems Biology

by

Kathryn Manakova

Dissertation Committee:
Professor Jun Allard, Chair
Professor John Lowengrub
Professor Anna Grosberg
Professor German Enciso
Professor Michael Zaragoza

2018

TABLE OF CONTENTS

LIST OF FIGURES

LIST OF TABLES

ACKNOWLEDGMENTS

I would like to thank my advisor, Jun Allard, for sharing his passion for and knowledge of science with me for the last 5 years. Every meeting with him left me more confident, focused and excited about our work. I thank Huaming Yan, John Lowengrub, Mehrsa Mehrabi, Anna Grosberg, Michael Zaragoza, Yoichiro Mori, Rochelle Radzyminski, Vincent Boudreau, Jay Gatlin and Paul Maddox for fruitful collaborations. I thank my colleagues in the Allard lab who I am lucky to also call my friends. I thank the CCBS administrative staff, Karen Martin, Cely Dean and Naomi Carreon, for making all departmental and organizational tasks the easiest part of this dissertation. I thank my parents, Bruce and Vicky, for supporting every decision I ever made. I thank my husband, Sergei, for staying up with me through all the late nights, and my son, Maxim, for getting me out of bed each morning.

This work was supported in part by NSF CAREER Award DMS-1454739 to Jun Allard and an Opportunity Award from the Center for Complex Biological Systems to Mehrsa Mehrabi and myself.

Statement of co-authorship

Jun Allard[1,2,3] has been involved in the design, development and analysis of all the projects presented here through his guidance, feedback and technical assistance. In all projects, I have been involved in model development, performing simulations and analyzing results, writing all MATLAB scripts for Chapters 2-4.

In Chapter 2, a model of cellular blebbing, additional numerical solvers were written to include the effect of membrane bending rigidity and simulations performed by Huaming Yan[1] and John Lowengrub[1].

In Chapter 3, an analysis of traveling wave solutions, Yoichiro Mori[4] provided critical insight into the derivation of the non-local Maxwell condition and guidance throughout.

In Chapter 4, a model of nuclear shape, Mehrsa Mehrabi[5], Anna Grosberg[5] and Michael Zaragoza[6] assisted in model design, provided experimental data on cardiomyocytes with a variety of nuclear shapes feature variances and provided critical feedback.

In Chapter 5, a model of nuclear growth, I have presented the computational portion of a joint experimental-computational work posted in BioRxiv [7]. Experimental data was

[1] Department of Mathematics, University of California, Irvine
[2] Department of Physics, University of California, Irvine
[3] Center for Complex Biological Systems, University of California, Irvine
[4] School of Mathematics, University of Minnesota
[5] Department of Biomedical Engineering, University of California, Irvine
[6] Department of Pediatrics, School of Medicine, University of California, Irvine

obtained and analyzed by V. Boudreau[7], J. Hazel[8], J.K. Sellinger[7], P.Chen[8], H.G. Garcia[9,10], J. Gatlin[8] and P. Maddox[7]. Rochelle Radzyminski[2] and I developed the model, wrote scripts in MATLAB, performed numerical simulations and analyzed the results.

[7] Department of Biology, University of Northern Carolina at Chapel Hill
[8] Department of Molecular Biology, University of Wyoming
[9] Department of Physics, University of California, Berkeley
[10] Department of Molecular & Cell Biology, University of California, Berkeley

CURRICULUM VITAE

Kathryn Manakova

EDUCATION

Doctor of Philosophy in Mathematical, Computational and Systems Biology — **2018**
University of California, Irvine — *Irvine, California*

Master of Science in Mathematics — **2015**
University of California, Irvine — *Irvine, California*

Bachelor of Mathematics in General Mathematics — **2013**
University of Waterloo — *Waterloo, Ontario*

Bachelor of Science in Biology — **2010**
McGill University — *Montreal, Québec*

RESEARCH EXPERIENCE

Graduate Research Assistant — **2013–2018**
University of California, Irvine — *Irvine, California*

Undergraduate Research Assistant — **2012–2013**
University of Waterloo — *Waterloo, Ontario*

TEACHING EXPERIENCE

Teaching Assistant — **2014–2015**
Department of Mathematics, University of California, Irvine — *Irvine, California*

REFEREED JOURNAL PUBLICATIONS

K. Manakova, H. Yan, J. Lowengrub and J. Allard **2016**
Cell Surface Mechanochemistry and the Determinants of Bleb Formation, Healing, and Travel Velocity
Biophysical Journal; 110(7): 1636-1647

REFEREED CONFERENCE PUBLICATIONS

K. Scannell, A. Szymanska and Z. Nenadic **2014**
Intrinsic Dimensionality of Extracellular Action Potentials
Annual International Conference of the IEEE Engineering in Medicine and Biology Society.

A. Szymanska, M. Doty, **K. Scannell** and Z. Nenadic **2014**
A Supervised Multi-Sensor Matched Filter for the Detection of Extracellular Action Potentials
Annual International Conference of the IEEE Engineering in Medicine and Biology Society.

ABSTRACT OF THE DISSERTATION

Modeling membranes under stress: dynamics and disease

By

Kathryn Manakova

Doctor of Philosophy in Mathematical, Computational and Systems Biology

University of California, Irvine, 2018

Professor Jun Allard, Chair

Biological membranes are essential to life as we know it. One of the most important roles of membranes is to provide a stable barrier between two aqueous environments maintaining spatially localized chemical environments to facilitate the occurrence of biochemical reactions necessary for life. To accomplish this, membranes must remain stable under a variety of external and internal stresses. Thus, membranes are often structurally reinforced with networks of proteins or polysaccharides. Here, we present three models of metazoan membranes and their associated protein networks. We first investigated the plasma membrane, under which lies a dense network of actin filaments known as the cortex. Disruptions in the cortex lead to transient membrane protrusions known as blebs, which are implicated in a variety of cellular functions. Here, we developed a model which recapitulates the bleb life cycle and provides conditions under which blebbing occurs. Furthermore, our model can give rise to traveling blebs, a mysterious behavior observed in some cell lines, and predicts traveling velocity, which had not been established by other models. We derived a previously unknown necessary condition for traveling wave solutions to exist in such a system, and demonstrate sufficiency numerically. Next, we present two models of the nuclear envelope which is internally associated with a network of lamin proteins known as the nuclear lamina. In the first model, we investigated nuclear shape defects resulting from mutations in the gene encoding for lamin A/C, a major component of the nuclear lamina. Our model serves

as a pipeline to determine unknown biophysical properties, presented as parameters in the model, of the lamina. Our second model explored the scaling relationship between nuclear size and cell size. We combined equations for the transport of nuclear elements, including surface factor elements (*e.g.* lamins) and volume factor elements (*e.g.* NuMA), across the cell and into the nucleus with a mechanical force-balance equation establishing the size of the nucleus. This model predicts that nuclear size is regulated by a combination of surface factor and volume factor elements with a non-negligible contribution from genomic content.

Chapter 1

Introduction

Life as we know it could not exist without membranes. This is because membranes provide a spatially localized compartment to protect genetic information, and to enable the chemical and physical processes required to replicate the genetic information. Membranes are also involved in a number of biological processes including (but not limited to): establishing and maintaining chemical gradients across them (enabling the generation of energy); inter- and intra-cellular communication; and compartmentalizing biochemical reactions into organelles. (It is important to note that non-membrane bound organelles exist within both prokaryotic and eukaryotic cells, and are functionally analogous to membrane bound organelles [52]. Non-membrane bound organelles form through phase separation of particular proteins, and are often less stable than their membrane bound counterparts [101].) Biological membranes are hard to study because they are composed of a dynamic ensemble of lipids, proteins and surface carbohydrates all packed into a sheet less that 10 nm in width [89].

These membranes must support all these functions under the influence of many external stresses (Figure 1.1B), *e.g.* osmotic pressure due to changing water concentrations inside or outside the cell [114]. Thus, many membranes have structural support by association

with proteins networks on one or both sides (Figure 1.1C). This is a recurring feature in metazoans, whose plasma membrane is supported on the inside by a dense network of actin filaments known as the cortex, and whose inner membrane of the nuclear envelope is associated with a dense network of lamin filaments known as the nuclear lamina. These supporting protein networks are also constantly undergoing processes of assembly and disassembly as in Figure 1.1D. For instance, with every cell division the nuclear lamina must completely disassemble and then reassemble within the daughter cells. Improper regulation of assembly/disassembly kinetics can result in serious and fatal diseases such as progeria [94].

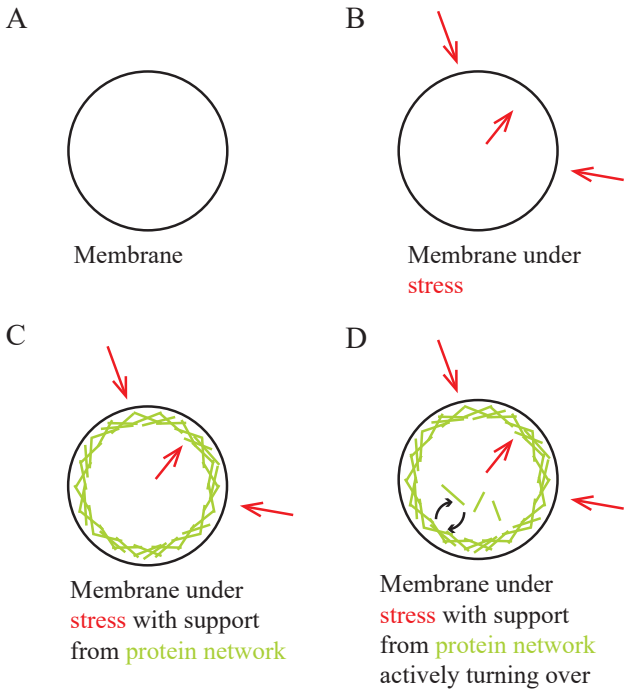

Figure 1.1: Membranes under stress.

In the following chapters, we treat the membrane as an elastic material [42] and use mathematical modeling to study the interplay between the chemical dynamics of assembly/disassembly of the proteins associated with membranes and the response of the membranes subjected to various mechanical forces. These models are developed at the molecular scale to recapitulate particular observations at the scale of the organelle and cell. By using the mathematical

tools of calculus developed over centuries, in conjunction with the computational advances of the last century, we are able to isolate the parts of the system we are interested in, *e.g.* membrane + associated protein complexes, without considering the system as a whole. In this way, we can identify the minimum number of elements necessary to describe a particular behavior of interest. In Chapters 2 and 5, we show how a model that is too simple fails to explain the observed behaviors, suggesting that something previously thought to be negligible is in fact important, and/or that something is missing in general. Mathematical modeling also allows us to use information that we know about a system, *e.g.* key biophysical parameters, to infer that which we are unable to obtain through laboratory experiments, as we do in Chapter 4. This provides an opportunity to identify the molecular origin of a difference observed at the scale of the cell or organism, *e.g.* the difference between a healthy *vs.* a pathological cell/organism. This dissertation is a presentation of four projects, each presented as a chapter, where we have developed biophysical models to investigate the mechanical responses of the plasma membrane of eukaryotic cells and the nuclear envelope of animal cells. Each project is briefly introduced by the following four paragraphs.

The cell membrane acts as the main barrier between the cell and the surrounding environment. Inside the cell of metazoans, the membrane is supported by a dense network of actin filaments called the cortex which is attached to the cell membrane via adhesion molecules. The cortex maintains the cell shape and contracts inward generating internal pressure in the cell. Local disruptions to the cortex result in dynamic, transient protrusions of the cell membrane termed blebs. Blebs are implicated in many cellular activities including apoptosis, mitosis and motility, yet little is known about the mechanism underlying bleb formation. One particular aspect which has received little attention is the traveling behavior of some blebs around the cell periphery, which may have implications in bleb based motility. In Chapter 2, we use mathematical modeling to elucidate the mechanisms underlying this behavior.

The equations arising from Chapter 2 are interesting in their own right, as little research

has been done for this class of non-local PDEs. More typical systems of equations arising in biological contexts, such as reaction-diffusion equations, have been studied extensively and many of their properties are well established. One such property is the existence of traveling wave solutions, which is known to be important to many biological processes [71]. In the case of reaction-diffusion systems, a necessary and sufficient condition which allows for traveling wave solutions is known. In our case of a non-diffusion like system, it is not. We believe the class of equations which our system falls into can and will be used to describe other biological systems in the future and so in Chapter 3, we describe an analog to this which will be applicable to a particular class of non-local PDEs.

A superficially similar problem to that of cellular blebs is seen in the nuclei of animal cells. Nuclei are bounded by a double membrane, and this double membrane is supported by a dense network of lamin filaments termed the nuclear lamina. In cases where the gene responsible for producing lamin A/C, the main constituent of the nuclear lamina, is mutated, a variety of disease states may ensue, including extremely severe diseases such as progeria and heart disease. The nuclei in these mutated cells often have a irregular shapes, with one or more protrusions termed nuclear blebs. In this case, the blebs are not due to a disruption in the linkage between the nuclear membrane and the lamina (as blebs contain lamina), but rather might be due to a defect in the lamina itself. The mechanism by which nuclear blebs form is unclear. In Chapter 4 we use mathematical modeling to probe potential defects in the lamin A/C protein, and work in conjunction with the Grosberg (UCI - Deparment of Biomedical Engineering) and Zaragoza (UCI - School of Medicine) labs to try to match simulated nuclei to their patient and control samples. This will elucidate the mechanism by which nuclear blebs form in disease states, and further our understanding of the disease itself.

Nuclei must be disassembled and reassembled with every cellular division, a process occurring throughout the lifespan of an organism. It has been previously shown that the final size of the

nucleus scales with cell size [50, 74], but the precise scaling relationship is unknown. Using a custom microfluidics device, our collaborators in the Maddox (UNC Chapel Hill) and Gatlin (University of Wyoming) have controlled for cell size and found that neither nuclear volume nor surface area scaled directly with cell size. In Chapter 5, we use a mathematical model of nuclear assembly to study the relative weights of the effects nuclear volume, nuclear surface area and genome size on the total nuclear size.

Finally, Chapter 6 includes general comments about the similarities and differences of each project, brief summaries and applications to other areas of mathematical and computational biology.

Chapter 2

Cell surface mechanochemistry and the determinants of bleb formation, healing and travel velocity*

2.1 Introduction

The eukaryotic cell surface is the site of cell-cell communication [3], cell-environment interactions including motility and mechanosensing [113], and cell morphogenesis [2], among other processes. Many of these processes involve mechanical forces and deformation, making mechanics of the cell surface an increasingly important topic of investigation.

The study of cell surface mechanics is complicated by dynamic interactions among its multiple constituents with distinct material properties. The plasma membrane is fluid [83] and resists deformation and experiences surface tension on the order of 10-100 pN/nm [97] that is spatially and temporally non-uniform [78]. Below the membrane is a $\sim 100\,\text{nm}$ layer of

*This work has been published in Biophysical Journal [Manakova et al. *Cell surface mechanochemistry and the determinants of bleb formation, healing, and travel velocity.* Biophys J, 110 (2016), pp. 1636-1647].

F-actin with distinct microarchitecture from the cytoplasmic F-actin further into the cell [19], termed the cortex. The cortex is anisotropic poro-viscoelastic material [86, 39] that generates internal active contractile stresses by association with myosin [97]. The membrane and cortex are decorated with a myriad of molecules, some of which interact with both of them, thereby facilitating dynamic adhesion between them [34]. This complexity obscures fundamental questions such as, how quickly is hydrostatic pressure propagated through the cortex [90, 18, 20], or surface tension propagated across the membrane [78, 31, 83]? These questions have functional consequences since, for example, membrane bending and tension are implicated in endocytosis [62], cell polarization [44] and motility [31, 110], while the cortex is implicated in cell division, initiating filopodia and other cellular protrusion [60], both facilitating and preventing vesicle export [105], and wound healing [86].

An example cell process that involves all the above components is offered by cellular blebbing, pressure-driven protrusions that occur in many cell types and conditions [14, 17, 76]. An individual bleb begins with an initiation phase whereupon the membrane separates from the cortex, either spontaneously or under experimental triggering such as laser ablation [19, 14]. Initiation is followed by a rapid ($\sim 10\,\mathrm{s}$) expansion phase which, unlike other cellular protrusion, is not actively driven by cytoskeletal polymerization [22]. After expansion, blebs can exhibit a range of dynamic behaviors: Stationary blebs heal in place with a slower timescale ($\sim$minutes). Other classes of bleb that have been experimentally observed travel around the periphery of the cell — a phenomenon termed circus movement [35, 75, 61] — or repeatedly bleb on top of an existing bleb [14]. The complete life-cycle is determined by a complex interplay between flow of cytosol into the bleb, contractile forces in the cortex and the formation and maintenance of membrane-cortex adhesions. Blebs are implicated in non-lamellipodial cell motility [63, 15], including in protease-inhibited cancer cells [33]; in maintaining homeostasis during division [87]; and have a speculated role in the origin of eukaryotic life [4].

Traveling waves of protrusion are increasingly reported in different cell types [44, 85], but these protrusions are typically F-actin-enriched (although see [51]), whereas blebs represent regions with reduced F-actin. A fundamental question to the understanding of any traveling wave phenomenon [2] is: what determines the traveling velocity of a traveling bleb? And, in the case of blebs which may be stationary or travel, even simultaneously at different locations on the same cell, what determines whether a bleb will travel or heal in place?

Several theoretical models of blebbing have been developed to capture various aspects of the process. Computational fluid dynamics models [90, 93, 111] have been developed to understand the initial expansion phase during which cytosolic fluid follows the protruding membrane. Due to the computational cost of solving the fluid equations along with their mechanical interaction with immersed structures (which typically have sub-second dynamics [90, 93]), simulations of these models are typically limited to 2D approximation and seconds timescales. Other researchers [61] have used force-balance models [1, 51] to obtain computationally tractable models describing the full life cycle. These models are in 2D and must assume an *a priori* bleb healing velocity to generate traveling blebs. Continuum analytical models [107, 106, 108] have also been developed that move beyond the typical small-deformation approximations typically used to describe membrane geometry. These models capture details of the shape of stationary bleb that have, among other findings, implicated lipid flow in determining bleb behavior.

A full, 3D description of the full life-cycle of traveling blebs is therefore lacking. In this work, we develop a model of local cell surface mechanics on timescales of seconds to minutes, thereby including cortex turnover and bleb healing. We exploit two simplifying assumptions: First, we assume hydrodynamic equilibrium is reached rapidly and therefore avoid computationally taxing fluid dynamic simulation, at the expense of losing information about the expansion phase. Second, our model contains a single, "effective" cortex corresponding to the weighted average of cortical actin, allowing us to include implicitly the cytoskeleton

further inside the cell.

An emerging feature of this model is that transient detachment between membrane and cortex can lead to: 1) rapid healing, 2) stationary bleb formation, and 3) spontaneous bleb travel, depending on model parameters. Our model makes two main contributions: First, since traveling blebs arise naturally, we can elucidate the determinants of bleb travel. In particular, several simplifying assumptions allow us to obtain an analytic expression for bleb travel velocity that provides experimentally-accessible perturbations predicted to accelerate or decelerate travel. Our second finding is that the biophysical ingredients hypothesized to account for blebbing produce traveling blebs with unrealistic geometry. This suggests yet-to-be-identified mechanism playing a role in cell integrity and the localization of morphological perturbations. We explore the influence of dynamic, non-uniform membrane tension; hydrostatic pressure equilibration occurring at multiple length scales (i.e., global versus local [93]); and spatial heterogeneity. We find the latter sufficient to maintain bleb compactness during travel.

2.2 Model

Our minimal model, summarized schematically in Figure 2.1, consists of four fundamental dynamic variables, as functions of time t and location on the two-dimensional cell surface, parametrized by (x_1, x_2). The actin cortex, has local height described by $y_C(x_1, x_2, t)$ measured normal to the mean cell surface from its steady-state configuration $y_C = 0$, and thickness $c(x_1, x_2, t)$. The cortical-cytoplasmic actin cytoskeleton can in principle have complicated morphologies that cannot be accounted for by a single location y_C, so we think of y_C as the weighted average position of maximal cortical actin. Membrane-cortex adhesions are described by density $a(x_1, x_2, t)$ in molecules/ nm^2. Finally, the membrane has local height $y_M(x_1, x_2, t)$. Note that our model is agnostic about the molecular constituents of the

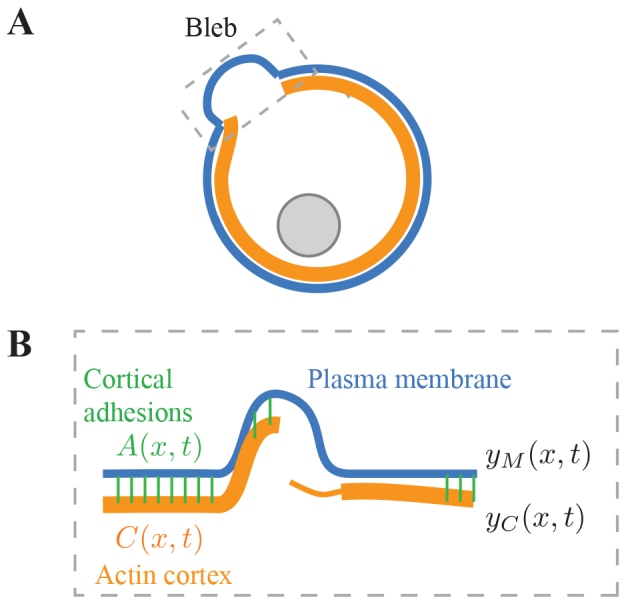

Figure 2.1: (A) Cartoon of a single bleb, with the plasma membrane depicted in blue and the cortex in orange. (B) Model components. At each location on the surface of the cell x, four quantities are represented: The height of the membrane $y_M(x,t)$, the height and thickness of the actin cortex $y_C(x,t)$ and $C(x,t)$ respectively, and the local density of membrane-cortex anchoring proteins, $A(x,t)$. Note that the schematic shows the range of possible model states (e.g., thick or thin cortex, protruding or proximal membrane), while specific predicted dynamics will be determined by simulation.

membrane, and it could include the plasma membrane as well as permanently membrane-associated proteins and cytoskeletal networks [51]. Our approach is similar to previous descriptions of membrane mechanics [1, 61, 3, 78].

2.2.1 Assembly and turnover.

The cortex is an active, anisotropic poro-viscoelastic material [86, 39]. Since the molecular details of cortex assembly are still under investigation [8], we assume simple first-order kinetics,

$$\frac{\partial c}{\partial t} = \omega a - rc. \tag{2.2.1}$$

The first parameter ω governs cortex assembly, and assumes new cortex requires adhesion to a nearby membrane (although existing cortex can exist anywhere), consistent with the observation that cortical actin has different architecture than cytoplasmic F-actin [19]. The second term describes cortex turnover with rate $r \sim 0.05\,\mathrm{s}^{-1}$ [34]. While we use the term thickness, we interpret c as a combination of density and spatial thickness, with fluorescence intensity of labeled F-actin serving as its experimental proxy. Therefore c has arbitrary units.

In stereotypical, pre-bleb conditions, the cortex is attached to the membrane via membrane-cortex adhesion molecules including ezrin- radixin- moesin (ERM) family proteins [34], as well as any other membrane proteins that interact with F-actin [77], therefore we use the generic term "adhesion" to describe their combined effect. We use similar first-order kinetics for adhesion assembly and turnover, with three additional assumptions: 1) Adhesion assembly saturates at high cortex thickness; 2) Adhesion attachment requires proximity between cortex and membrane, with characteristic distance δ that describes the "reach" of adhesion molecules, which may be as large as $\sim 100\,\mathrm{nm}$ [19]; and 3) Adhesion detachment is force-dependent with characteristic breaking force f_0. These assumptions lead to

$$\frac{\partial a}{\partial t} = \frac{k_{\mathrm{on}}\, c}{c_0 + c} \exp\left(-\left(\frac{y_M - y_C}{\delta}\right)\right) - k_{\mathrm{off}}\, a \exp\left(\frac{\kappa(y_M - y_C)}{f_0}\right) \tag{2.2.2}$$

where k_{on} and k_{off} have units of $\mathrm{nm}^{-2}\,\mathrm{s}^{-1}$ and s^{-1}, respectively, and c_0 is the cortex thickness at which adhesion assembly is half-maximal. The numerator $\kappa(y_M - y_C)$ follows from the assumption that adhesions collectively behave like springs with Hookean stiffness κ. Note that adhesion turnover $k_{\mathrm{off}} \sim 2\,\mathrm{s}^{-1}$ [34] is significantly faster than cortex turnover, leading to a separation of timescales we exploit.

2.2.2 Mechanics.

The above equations describing assembly and disassembly kinetics are coupled to a mechanical description of the membrane and cortex via mechanical energy,

$$E = \iint \mathcal{H}_1 + \mathcal{H}_M + \mathcal{H}_C \, dx_1 dx_2 \tag{2.2.3}$$

where

$$\mathcal{H}_1 = \frac{1}{2} a\kappa \left(y_M - y_C\right)^2 - \Pi. \tag{2.2.4}$$

The first term corresponds to tension on the adhesions. Since these adhesions break at moderate tension, we model these as linear springs. The second term is hydrostatic pressure Π, specified below. Membrane mechanics are described by

$$\mathcal{H}_M = \frac{1}{2} \, \gamma_M \left(\nabla y_M\right)^2 + \frac{1}{2} B_M \left(\nabla^2 y_M\right)^2 \tag{2.2.5}$$

corresponding to the standard Canham-Helfrich energy with membrane tension γ_M and bending rigidity B_M [42, 1, 106, 61]. These functional forms represent a small-deformation approximation and comprise a simplifying assumption to make the model more easily amenable to the analysis. We therefore do not expect our model to capture the shape of a fully-expanded bleb with high accuracy, for which geometrically more complex models have been developed [108]. Finally, mechanics of the actin-myosin cytoskeleton is included in

$$\mathcal{H}_C = c\sigma_m \left(y_C^2 + \frac{1}{2} \, w_C \left(\nabla y_C\right)^2 \right), \tag{2.2.6}$$

accounting for active of the cortex, which generates contraction stress $\sigma_m c$, assumed proportional to cortex thickness. The first term accounts for inward contractility, as the cortical cytoskeleton pulls against the cytoplasmic cytoskeleton, generating a normal (inwards) force,

as shown in Figure A.1. Note this term has been neglected in previous work [61]. The second term accounts for tangential stress in the plane of the cortex, where w_C is the cortex dimension that translates the 3D contractile stress to a tangential planar contractile tension. Importantly, we find that in traveling blebs, where the cortex is discontinuous, the tangential term does not generate sufficient inward force to heal the tail of the bleb as it travels, highlighting the importance of the normal contractility term. Cortex elasticity terms describing how the cortex resists deformation are straightforward to add, however we find that their omission is sufficient to explain our key results.

The mechanical features included in the energy equation 2.2.3 can also be understood by their equivalent force-balance form, 2.2.8-2.2.9 below.

Pressure propagation inside the complex rheology of the cytoplasm is under intense investigation [16, 90, 87]. To address the nature of pressure dynamics, we investigate several pressure model variants. As a base model, we assume pressure is locally relaxed when the membrane is allowed to relax,

$$\Pi = \hat{\Pi} \cdot \left(1 - \frac{y_M}{2y_M^0}\right)^2 \tag{2.2.7}$$

where y_M^0 sets the characteristic distance at which pressure is significantly reduced. The pressure drop would be lessened if the membrane is locally water-permeable [95], which would have the effect of reducing the coefficient relating pressure to membrane extrusion. Other model variants explore the possibility of rapidly-equilibrated pressure across the whole cell surface and a mixture of global and local pressure relaxation.

The dynamics of membrane tension are also under investigation [31, 80, 97, 44, 2]. Under the simplest assumption, membrane tension γ_M is spatially uniform and constant in time. We use this as our base model, but also explore membrane tension that is spatially non-uniform and dynamically responding to local stretching/unruffling and cortex attachment in 2.3.

Table 2.1: Model parameters.

Symbol	Dimensions	Meaning
ω	[A.U.] $\cdot\,\mathrm{s}^{-1}$	Cortex assembly rate constant
r	s^{-1}	Cortex turnover rate constant
k_{on}	$\mathrm{nm}^{-2}\,\mathrm{s}^{-1}$	Adhesion assembly rate
k_{off}	s^{-1}	Adhesion turnover rate
c_0	[A.U.]	Cortex thickness at adhesion saturation
δ	nm	Adhesion length between cortex and membrane
κ	pN/ nm	Adhesion spring constant
f_0	pN	Adhesion breaking strength
γ_M	pN/ nm	Membrane tension
B_M	pN nm	Membrane bending modulus
σ_m	Pa / [A.U.]	Actin-myosin contractility (per unit of c)
$\hat{\Pi}$	Pa/nm	Hydrostatic pressure scale

2.2.3 Preliminary analysis.

Taking the variational derivative of 2.2.3 leads to force-balance equations on the cortex and membrane,

$$0 = +a\kappa(y_M - y_C) - \sigma_m c y_C + \sigma_m c\, w_C \nabla^2 y_C \tag{2.2.8}$$

$$0 = -a\kappa(y_M - y_C) + \frac{\delta\hat{\Pi}}{\delta y_M} + \gamma_M \nabla^2 y_M - \beta\, \nabla^4 y_M \tag{2.2.9}$$

Physical parameters are summarized in Table 2.1. Values for many of these parameters have been estimated, see Figure A.1. The spatial terms significantly complicate both numerical solution and analysis of the model, and we find that their omission does not significantly influence blebbing dynamics. This is expected for membrane bending, since bending forces are expected to be negligible on length scales above $\sim (\beta/\gamma_M)^{(1/4)} \sim 100\,\mathrm{nm}$ [3]. Therefore, unless otherwise noted below, we neglect the tangential cortex stress $\nabla^2 y_C$ and membrane bending $\nabla^4 y_M$ terms. However, see Appendix A for solutions with full terms.

We nondimensionalize by choosing a characteristic actin cortex thickness, $C_c = c_0$, a characteristic density of adhesions, $A_c = k_{\mathrm{on}}/k_{\mathrm{off}}$, a characteristic time, $t_c = 1/r \sim 30\,\mathrm{s}$ [34], and

a characteristic position, $Y_c = y_M^0$, and a characteristic length by $x_c = \sqrt{2\gamma_M k_{\text{off}}/(k_{\text{on}}\kappa)} \sim 0.2\,\mu\text{m}$, resulting in a nondimensional model,

$$\frac{dC}{d\tau} = \Omega A - C \tag{2.2.10}$$

$$\epsilon\frac{dA}{d\tau} = \frac{C}{1+C}\exp\left(-\frac{Y_M - Y_C}{D}\right) - A\exp\left(\frac{Y_M - Y_C}{F_0}\right) \tag{2.2.11}$$

$$0 = A(Y_M - Y_C) - MCY_C \tag{2.2.12}$$

$$0 = -A(Y_M - Y_C) + P(1 - Y_M) + \frac{\partial^2 Y_M}{\partial \chi^2} \tag{2.2.13}$$

with six nondimensional parameters defined in Table 2.

Here we provide an overview of the roles of each term in 2.2.10-2.2.13. The first and second term in the C equation describe cortex formation and turnover, respectively. The first and second term in the A equation describe attachment and detachment of cortex-membrane adhesions. The first exponential in 2.2.11 arises because the membrane and cortex must be in proximity for an adhesion to form. The second exponential in 2.2.11 describes the accelerated breaking of adhesions under force. Then, 2.2.12 and 2.2.13 describe the mechanical balance between five forces acting on the membrane and cortex. The forces, in order of appearance, are: Adhesion force on the cortex; myosin contractility of the cortex; adhesion force on the membrane; pressure; and membrane tension.

Note that our choice of nondimensionalization means that only relative changes in Y_M and Y_C are physically meaningful. We numerically solve these equations as described in Appendix A [104].

Table 2.2: Nondimensional parameters.

Symbol	Definition	Interpretation
Ω	$\omega k_{\text{on}}/\gamma c_0 k_{\text{off}}$	Cortex intensity
ϵ	r/k_{off}	Ratio of adhesion and cortex turnover times
D	δ/y_M^0	Adhesion reach
F_0	$f_0/\kappa y_M^0$	Adhesion bond strength
M	$\sigma_m c_0 k_{\text{off}}/k_{\text{on}}\kappa$	Myosin contractility relative to adhesion strength
P	$\hat{\Pi} k_{\text{off}}/k_{\text{on}}\kappa$	Pressure relative to adhesion strength

2.3 Results

2.3.1 Model exhibits blebbing and non-blebbing behaviors.

The quantitative model combines five mechanisms of the membrane-cortex interaction: force-sensitive adhesions, local hydrostatic pressure, cortex contractility, membrane tension and cortex turnover. We numerically simulate the model and find three classes of dynamics arise from the same model at different parameters: Stable non-blebbing states, stationary blebbing, and traveling blebs. We discuss these in turn.

At equilibrium, the membrane and cortex are locally approximately flat. We apply an initial perturbation corresponding to local ablation by locally reducing the adhesion density by 99%. In blebbing states, the membrane will detach from the cortex and protrude locally. The membrane then continues to move away from the thinning cortex as the detached region grows in both lateral size (along the surface) and in height (i.e., normal to the cell surface) until it reaches a maximum size around $\tau = 1.75$. The adhesions subsequently accumulate under the protruding membrane and the cortex is able to re-attach and thicken. Under the influence of cortex contraction, the bleb heals and the membrane returns to its equilibrium. This bleb-like behavior is observed in 2D (Figure 2.2A left) and in 3D (Figure 2.2B) simulations. In contrast, at different biophysical parameters, the detached region of membrane may not grow after perturbation, but instead directly and rapidly return

to equilibrium, shown in Figure 2.2A right. This stable behavior is observed in both 2D (Figure 2.2A right) and in 3D (not shown).

2.3.2 Blebs as excitable phenomena

While numerical simulation of the full model reveals a range of blebbing behavior, we seek to elucidate how biophysical parameters determine the class of dynamics, specifically whether or not a bleb forms. To this end, we simplify the model by neglecting the tension term in 2.2.12. Heuristically, we model an (unrealistic) system in which a patch of cell surface has been cut off from its neighbors (as in Figure A.1). This transforms the force-balance equations 2.2.12-2.2.13 into a pair of algebraic equations,

$$Y_M = \frac{(A + CM)P}{AMC + AP + MCP} \tag{2.3.1}$$

$$Y_C = \frac{AP}{AMC + AP + MCP}, \tag{2.3.2}$$

shown in Figure 2.3A as a function of A and C. These are then substituted into the assembly/disassembly equations, yielding

$$\frac{dC}{d\tau} = \Omega A - C \tag{2.3.3}$$

$$\epsilon \frac{dA}{d\tau} = \frac{C}{1+C} \exp\left(-\frac{1}{D}\frac{MPC}{AMC + AP + MCP}\right) - A \exp\left(+\frac{1}{F_0}\frac{MPC}{AMC + AP + MCP}\right) \tag{2.3.4}$$

The model is now a system of two ordinary differential equations (ODEs) amenable to phase plane analysis [26]. We plot nullclines in which $dA/d\tau = 0$ (green) or $dC/d\tau = 0$ (orange) in Figure 2.3B,D. Four regimes of behavior are observed in this system: In one (top-left), there is a single stable equilibrium with no threshold behavior. In this regime, perturbations rapidly return to their steady state. We identify this with the stable non-blebbing behavior

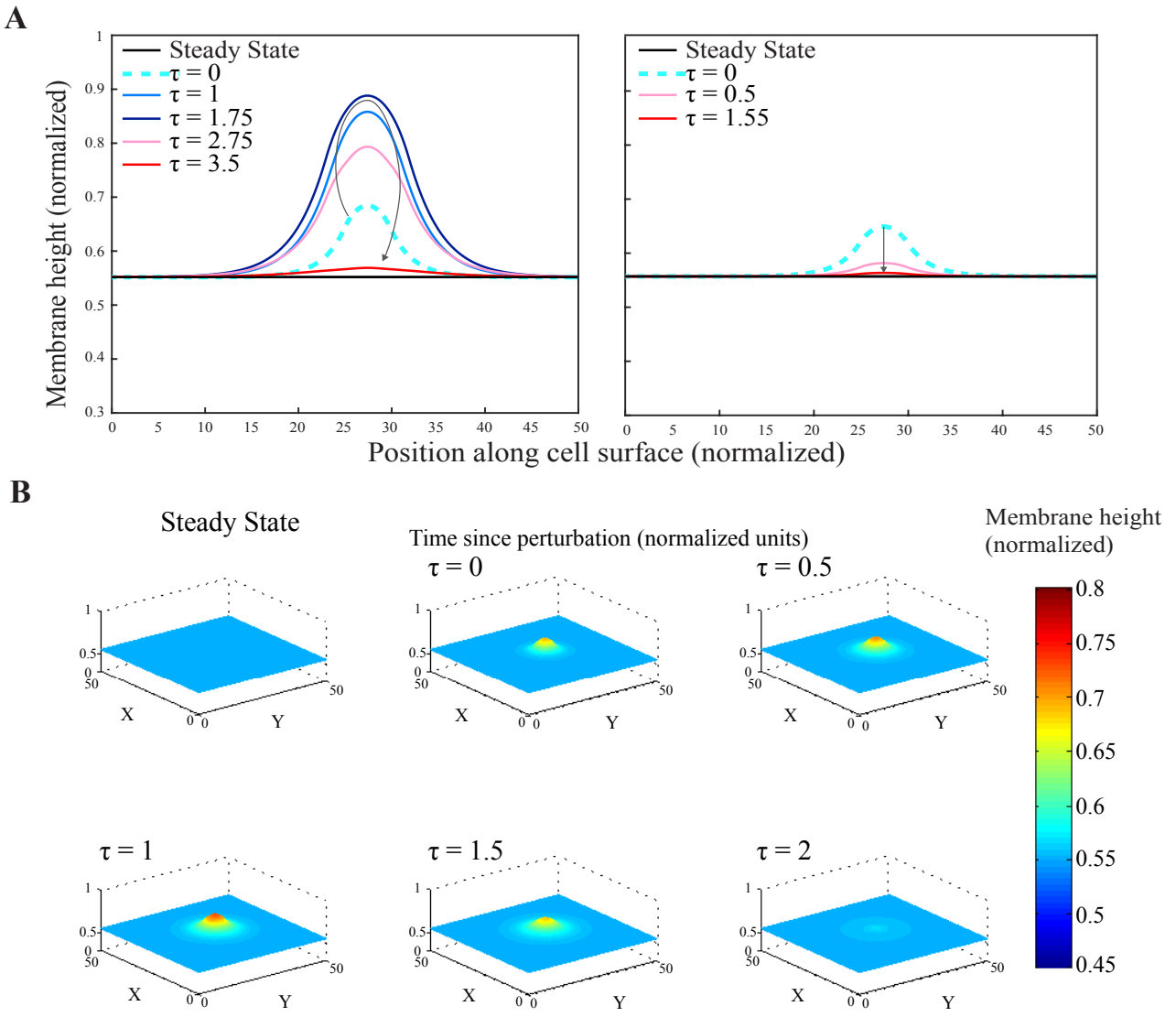

Figure 2.2: Model exhibits stationary blebs and non-blebbing states in 2D and 3D. (A) Profile of stationary solution of the 2D system: (Left) Excitable state in which an initial perturbation (cyan dashed) expands in both height (normal to cell surface) and laterally along cell surface before retracting. (Right) Non-excitable state in which the initial perturbation rapidly and directly returns to equilibrium. Parameter values: $\Omega = 40$, $\epsilon = 0.1$, $F_0 = 1$, $M = 0.007$, $P = 0.1$ and $D = 0.15$ for the excitable state, $D = 0.2$ for the non-excitable state. (B) Profile of stationary solution of the 3D system in an excitable state. Parameter values: $\Omega = 50$, $\epsilon = 0.1$, $F_0 = 1$, $M = 0.007$, $P = 0.1$ and $D = 0.15$. Note that our choice of nondimensionalization means that only relative changes in Y_M and Y_C are physically meaningful.

of the full model.

The stable equilibrium can exhibit excitability (bottom-left), a threshold phenomenon in which small perturbations rapidly return to the equilibrium, but a large sufficiently large perturbation results in a large, slow excursion in parameter space that eventually returns to the equilibrium. We identify this with blebbing behavior in the full model and is characterized by a fold in the $dA/d\tau$ nullcline.

One such excitation trajectory is shown in Figure 2.3C. Prior to the initial perturbation, $\tau < 2$, the flat surface is stable to small perturbations but susceptible to large perturbations such as the decrease in adhesion density applied here at $\tau = 2$. The membrane rapidly finds a new mechanical equilibrium, pushed out by hydrostatic pressure which is no longer in competition with cortical contraction. The comparatively slow timescale of cortical turnover (orange curve) leads to a delay before cortex begins to reform ($\tau \approx 4$), after which the cortex accumulates, pulling in the membrane. Note that many excitable trajectories exhibit low-amplitude oscillations in the cortex as it heals, corresponding to a slight "over-shooting" of the equilibrium ($\tau \approx 7$). Interestingly, such overshooting has been observed experimentally [19].

The minimum threshold to initiate an excitation can be extracted from Figure 2.3 as follows: The stable equilibrium is at the intersection of the two nullclines. From this point, removing adhesions corresponds to moving horizontally to the left. When adhesion removal is sufficient to cross the $dA/d\tau$ nullcline, an excitation is initiated. Since the $dA/d\tau$ nullcline determines this threshold, it is independent of membrane tension. This is in disagreement with previous estimates of the threshold, where membrane tension has been predicted to be a strong determinant of the size of initial ablation required for bleb initiation [17]. In contrast, our model predicts that membrane tension determines how big a bleb grows (laterally), but not whether it initially grows. This tension-independence arises heuristically because, once a patch of membrane has been de-adhered, membrane tension promotes bleb growth by

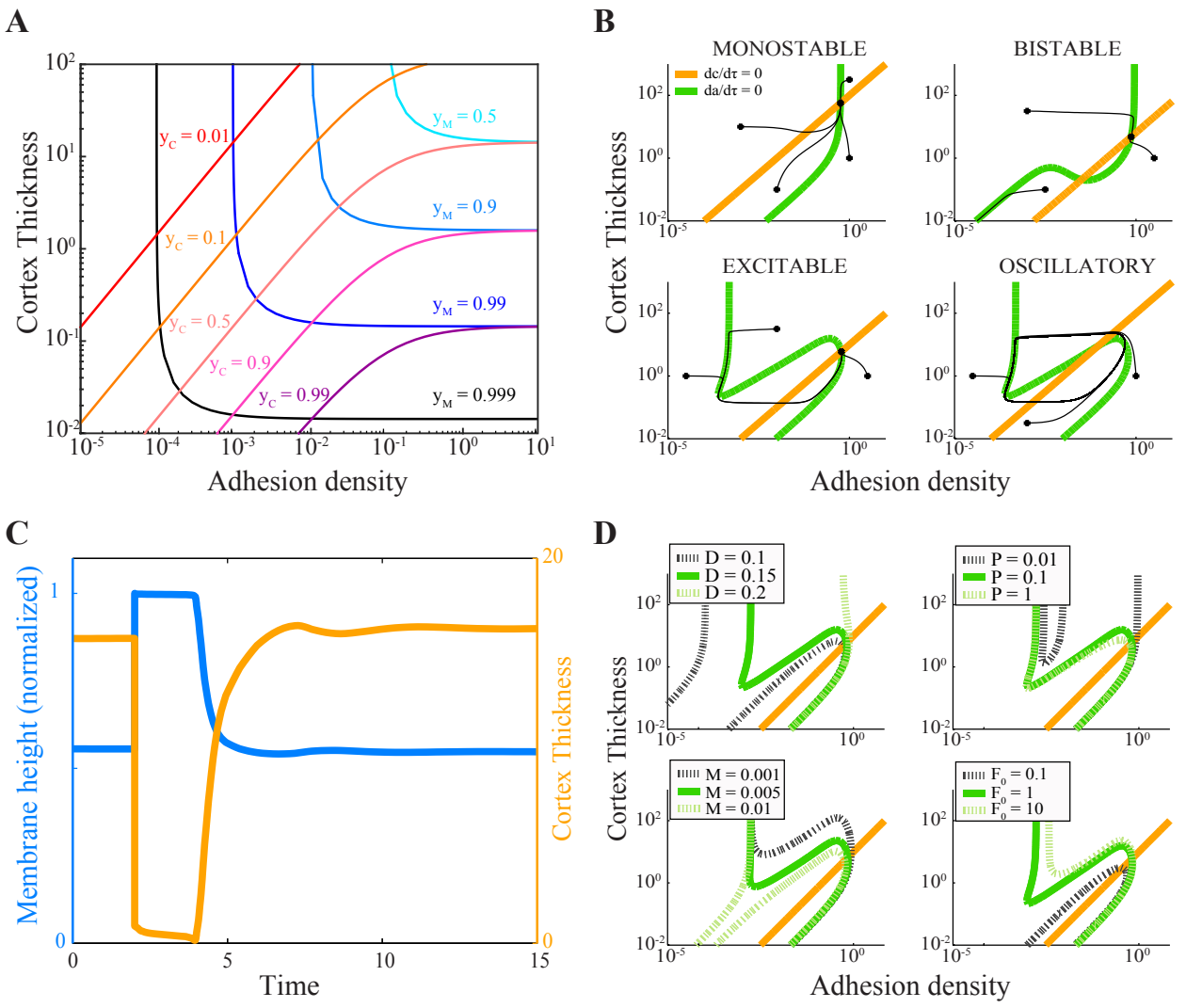

Figure 2.3: Emergence of blebbing states can be understood in terms of the local $A-C$ phase plane. (A) Since the model assumed force-balance between adhesions, cortex and membrane, a particular value of A and C determine the current position of the membrane and cortex y_M and y_C via 2.3.1-2.3.2. (B) Range of behaviors of the system of equations given different parameter sets visualized by the nullclines (orange for C and green for A) of the nondimensionalized system of equations, 2.3.4-2.3.3. Sample trajectories are shown in black. Monostable parameters: $\Omega = 100$, $\epsilon = 0.1$, $F_0 = 6.3$, $M = 0.09$, $P = 0.08$ and $D = 0.23$. Bistable parameters: $\Omega = 6.5$, $\epsilon = 0.1$, $F_0 = 2.9$, $M = 0.43$, $P = 0.016$ and $D = 0.19$. Oscillatory parameters: $\Omega = 100$, $\epsilon = 0.1$, $F_0 = 1$, $M = 0.007$, $P = 0.1$ and $D = 0.15$. Excitable parameters: $\Omega = 10$, $\epsilon = 0.1$, $F_0 = 1$, $M = 0.007$, $P = 0.1$ and $D = 0.15$. (C) Time series plot of membrane position (blue) and cortex thickness (orange) beginning in steady state, with a perturbation at time $\tau = 2.5$. (D) The effect of parameter variation on the nullclines. Parameters which are not being varied as indicted in legend are fixed as: $\Omega = 10$, $\epsilon = 0.1$, $F_0 = 1$, $M = 0.007$, $P = 0.1$ and $D = 0.15$.

pulling neighboring adhesions, and inhibits bleb growth by pulling in the de-adhered region. By the force-balance condition (2.2.9), these forces are equal.

We also observe oscillations (bottom-right), which could represent continually blebbing cells [14]. At yet other parameters, the same model exhibits bistable states (top-right) in which the flat, unperturbed equilibrium is stable, but is accompanied by a second state in which all adhesions are broken, and hydrostatic pressure is too great for the actin cortex to overcome, thus healing does not spontaneously occur. We expect this permanently-damaged state to not be observed experimentally as other cellular processes adjust to heal the cortex.

Thus, by observing the nullclines for different parameters, our model makes predictions about the emergence of blebbing following changes in biophysical parameters (Figure 2.3D). We summarize these predictions here and in Table A.1. Increasing the effective reach of adhesion molecules corresponds to increasing D, and abolishes excitability, while decreasing D is predicted to not abolish blebbing but extends the excitable trajectory, therefore predicting a slower healing period. Increasing hydrostatic pressure, *e.g.* by decreasing extracellular pressure by modulating osmolites, leads to emergence of blebbing from non-blebbing states, in agreement with experiment [97] and intuition. Decreasing myosin contractility abolished excitability, while increasing it delays healing.

2.3.3 Biophysical determinants of travel and travel velocity

The previous section's analysis predicts when the cell surface will be excitable and how the bleb evolves in height, but not its dynamics along the cell surface. To understand bleb travel, we return to the full, spatially-extended model first in 2D, then in 3D.

Excitable parameter sets all spread laterally. However, some parameter sets expand in a limited manner (Figure 2.2A), which we identify as stationary blebs, while others trigger

traveling pulses that persist, as shown in Figure 2.4A. We identify these as traveling blebs. In 2D, they move in both directions from the site of initial triggering. The time interval τ_{heal} from triggering and expansion to healing is equal to the healing time in the local analysis and is determined by the cortex turnover time $\tau_{\text{heal}} \sim 1/r$. The width of the traveling bleb w is thus determined by its travel velocity, $w \sim v\tau_{\text{heal}}$.

Traveling pulses are a generic feature of spatially-extended excitable systems [49, 84, 5]. In many cases, neighboring regions are coupled by the diffusion of a molecular participant. In these reaction-diffusion systems, a simple mathematical condition exists for determining whether an excitation will induce a traveling pulse or remain localized, sometimes called the Maxwell condition [9, 68]. Since our system is not a reaction-diffusion system, the Maxwell condition fails to predict whether the blebs travel or not.

A major goal of this work is to elucidate the determinants of the traveling velocity, which is known for reaction-diffusion waves and mechanical linear waves [2]. Parameter variations, shown in Figure 2.5, reveal that the parameter regime that allows traveling blebs is narrow in all nondimensional parameters except ϵ. Indeed, its relative range is less than $10^{0.3}$, corresponding to a 2-fold change. The model therefore predicts a nondimensional velocity $V \sim 1/\epsilon$, yielding the following dimensional velocity, the principle result of this work:

$$v \approx \sqrt{\frac{\gamma_M k_{\text{off}}^3}{\kappa k_{\text{on}}}}\, h(\Omega, D, F_0, P, M) \tag{2.3.5}$$

$$\approx \sqrt{\frac{\gamma_M k_{\text{off}}^3}{\kappa k_{\text{on}}}} \tag{2.3.6}$$

where the function h expresses to a weak dependence. We confirm this prediction in Figure 2.5B by performing a large pan-parametric search through parameter space. Equation 2.3.6 predicts that travel will accelerate with increasing membrane tension, with a specifically square-root dependence, and will decelerate with adhesion formation rate k_{on}, a parameter that could be varied by increasing the abundance of total adhesion molecules.

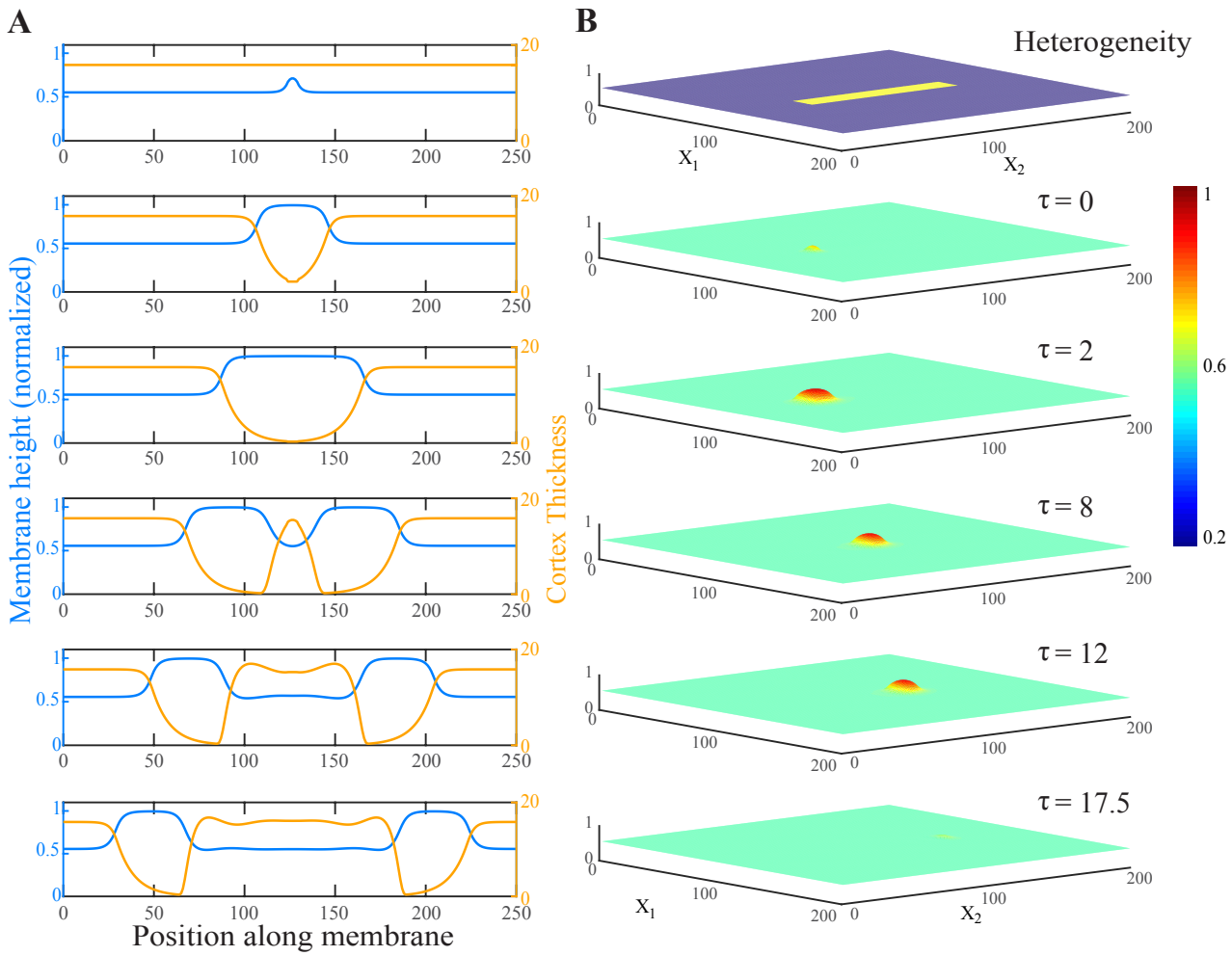

Figure 2.4: Traveling blebs in 2D and 3D. (A) Profile of a traveling blebs in 2D after a perturbation at time $\tau = 0$. Membrane height in blue, cortex thickness in orange. Parameter values: $\Omega = 55$, $\epsilon = 0.1$, $F_0 = 1$, $M = 0.007$, $P = 0.1$ and $D = 0.15$. (B) Profile of a traveling bleb in 3D after a perturbation at time $\tau = 0$ in the spatial-heterogeneity hypothesis model as shown in top panel, see Results.

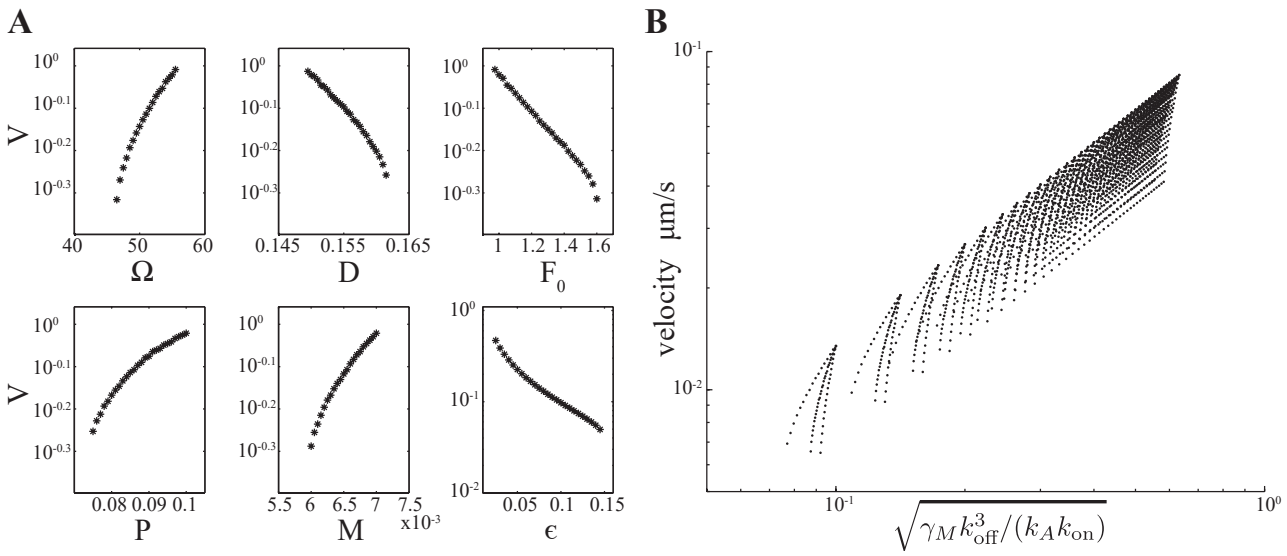

Figure 2.5: Velocity of traveling blebs. A) Plot of each of the 6 nondimensional parameters, Ω, D, F_0, P, M, ϵ, versus nondimensional velocity. Parameter ranges show the full extent of the parameter regime exhibiting traveling solutions. Fixed parameters in each plot are: $\Omega = 55$, $\epsilon = 0.1$, $F_0 = 1$, $M = 0.007$, $P = 0.1$ and $D = 0.15$. (B) Plot of hypothesized relationship between velocity, 2.3.6, versus velocity observed in numerical simulation.

The affinity of adhesions for the cortex, $K_A \equiv k_{\rm on}/k_{\rm off}$, is also predicted to have a decelerating influence on bleb travel. Interestingly, all other parameters, including hydrostatic pressure and myosin contractility, are predicted to have only a minor influence on travel velocity. Note, however, that these parameters strongly determine whether or not a bleb can form, and whether or not the bleb travels laterally. This model prediction is distinct from a previous prediction [61], which posited that cortex healing has an intrinsic velocity, and that this velocity determines bleb travel velocity.

2.3.4 Hypotheses for compact traveling blebs

In 3D, the base model also exhibits excitations that either travel or heal in place, in agreement with the local analysis and 2D model. Parameter conditions for excitability and travel are the same as for the 2D model, as is travel velocity. However, we find that a localized

initial perturbation spreads radially in all directions, leading to an expanding bull's-eye or target pattern, Figure 2.6B. This is a generic feature of excitable systems and arises because of inherent symmetry: a protruding region of membrane will pull neighboring regions of membrane, without directional bias.

Since traveling blebs are not experimentally observed to expand in bull's eye patterns, we are led to investigate the question of what gives rise to spatially compact traveling blebs? That is, what breaks the symmetry, inducing travel in a single direction?

We introduce three hypotheses. The first is that hydrostatic pressure may be reduced globally fast enough that, once the excited region enlarges past a certain size, there is no longer sufficient pressure to drive further excitation, thus limiting the target pattern to a compact region. In our model, we modify the membrane force-balance equation, 2.2.9, by including the pressure term

$$\Pi = \hat{\Pi} \cdot \iint \left(1 - \frac{y_M}{2y_M^0}\right) dx_1 dx_2. \tag{2.3.7}$$

This equation corresponds to a shared, global pressure that responds to pressure release (via membrane protrusion) instantly anywhere in the domain. We variously simulated purely global pressure, purely local pressure, and pressure with both local and global equilibration, following recent theoretical evidence [91].

We find that global pressure dynamics can limit the bleb's outward growth when $\hat{\Pi}$ is sufficiently large. However, we do not see symmetry breaking, even upon introduction of 10% parametric noise (Figure 2.6A). Interestingly, at intermediate global pressures, the bleb does not heal and instead undergoes slow oscillations (Figure 2.6A right). These oscillations reveal an inherent negative feedback between cortical formation, which builds pressure, which in turn breaks adhesions, weakening the cortex.

The second hypothesis is that bleb compactness and asymmetry is due to a dynamic, non-uniform membrane tension. Following recent evidence [80], we introduce the assumption that tension increases with increasing local cortical actin contractility,

$$\gamma_M = \gamma_{M0} + \gamma_{M1} C. \tag{2.3.8}$$

We find that this is sufficient to terminate the protrusion (Figure 2.6B), but, again, do not observe symmetry breaking.

Our third hypothesis is that large-length-scale heterogeneity, specifically on the $\sim$ micron length scale of blebs, exists in the local density of proteins such as adhesion molecules and cortical actin nucleators. These manifest as spatial heterogeneity in model parameters such as D and Ω. Since these parameters sensitively determine whether the bleb can travel, such heterogeneity might create specific paths, forcing traveling blebs from spreading in all directions. We simulate the model on a surface in which a small rectangular region has distinct parameters from its surrounding region, as shown in Figure 2.4B top. Since the parameter region allowing traveling blebs is fairly narrow (Figure 2.5), it is straightforward to find parameter sets with less than 2-fold variation for which the equilibrium is the same, but only one allows travel. As expected, blebs initiated in the excitable-travel region remain compact and move with velocity v from 2.3.6, and front-to-back width $w \sim v\tau_{\text{heal}}$.

We conclude that small differences across large length scales in the underlying biophysical properties of the cell surface are sufficient to explain compact traveling blebs. This hypothesis makes the prediction that subsequent traveling blebs will tend to occur in the same location on the cell surface, provided that the heterogeneity's own timescale of variation is longer than the bleb lifetime.

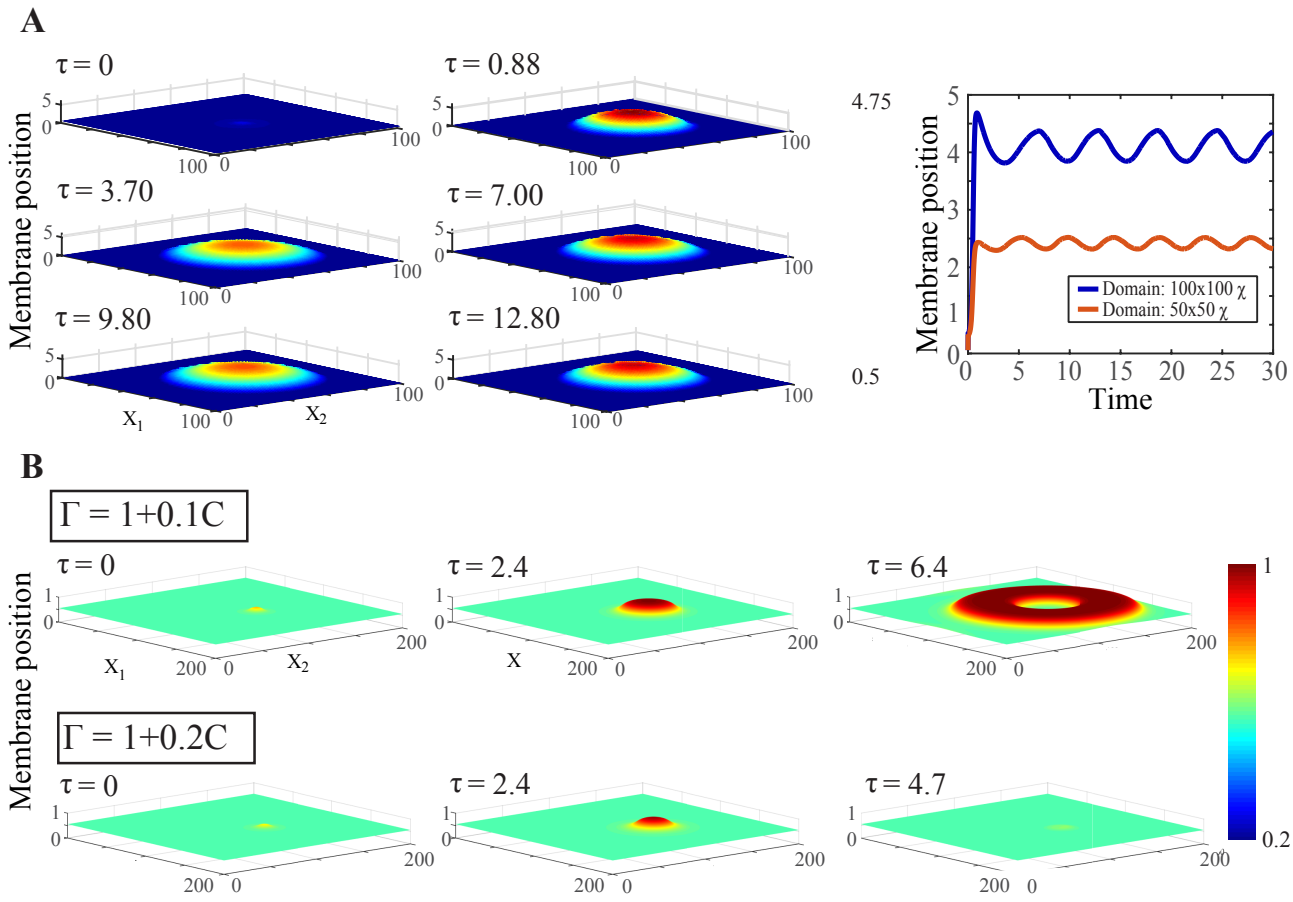

Figure 2.6: Alternative hypotheses for hydrostatic pressure and membrane tension dynamics. (A) Profile of 3D bleb using the global pressure model, 2.3.7, which assumes pressure equilibrates instantaneously across the domain. The bleb expands and contracts in oscillatory cycles (right panel). (B) Profile of a 3D bleb using a non-uniform tension model, 2.3.8, which assumes membrane tension depends on to the cortex thickness at a given point on the membrane. As the strength of this dependence increases (bottom row), the bleb no longer travels across the membrane. Here, $\Gamma = \gamma/\gamma_0$ is the nomdimensionalized membrane tension.

2.4 Discussion

Excitability is a recurrent theme in cell biology [47, 109, 30, 5]. We find that the conditions for excitability emerge naturally from the mechanical properties of the cell surface, namely: the combination of a contractile cortex, a membrane exposed to internal hydrostatic pressure, and force-sensitive adhesions connecting them. In addition, membrane mechanical properties (i.e. surface tension) are sufficient for this excitability to lead to either limited-growth stationary blebs that heal in place, or traveling blebs reminiscent of circus movement. Notably, three classes of dynamics arise from the same model at different parameters: Stable, non-blebbing states (Figure 2.2B), stationary blebbing (Figure 2.2A,C); and traveling blebs (Figure 2.4A,B). Thus our model provides quantitative conditions for bleb growth and whether the bleb heals locally or travels.

The model makes two main contributions. First, it allows elucidation of the determinants of the travel velocity in terms of biophysical parameters such as membrane tension and adhesion kinetics, 2.3.6. Surprisingly, we find that hydrostatic pressure and myosin contractility only weakly determine velocity, while strongly determining other features such as whether the bleb forms, and its height. This is in distinction to previous assumptions [61] and other traveling waves in biology [2].

Our second finding is that known biophysical mechanisms are insufficient to account for the compactness of traveling blebs in 3D. The excitability inherent in the system leads to traveling waves. However, a striking distinction from other excitable waves on a two dimensional domain is that other waves create bull's eye patterns or spiral patterns. Since local membrane-cortex detachment promotes nearby detachment symmetrically, why do blebs travel in a compact shape, rather than spreading in all directions? Generically, for a shape to remain approximately constant as it travels, the normal velocity on its perimeter must vary from maximal at its front to zero at its sides. This observation, termed the Graded

Radial Extension condition [59], was stated for steady cell motility but holds in general and therefore must be true for compact traveling blebs. One hypothesis we find sufficient to maintain compact travel is heterogeneity in the biophysical properties of the cell surface, such as adhesion density. There is no direct evidence that such heterogeneity is responsible for determining bleb travel paths, and it is likely that other mechanisms can explain compact travel. Since membrane tension is a strong determinant of local expansion velocity, it is possible that a model including different non-uniform membrane tension can recover a compact bleb in the absence of parametric heterogeneity. Other alternatives are: constraints set by lipid flow through the neck of the bleb [83], or nematic ordering in the cortex [51], which would break isotropic symmetry. For cells adhered to a rigid surface, the curvature is higher at the cell perimeter. This higher curvature could also potentially bias bleb formation and travel. We anticipate these will be a future direction of research.

A crucial feature of our model is the presence of a normal stress generated by the cortex, in addition to tangential stresses. We find that this normal stress is necessary for the dynamic healing and retraction of a traveling bleb. If myosin in the cortex generates an isotropic contractile stress, then it will induce stress in any direction in which there is F-actin. There is significant F-actin beneath the cortex (around 60% of the density in the cortex [19]), which is referred to as the cytoplasmic actin network and plays a role in cell integrity [64]. Our results suggest it also plays a role in retracting cellular protrusions.

The rheology of the cytoplasm, which determines how pressure propagates, is under intense investigation. Our model assumes a particular relationship between pressure change and volume change. To be as faithful to the correct rheology as possible, in 2.3 we simulate two extremes. Either (1) pressure relaxes entirely locally, with pressure at nearby locations unchanged, except perhaps on longer timescales if the bleb doesn't retract, *i.e.*, pressure is local on short timescales, as described by our model (2.2.7). Or, (2) pressure relaxation spreads rapidly, and it nearly equal everywhere following blebbing, *i.e.*, pressure is global on

short timescales, as described by our model (2.3.7). Recent computational models of detailed cell rheology [91] demonstrate a more complicated possibility. Assuming the cytoplasm is poroelastic [18, 65], they find that, following blebbing, there is a small global drop in pressure, but full global equilibration is significantly slower. In the language of our model, this means that, on the $\sim 1\,\mathrm{s} - 10\,\mathrm{s}$ timescale we consider, part of the pressure drop is local and part is global. We may therefore be interested in a part-local, part-global pressure model. In Appendix A, we consider pressure models in which local membrane protrusion leads to both local and global pressure drops. We find that pressure must be at least partly local, *i.e.*, that neighboring regions are not equilibrated as quickly as at the site of protrusion, for blebbing to arise. As the global pressure drop is increased (corresponding to the assumption that the cytoplasm is less poroelastic and more like an incompressible fluid), the simulation approaches the purely global pressure model shown in Figure 2.6A.

Increasingly, mechanics is included in theoretical models of cellular processes [77, 96, 78, 24, 81]. In these cases and others, subcellular mechanics equilibrates on sub-second timescales but drives processes that play out over seconds or slower, therefore mechanics is included via instantaneous force-balance or, equivalently, minimization of an energy functional as in 2.2.3 at every moment in time. Instead of reaction-transport (diffusion or advection) partial differential equations, these models can be expressed as a boundary value problem at each moment in time coupled to local time-dependent governing equations. This distinct class of models presents new opportunity for mathematical development. For excitable reaction-diffusion systems, a straightforward condition termed the Maxwell condition [68, 9, 72] can be computed that determines whether the excitation will generate traveling waves. Analogous conditions for the new class of mechanical models exist, and are the subject of the next chapter.

Our model makes several testable predictions about how bleb behavior will be modulated by experimental perturbations. The specific predictions about bleb formation and travel

velocity, in Results, correspond to changes in hydrostatic pressure, which can be modulated via the extracellular pressure by, *e.g.*, osmolites; Cortical turnover, which can be promoted or slowed by jasplakinolide or cytochalasin-D [19, 87]; Myosin contractility, which in blebs has been demonstrated to be susceptible to blebbistatin and indirectly to Y-compound [97]. In addition to these experiments, our model predicts that the "reach" of the adhesion molecules, δ, influences bleb characteristics via the (nondimensional parameter D). It might be possible to modulate this parameter by mutagenically elongating or truncating cortex-membrane adhesion molecules.

In addition to the model variants we explored here, this model is readily extendable to different surface geometries and assumptions about stresses below and above the cell surface. An intriguing direction of research is the coupling of the present model of surface mechanochemistry with different rheological models of how stress evolves inside the cell [91, 18]. Another direction is the coupling to extracellular fluid dynamics, which have recently been proposed to play a role in determining membrane dynamics, even on slow ($\sim 1\,\mathrm{s}$) timescales [12].

Chapter 3

Analysis of traveling waves in a non-local model of cell surface mechanics*

3.1 Introduction

Reaction-diffusion equations are used to describe many phenomena. They are of particular importance to the field of mathematical biology, and have been used to study pattern development [98] and the emergence of periodic structures from non-periodic sources during embryogenesis [55]. Because of a long history and extensive applications, mathematical studies have revealed the conditions for various spatiotemporal patterns to arise.

The inclusion of biomechanics to chemical kinetic frameworks naturally leads to non-diffusion PDEs. In particular, the separation of time scales between typical mechanical equilibration

*with Y. Mori and J. Allard

(often sub-second) and chemical dynamics (often on seconds timescale) allows a system, where all interactions are fundamentally local, to be approximated with a non-local model [58]. This principle was used by us in Chapter 2 to model the phenomenon of cellular blebbing.

Here we are studying a type of non-local PDE resulting from mechanical constraints in conjunction with chemical dynamics. In particular, we have chosen to investigate the conditions under which traveling wave solutions arise. We speculate that this phenomenon is relevant to a larger class of equations arising in cellular biophysics. We establish a non-local analogue of a mathematical condition previously established in reaction-diffusion systems and sometimes called the Maxwell condition [10, 67].

3.2 Statement of model

The model is derived in Chapter 2, and therefore will not be repeated here. I will simply remind the reader that a particular choice of nondimensionalization results in the following system:

$$\frac{dc}{dt} = \Omega a - c \tag{3.2.1}$$

$$\epsilon \frac{da}{dt} = \frac{c}{1+c} \exp\left(-\frac{y - y_C}{D}\right) - a \exp\left(\frac{y - y_C}{F}\right) \tag{3.2.2}$$

$$0 = a(y - y_C) - M c y_C \tag{3.2.3}$$

$$0 = -a(y - y_C) + P(1 - y) + \epsilon^2 \frac{\partial^2 y}{\partial x^2}. \tag{3.2.4}$$

Note that for ease of reading we have deliberately abused notation by using slightly different variables than in Chapter 2. For a detailed description of the scales used for nondimension-

alization, see Chapter 2.

3.2.1 Connections to a larger class of models arising in cell mechanics

As previously mentioned, mechanical equilibration is fast compared to the chemical kinetics of the system and as a such, we are not explicitly modeling the dynamics of mechanical equilibration, which would involve hydrodynamic effects [92] on microsecond or millisecond timescales. A consequence of this method is that our resulting system includes non-local interactions. Non-local formulations are useful to biologists for a number of reasons and may provide even greater insight into the variables of interest, and they are often easier to solve numerically as in Lee et al. [58]. In Mogilner and Edelstein-Keshet [66], the authors used non-local interactions to describe how a group of individuals can migrate together in a swarm or a flock, a behavior which was not observed with traditional population models which considered only local interactions. Several other single-species ecological population models have incorporated non-local effects including Gourley et al. [37], Yu and Chen [112]. Edward and Mathematical [27] extends the Mogilner and Edelstein-Keshet [66] model to describe the non-local interactions between two cell populations. Lee et al. [58] showed that a non-local interaction model is suitable to describe the behavior of the chemotactic systems, when the associated chemical(s) diffuse much more rapidly than the cells. Incorporating non-local interactions into a mathematical model has the effect of turning a system of PDEs into a single (or system of) integro-PDE(s).

3.3 Non-spatial system

Numerical simulation of the full, spatial, model reveals a range of blebbing behavior as in Chapter 2. In this section, we seek to elucidate how biophysical parameters determine the regime of behavior. To this end, we simplify the model by neglecting the tension term in (3.2.4). This transforms the force-balance equations (3.2.3)-(3.2.4) into a pair of algebraic equations,

$$y = \frac{(a + cM)P}{aMc + aP + McP} \tag{3.3.1}$$

$$y_C = \frac{aP}{aMC + aP + McP}. \tag{3.3.2}$$

These are then substituted into the assembly/disassembly equations, yielding

$$\frac{dc}{dt} = \Omega a - c \tag{3.3.3}$$

$$\epsilon \frac{da}{dt} = \frac{c}{1+c} \exp\left(-\frac{1}{D}\frac{MPc}{aMc + aP + McP}\right) - a \exp\left(+\frac{1}{F}\frac{MPc}{aMc + aP + McP}\right). \tag{3.3.4}$$

The model is now a system of two ODEs amenable to phase plane analysis [26].

3.3.1 Regimes of behavior at small ϵ

We ran simulations of this non-spatial system using MATLAB's `ode45` and `ode23` (for $\epsilon < 0.01$) differential equation solvers. We found that for $\epsilon \ll 1$, the system is capable of exhibiting four different states which are qualitatively different. There is a monostable regime, where the system returns to steady state immediately upon perturbation. Upon changing parameters, the system can exhibit a bistable regime where two stable steady states are separated by an unstable steady state. The presence of a stable limit cycle characterizes

the oscillatory regime. Finally, there is a second monostable regime which we term the "excitable" regime. In this case the system returns to the original steady state after perturbation and so is in fact another monostable state, but rather than returning immediately, the solution initially travels away from the steady state. Phase plane diagrams with sample trajectories for each of these regimes are shown in Figure 3.1A, and time series for the variables $a(t)$ and $c(t)$ are plotted in Figure 3.1B. It is the excitable regime which is associated with the blebbing behavior.

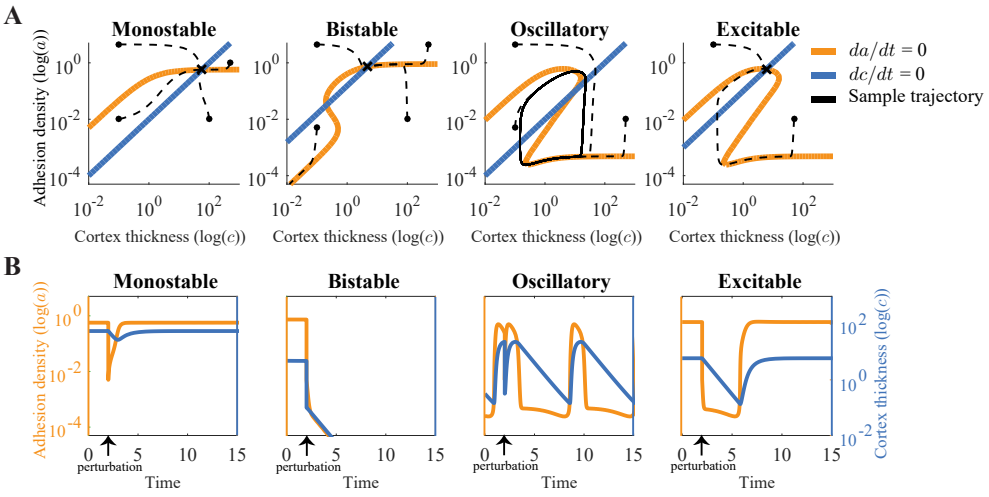

Figure 3.1: Phase plane analysis. (A) Range of behaviors of the system of equations given different parameter sets visualized by the nullclines (dark blue for c and light orange for a) of the non-dimensionalized system of equations. Sample trajectories are shown in black. (B) Time series plots of the adhesion density (orange) and cortex thickness (blue) beginning in steady state with a perturbation at time t=2. Monostable parameters: $\Omega = 100$,$\epsilon = 0.1$, $F = 6.3$, $M = 0.09$, $P = 0.08$ and $D = 0.23$, Bistable parameters: $\Omega = 6.5$, $\epsilon = 0.1$, $F = 2.9$, $M = 0.43$, $P = 0.016$ and $D = 0.19$, Oscillatory parameters: $\Omega = 100$, $\epsilon = 0.1$, $F = 1$, $M = 0.007$, $P = 0.1$ and $D = 0.15$, Excitable parameters: $\Omega = 10$, $\epsilon = 0.1$, $F = 1$, $M = 0.007$, $P = 0.1$ and $D = 0.15$.

3.3.2 Bifurcation analysis in ϵ and Ω

We next relax the assumption that $\epsilon \ll 1$ and characterize the dynamics of the system for various ϵ and Ω values. For $\epsilon \ll 1$, we noticed a bifurcation from a stable equilibrium

to a large amplitude stable limit cycle and back again (Figure 3.2A). As ϵ gets larger, the amplitude of the oscillations get smaller until they disappear entirely. The sudden

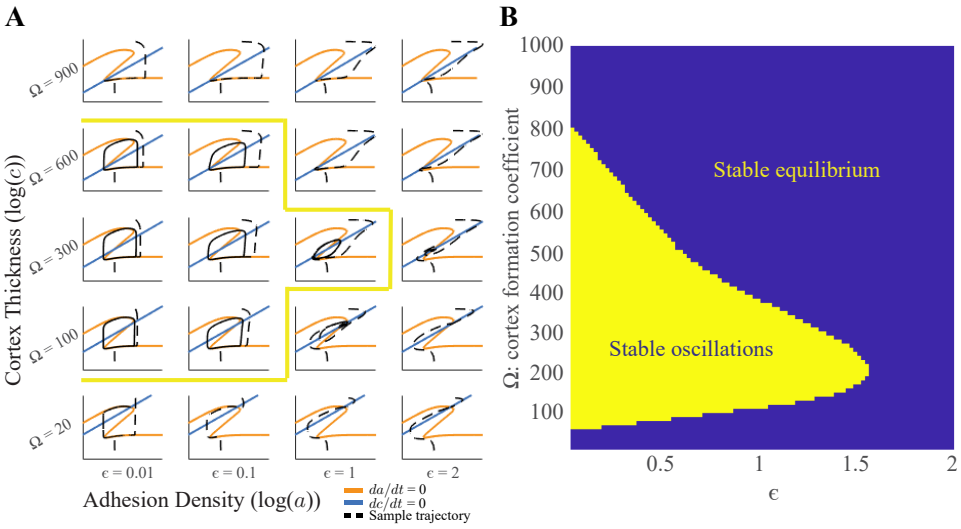

Figure 3.2: A bifurcation in the ODE system. (A) Phase plane diagrams with sample trajectories plotted for a range of Ω and ϵ values. The yellow line demarcates the boundary between the oscillatory and stable equilibrium regimes. (B) Two parameter sweep through Ω and ϵ demonstrating the emergence of stable oscillations in the system.

appearance of large-amplitude oscillations from a stable equilibrium is common in fast-slow dynamical systems [79]. Often these are Hopf bifurcations which happen in conjunction with a canard explosion [23], a "false bifurcation" in which amplitude grows rapidly with small changes in bifurcation parameter. In order to investigate this bifurcation, we employ continuation methods. In our case, a subcritical Hopf bifurcation occurs as the parameter Ω varies, as shown in Figure 3.3A. Here the amplitude of the unstable limit cycle was obtained using the continuation package XPP-AUTO. The canard occurs just prior to the collision of the unstable and stable limits cycles (Figure 3.3A). The canard is characterized by the resulting "duck-shaped" trajectories, as shown in Figure 3.3B top.

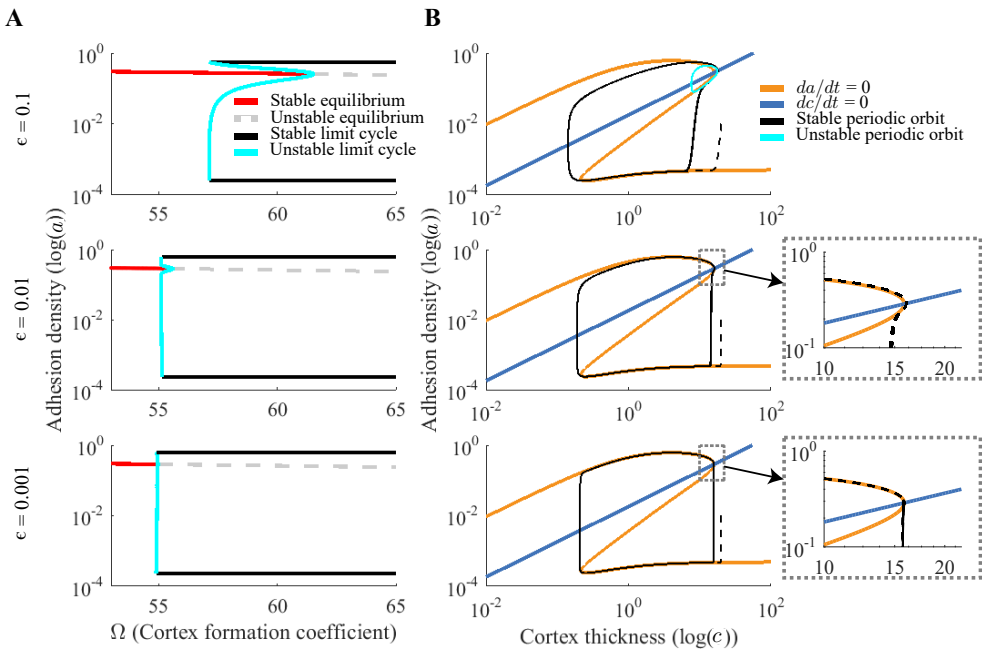

Figure 3.3: Canard explosion. (A) For small ϵ values, the system undergoes a subcritical Hopf bifurcation upon changes the the parameter Ω. (B) The characteristic canard trajectories. Stable trajectories are shown in black and the unstable trajectory is shown in cyan. The Ω values used in this plot are as follows: for $\epsilon = 0.1, \Omega = 57.15$, for $\epsilon = 0.01, \Omega = 55.15$, and for $\epsilon = 0.001, \Omega = 54.95$.

3.4 Full system in traveling wave parameter regime

As previously mentioned, for a particular set of parameters, the full non-dimensional system exhibits a traveling wave pulse. Here we define a traveling wave pulse as a solution which travels in space, x, with constant velocity and waveform, and which begins and ends in the same state (as opposed to a wavefront which is a transition from one state to a second state which propagates through space). Due to the separation of timescales in our system, are able to section the wave into different regions of dynamics, see Figure 3.4. Region I is the equilibrium state, a stable steady state solution at which the system remains unless perturbed. Region II comprises the wavefront. Regions III, IV and V are the plateau region, the downstroke, and the recovery phase respectively.

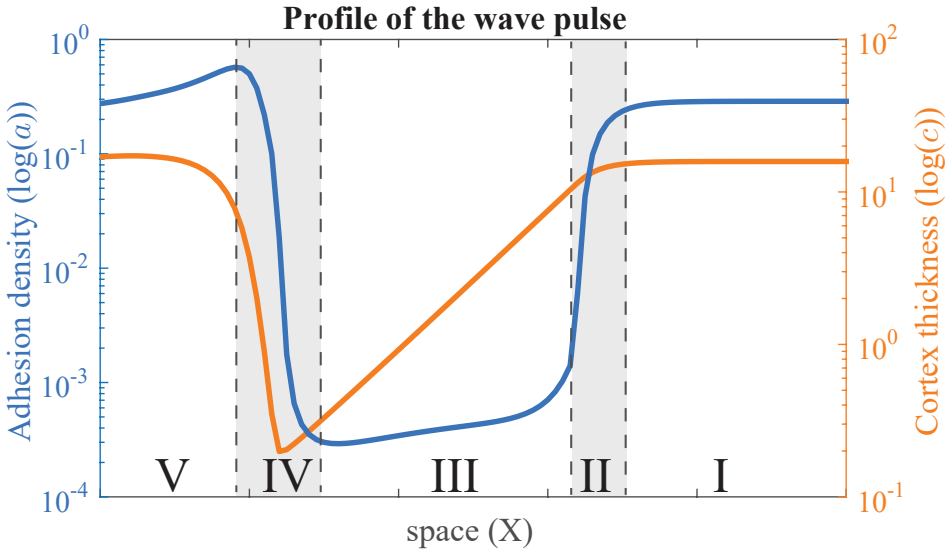

Figure 3.4: The traveling wave solution of the full non-dimensional system. The numerals denote different phases of the wave pulse: I. equilibrium state, II. wavefront, III. plateau, IV. downstroke and V. recovery phase.

3.4.1 Wavefront

In order to examine the wavefront, *i.e.* region II in Figure 3.4, we re-scale our equations by the change of variables $T = t/\epsilon$ and $X = x/\epsilon$. The system becomes

$$\frac{dc}{dT} = \epsilon(\Omega a - c) \tag{3.4.1}$$

$$\frac{da}{dT} = \frac{c}{1+c}\exp\left(-\frac{y-y_C}{D}\right) - a\exp\left(\frac{y-y_C}{F}\right) \tag{3.4.2}$$

$$0 = a(y-y_C) - Mcy_C \tag{3.4.3}$$

$$\frac{\partial^2 y}{\partial X^2} = -a(y-y_C) + P(1-y). \tag{3.4.4}$$

Note that since (3.4.3) is algebraic in y_C, we can eliminate it from the system. Collecting $\mathcal{O}(1)$ terms, we can eliminate (3.4.1) and as a result (3.4.2) becomes

$$\frac{\partial a}{\partial T} = \frac{c^{ss}}{1+c^{ss}}\exp\left(-\frac{y}{D}\left(1-\frac{a}{a+Mc}\right)\right) - a\exp\left(\frac{y}{F}\left(1-\frac{a}{a+Mc}\right)\right). \tag{3.4.5}$$

The dynamics of excitation are thus only governed by the a equation (3.4.5) and a version (3.4.3) with y_C written as a function of a and y. We will refer to this system as the inner re-scaling of the full system.

The traveling wave solution of the inner re-scaling of the full system is observed in Figure 3.5. In this parameter regime, (3.4.5) is bistable and the wave is characterized by a transition from the equilibrium state (a^+, y^+) to the other equilibrium state (a^+, y^+). Without loss of generality, we assume the waves traveling in this direction will be associated with a positive velocity v.

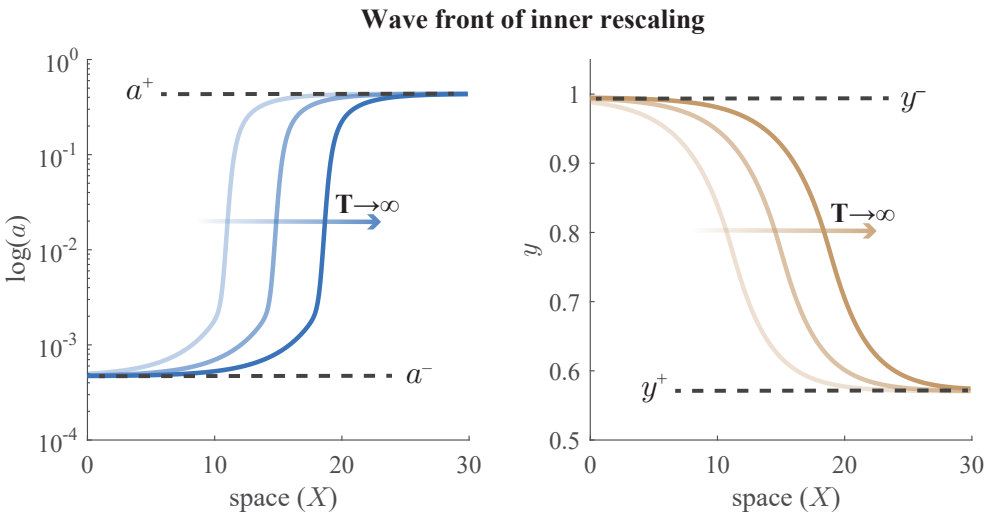

Figure 3.5: Wavefront of inner re-scaling of full non-dimensional system. The solution moves from the steady state (a^+, y^+) to (a^-, y^-).

By using the wave coordinate $Z = X - vT$, where v is the velocity of the traveling front, and substituting $a(X,T) = a(Z)$ and $y(X,T) = y(Z)$, the system is described by a first-order ODE and a second-order ODE (3.4.6)-(3.4.7), or equivalently 3 first-order ODEs:

$$-v\frac{da}{dZ} = \frac{c^{ss}}{1+c^{ss}}\exp\left(-\frac{y}{D}\left(1-\frac{a}{a+Mc}\right)\right) - a\exp\left(\frac{y}{F}\left(1-\frac{a}{a+Mc}\right)\right) \tag{3.4.6}$$

$$\frac{\partial^2 y}{\partial Z^2} = -ay\left(1-\frac{a}{a+Mc}\right) + P(1-y). \tag{3.4.7}$$

The traveling wave solution comprises an orbit that departs an initial fixed point (a^+, y^+) and arrives at another fixed point, (a^-, y^-) as $Z \to -\infty$ (as in Figure 3.6A,B). Using linear stability analysis, we calculated the stability properties at both fixed points via their eigenvalues (see Figure 3.7) and have found both fixed points to be saddles with one negative eigenvalue and 2 positive eigenvalues. If we let n_{init} = no. of eigenvalues with positive real part of the initial state and n_{fin} = no. of eigenvalues with negative real part of the final state, then we find in each case that $n_{init} + n_{fin} = 3 =$ dimension of the space. This suggests

there is a unique velocity which will provide a heteroclinic connector between the two states, for further discussion, see Chapter 6 of [57].

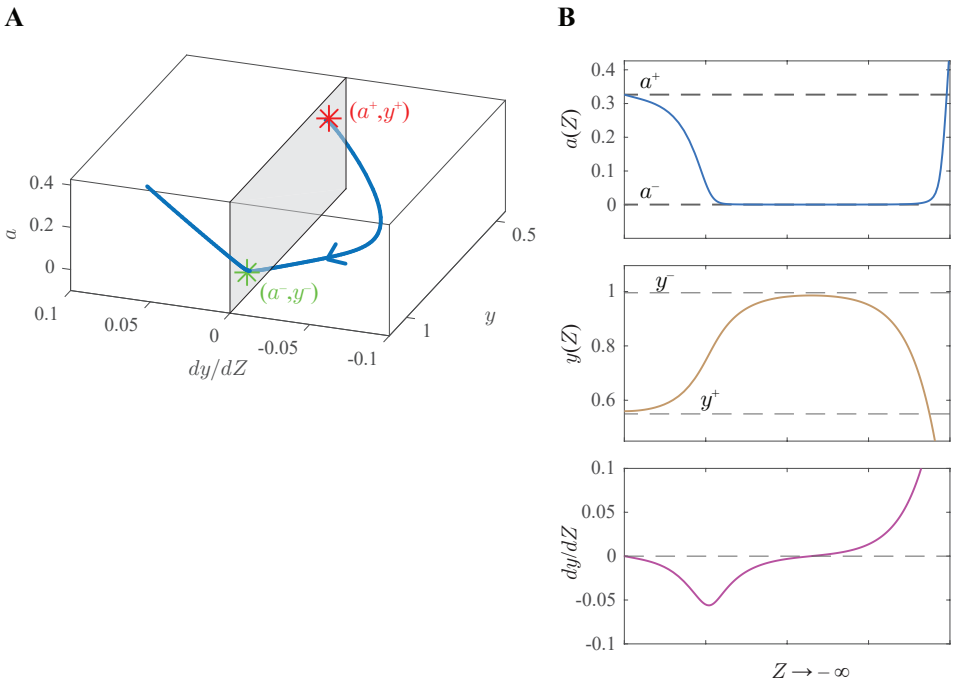

Figure 3.6: Trajectory of the system of 3 ODEs. (A)Trajectory of the system from $(a^+, y^+, dy/dZ = 0)$ to $(a^-, y^-, dy/dZ = 0)$ as $z \to -\infty$. (B) Individual variables as functions of Z. The parameter values used were $c^{ss} = 15.62, D = 0.15, P = 0.1, M = 0.007$, $F = 1$ and $v = 0.988$.

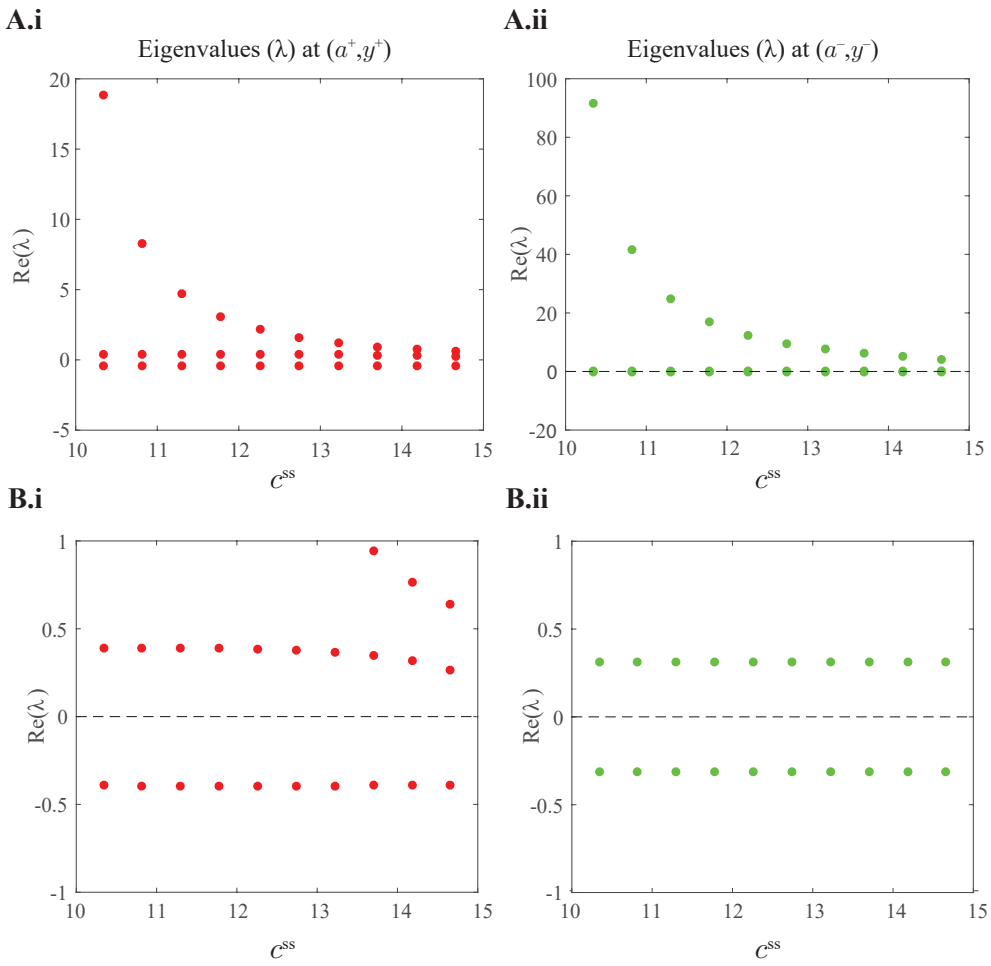

Figure 3.7: Eigenvalues of the system of 3 ODEs at $(a^+, y^+, 0)$ and $(a^-, y^-, 0)$. (A) Eigenvalues at i) $(a^+, y^+, 0)$ and ii) $(a^-, y^-, 0)$ as a function of c^{ss}. (B) Zoom in on the eigenvalues with at i) $(a^+, y^+, 0)$ and ii) $(a^-, y^-, 0)$ as a function of c^{ss}. The parameter values used were $D = 0.15, P = 0.1, M = 0.007$, and $F = 1$.

3.4.2 Downstroke

The upstroke of the wave occurs at $c = c^{ss}$, with velocity v. We conjectured that the downstroke occurs at a c value, $c = c^-$, that produces a velocity $-v$. We now move to region IV of Figure 3.4, re-scaled as in the previous section. Numerical exploration of c values has provided evidence that there does not exist such a c^- value. This might imply that the downstroke is a phase wave rather than a trigger wave. In this case, the downstroke will occur

at $c = c^{-}$ dictated by the shape of the nullcline of the corresponding non-spatial system, *i.e.* c will decrease until it "falls off" the $da/d\tau$ nullcline, as in fact it does for sufficiently small ϵ (see Figure 3.8A). Figure 3.8B shows the calculated velocities for a range of c^{ss} values spanning the region of bistability in the single ODE of the reduced system (where c is held constant). We see that a non-zero velocity only results from $c^{ss} \in [\approx 10, \approx 16]$, and is always positive. An sample wave is shown in Figure 3.8C for $c^{ss} = 13$. Interestingly, for $c^{ss} \in [\approx 0.5, \approx 10]$, we find wave stalling behavior (Figure 3.8D,E), where the perturbation neither spreads in a traveling wave nor recovers.

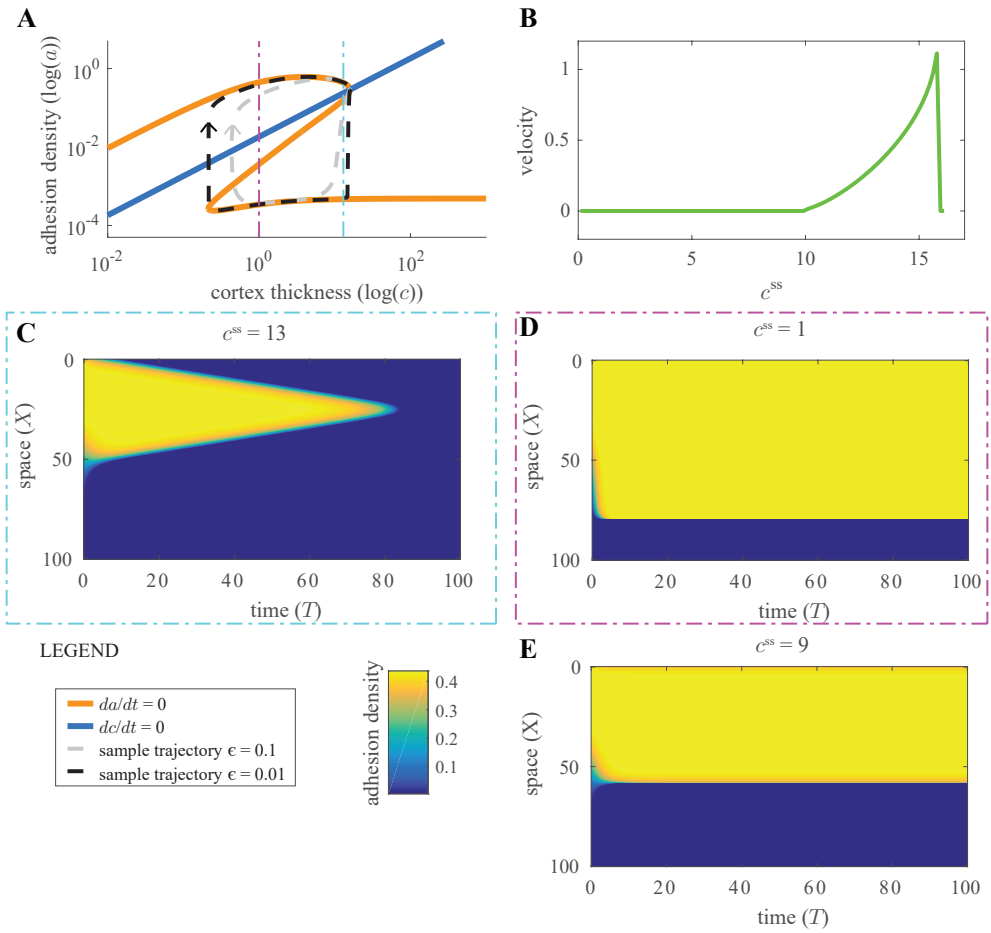

Figure 3.8: Investigation of the downstroke of the system. (A) Full system traveling wave trajectories plotted on the nullclines of the system for $\epsilon = 0.1$ and $\epsilon = 0.01$ at a spatial location sufficiently far from the initial perturbation (see red line in (C)). (B) Velocity as a function of c^{ss} in the reduced system (*i.e.* where $c = c^{ss}$ but y_C remains dynamic). (C) Adhesion density as a function of time and space with initial conditions smoothly transitioning from (a^+, y^+) to (a^-, y^-) across the spatial domain for $c^{ss} = 13$. Here we see a traveling wave solution. (D,E) Adhesion density as a function of time and space with initial conditions smoothly transitioning from (a^+, y^+) to (a^-, y^-) across the spatial domain for $c^{ss} = 1$ (D), and $c^{ss} = 9$ (E). Here we see that the solution doesn't travel in either direction. Other parameter values used were $D = 0.15, P = 0.1, M = 0.007$, $F_0 = 1$ and $\Omega = 55$.

To verify that this stalling behavior was not due to a numerical error, we used a fourth-order accurate central finite difference method in space looked at how the adhesion density converged to a steady state in space and time (Figure 3.9A,B). Additionally, we tested for convergence upon finer spatial discretization (Figure 3.9C) and finally that $|da/dT| \Rightarrow 0$

within the simulation time.

3.5 Derivation of a nonlocal Maxwell condition for traveling waves

Given a parameter regime in which the non-spatial system is excitable, will there be a traveling solution in the full system? This is the question we seek to answer. However this is outside our current scope. A narrower version of the system is obtained if we assume the force balance equations are linear in a, which can be done by making the following simplifying assumption: we assume the variable, y_C, does not move significantly during excitation, $y_C = y_C^{ss}$. This leaves us with a simplified system of two equations (while remaining in our inner re-scaling coordinates),

$$\frac{\partial a}{\partial T} = \frac{c^{ss}}{1+c^{ss}}\exp\left(-\frac{y-y_C^{ss}}{D}\right) - a\exp\left(\frac{y-y_C^{ss}}{F}\right) \tag{3.5.1}$$

$$0 = -a(y-y_C^{ss}) + P(1-y) + \frac{\partial^2 y}{\partial X^2}. \tag{3.5.2}$$

Let

$$f_1(y) = \frac{c^{ss}}{1+c^{ss}}\exp\left(-\frac{y-y_C^{ss}}{D}\right), \tag{3.5.3}$$

$$f_2(y) = \exp\left(\frac{y-y_C^{ss}}{F}\right), \tag{3.5.4}$$

$$g_1(y) = P(1-y), \tag{3.5.5}$$

$$g_2(y) = (y-y_C^{ss}). \tag{3.5.6}$$

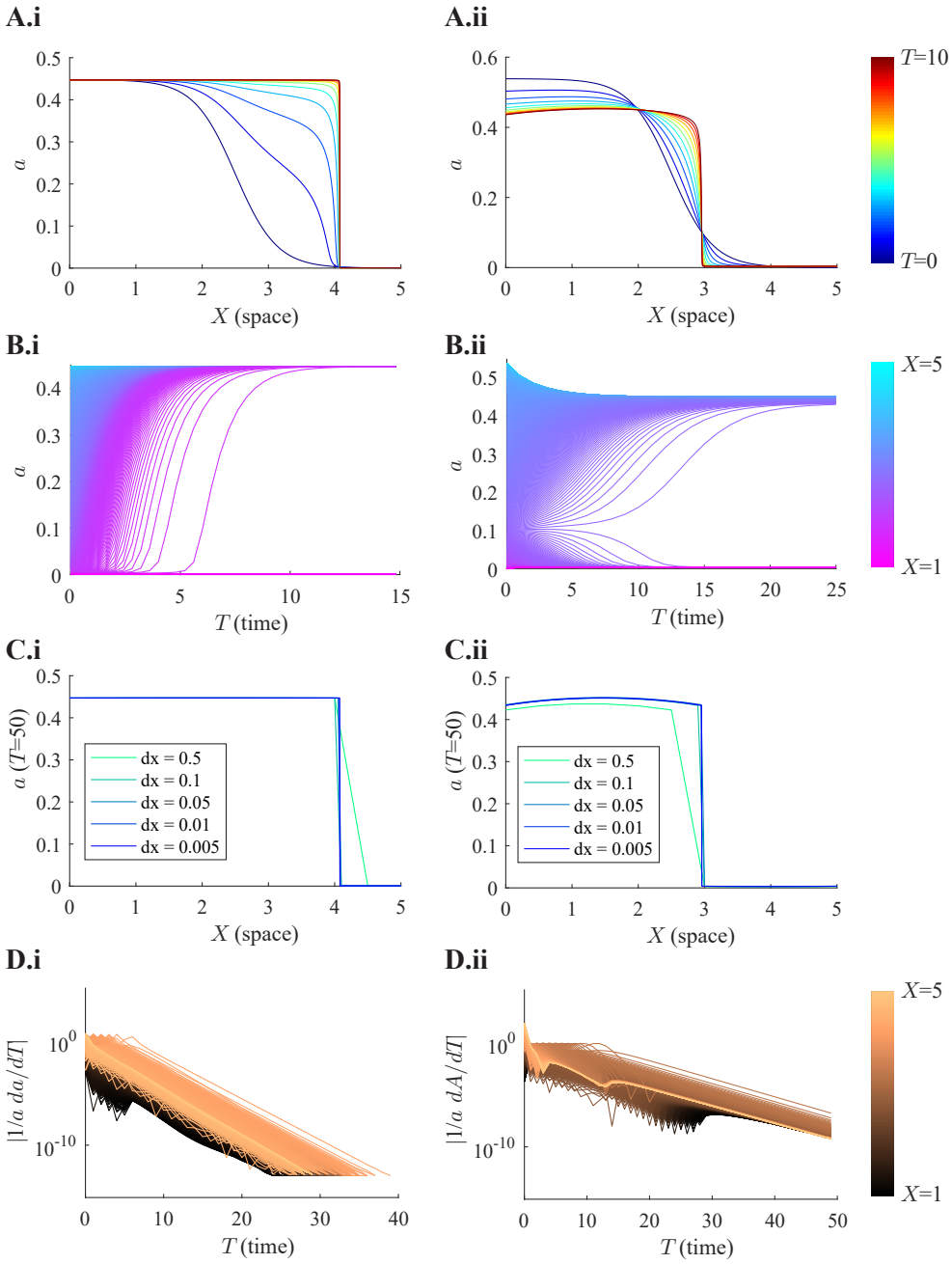

Figure 3.9: Analysis of the wave stalling behavior. (A) Adhesion density (a) across space (x-axis) over time (colormap) for i) $c^{ss} = 1$ and ii) $c^{ss} = 9$. (B) Adhesion density (a) across time (x-axis) over space (colormap) for i) $c^{ss} = 1$ and ii) $c^{ss} = 9$. (C) Adhesion density (a) at time $T = 50$ for various spatial discretizations for i) $c^{ss} = 1$ and ii) $c^{ss} = 9$. (D) Convergence to steady state in time over space (colormap) for i) $c^{ss} = 1$ and ii) $c^{ss} = 9$. Other parameter values used were $D = 0.15, P = 0.1, M = 0.007, F = 1$.

Our system can be generalized to the form:

$$\frac{da}{dT} = f_1(y) - af_2(y) \tag{3.5.7}$$

$$0 = g_1(y) - ag_2(y) + \frac{\partial^2 y}{\partial X^2}. \tag{3.5.8}$$

In this section, we derive a necessary condition for the system described by (3.5.7) and (3.5.8) to exhibit a traveling wave solution. In the parameter regime where we observe a traveling wave solution, shown in Figure 3.10, (3.5.1) is bistable. As such, we assume that the general system (3.5.7-3.5.8) has two stable roots which we will denote by (y^+, a^+) and (y^-, a^-). Without loss of generality, we assume the waves traveling from (y^+, a^+) to (y^-, a^-) will be associated with a positive velocity v.

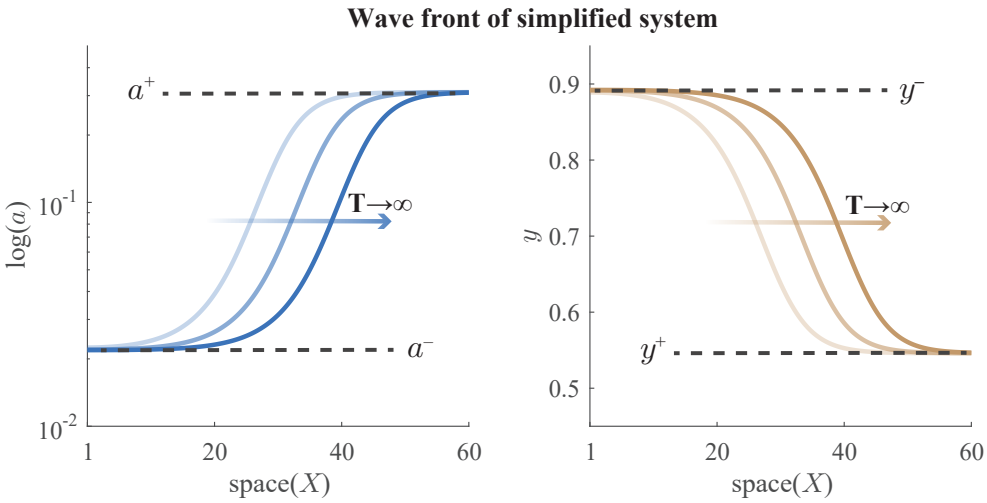

Figure 3.10: Wavefront of inner re-scaling of simplified system. The solution moves from the steady state (a^+, y^+) to (a^-, y^-). Parameters used are $c^{ss} = 20, y_c = 0.4, P = 0.1, D = 0.15$ and $F = 1$.

In order to study the traveling wave solution we again make a change of variables to a wave

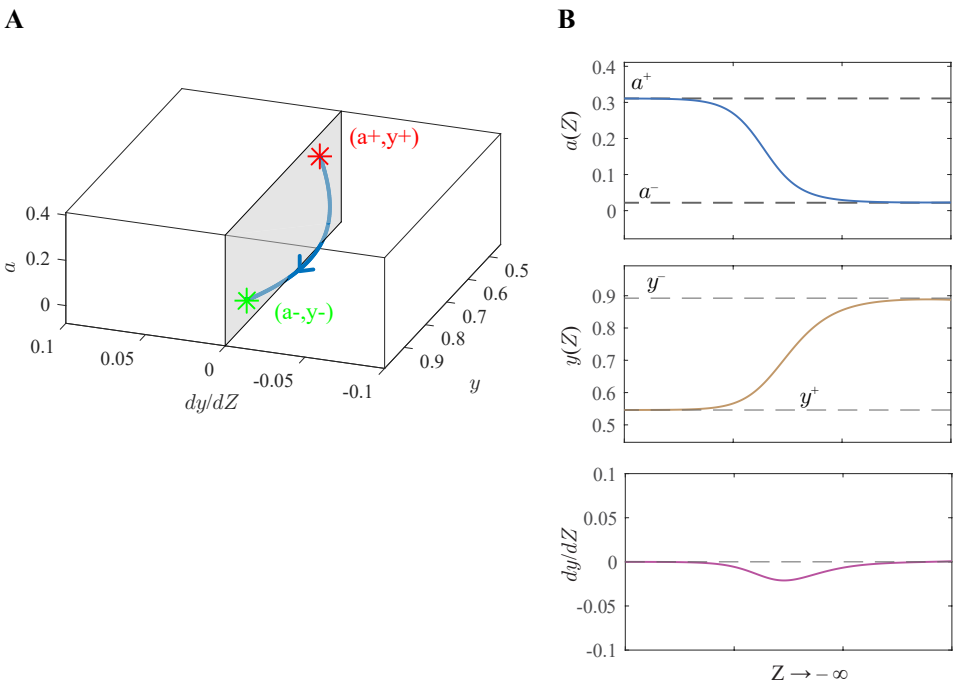

Figure 3.11: Trajectory of the simplified system of 3 ODEs. (A)Trajectory of the system from $(a^+, y^+, dy/dZ = 0)$ to $(a^-, y^-, dy/dZ = 0)$ as $Z \to -\infty$. (B) Individual variables as functions of Z. The parameter values used were $c^{ss} = 20, D = 0.15, P = 0.1, y_C = 0.4$, $F = 1$ and $v = 0.363$.

coordinate $Z = X - vT$. Equations 3.5.7-3.5.8 become

$$-v\frac{da}{dZ} = f_1(y) - af_2(y) \tag{3.5.9}$$

$$0 = g_1(y) - ag_2(y) + \frac{\partial^2 y}{\partial Z^2}. \tag{3.5.10}$$

Once again this results in a system described by a first-order ODE and a second-order ODE (3.5.9-3.5.10), or 3 first-order ODEs. The traveling wave solution departs an initial fixed point (a^+, y^+) and arrives at another fixed point, (a^-, y^-) as $Z \to -\infty$ for positive velocities (as in Figure 3.11A,B). We are now able to observe negative velocities (waves traveling from (a^-, y^-) to (a^+, y^+) as $Z \to -\infty$) for c^{ss} values above a certain threshold, c^*, as in Figure 3.12A. We also notice a change in the stability properties of the two steady states as c^{ss} passes through c^*. Both steady states have 1 negative eigenvalue and 2 positive eigenvalues for $c^{ss} < c^*$ and 2 negative eigenvalues and 1 positive eigenvalue for $c^{ss} > c^*$ (Figure 3.12B,C). In all cases, this is consistent with the suggestion of a single velocity.

3.5.1 The nonlocal Maxwell condition

Once we are in the traveling wave coordinate of the re-scaled simplified system (3.5.9-3.5.10), we can solve (3.5.10) for a,

$$a = \frac{1}{g_2(y)}\left(g_1(y) + \frac{\partial^2 y}{\partial Z^2}\right). \tag{3.5.11}$$

Note that this forces us to require that $g_2(y) \neq 0$ for $y \in [y^+, y^-]$. Then it follows that

$$-v\frac{\partial a}{\partial Z} = f_1(y) - \frac{g_1(y)}{g_2(y)}f_2(y) - \frac{f_2(y)}{g_2(y)}\frac{\partial^2 y}{\partial Z^2}. \tag{3.5.12}$$

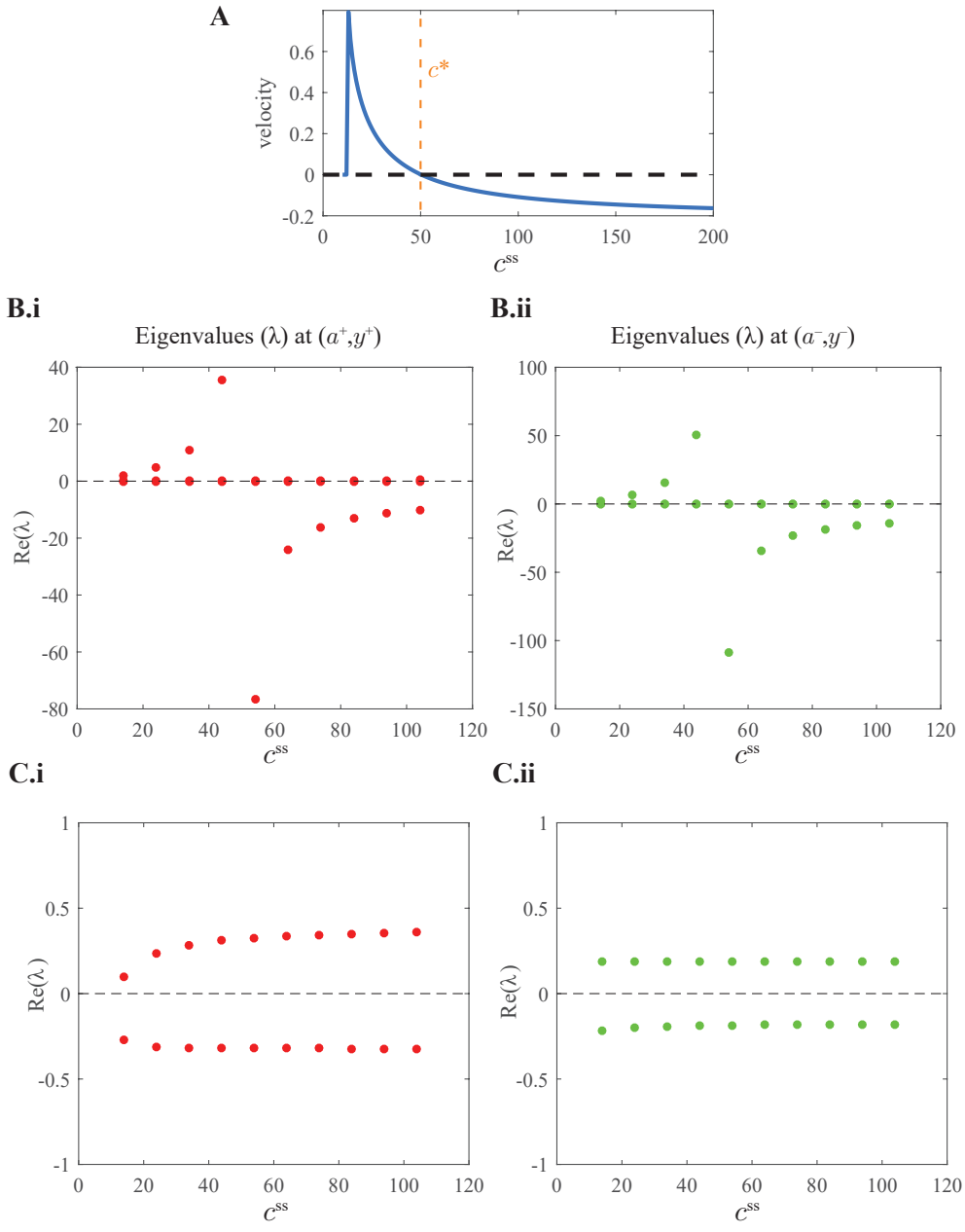

Figure 3.12: Velocities and eigenvalues of the simplified system of 3 ODEs at $(a^+, y^+, 0)$ and $(a^-, y^-, 0)$. (A) Velocity of the simplified system as a function of c^{ss}. (B) Eigenvalues at i) $(a^+, y^+, 0)$ and ii) $(a^-, y^-, 0)$ as a function of c^{ss}. (C) Zoom in on the eigenvalues with at i) $(a^+, y^+, 0)$ and ii) $(a^-, y^-, 0)$ as a function of c^{ss}. The parameter values used were $D = 0.15, P = 0.1, y_C = 0.4$, and $F = 1$.

We then multiply by $\frac{g_2(y)}{f_2(y)}\frac{\partial y}{\partial Z}$ (again, now requiring that $f_2(y) \neq 0$ for $y \in [y^+, y^-]$) and integrate over Z,

$$\int_{-\infty}^{\infty} -v\frac{\partial a}{\partial Z}\frac{g_2(y)}{f_2(y)}\frac{\partial y}{\partial Z}dZ = \int_{-\infty}^{\infty}\left(f_1(y)\frac{g_2(y)}{f_2(y)} - g_1(y) - \frac{\partial^2 y}{\partial Z^2}\right)\frac{\partial y}{\partial Z}dZ. \tag{3.5.13}$$

We change variables on RHS,

$$\begin{aligned}
-v\int_{-\infty}^{\infty}\frac{\partial a}{\partial Z}\frac{g_2(y)}{f_2(y)}\frac{\partial y}{\partial Z}dZ &= \int_{y^-}^{y^+}\left(f_1(y)\frac{g_2(y)}{f_2(y)} - g_1(y) - \frac{\partial^2 y}{\partial Z^2}\right)dy \\
\Rightarrow -v\int_{-\infty}^{\infty}\frac{\partial a}{\partial Z}\frac{g_2(y)}{f_2(y)}\frac{\partial y}{\partial Z}dZ &= \int_{y^-}^{y^+}\left(f_1(y)\frac{g_2(y)}{f_2(y)} - g_1(y)\right)dy - \cancelto{0}{\int_{y^-}^{y^+}\frac{\partial^2 y}{\partial Z^2}dy} \\
\Rightarrow -v\int_{-\infty}^{\infty}\frac{\partial a}{\partial Z}\frac{g_2(y)}{f_2(y)}\frac{\partial y}{\partial Z}dZ &= \int_{y^-}^{y^+}\left(f_1(y)\frac{g_2(y)}{f_2(y)} - g_1(y)\right)dy.
\end{aligned} \tag{3.5.14}$$

For the specific case of our cellular blebbing model, we plug in (3.5.3-3.5.6) and obtain

$$\begin{aligned}
-v\int_{-\infty}^{\infty}\frac{\partial a}{\partial Z}\frac{\partial y}{\partial Z}\exp\left(-\frac{y-y_C^{ss}}{F}\right)(y-y_C^{ss})dZ& \\
= \int_{y^-}^{y^+}\left(\frac{c^{ss}}{1+c^{ss}}\exp\left(-\left(\frac{1}{D}+\frac{1}{F}\right)(y-y_C^{ss})\right) - P(1-y)\right)dy.&
\end{aligned}$$

We also note that in our specific case $y^- > y^+$ (see Figure 3.10) and therefore it is more natural to integrate from y^+ to y^-.

$$\begin{aligned}
-v\int_{-\infty}^{\infty}\frac{\partial a}{\partial Z}\frac{\partial y}{\partial Z}\exp\left(-\frac{y-y_C^{ss}}{F}\right)(y-y_C^{ss})dZ& \\
= -\int_{y^+}^{y^-}\left(\frac{c^{ss}}{1+c^{ss}}\exp\left(-\left(\frac{1}{D}+\frac{1}{F}\right)(y-y_C^{ss})\right) - P(1-y)\right)dy.&
\end{aligned} \tag{3.5.15}$$

We define the nonlocal Maxwell condition number as

$$NLMC = -\int_{y^+}^{y^-} \left(\frac{c^{ss}}{1+c^{ss}} \exp\left(-\left(\frac{1}{D} + \frac{1}{F} \right) (y - y_C^{ss}) \right) - P(1-y) \right) dy$$
$$\exp\left(+\left(\frac{1}{D} + \frac{1}{F} \right) y_C^{ss} \right) \left(y^- - y^+ \right) + P\left(1 - \frac{1}{2}\left(\left(y^+\right)^2 - \left(y^-\right)^2 \right) \right).$$

The integral on the LHS is of (3.5.15) determined sign (-). Therefore, the nonlocal Maxwell condition in this case is

$$NLMC \leq 0 \Rightarrow v = 0, \text{no traveling solution.}$$

Note that only necessity is shown here.

We varied two parameters continuously in our simplified re-scaled system (3.5.1-3.5.2) to numerically verify our derivation of this necessary condition for traveling waves. To solve these equations we built a PDE solver in which we use a standard five-point stencil finite difference method in space and forward-Euler in time. We discretized space into a uniform grid of width $\Delta x = 0.1$ and time step size $\Delta T = 0.01$, and used MATLAB's `mldivide` to solve (3.5.2) directly.

The nonlocal Maxwell condition is equal to 0 in the parameter regimes where (3.5.1) has only one stable root (because $y^- = y^+$), but can be negative or positive in the bistable regime. Figure 3.13A shows the sign value of the nonlocal Maxwell condition number through our two-parameter sweep. The regions shown in Figure 3.13A align with the numerical solutions of the PDE as depicted in Figure 3.13B, which shows the velocity of the traveling wave solution (= 0 for a stationary solution). This numerical evidence suggests that the nonlocal Maxwell condition is also a sufficient sufficient condition (i.e. $NLMC > 0 \Rightarrow$ v exists, traveling solution).

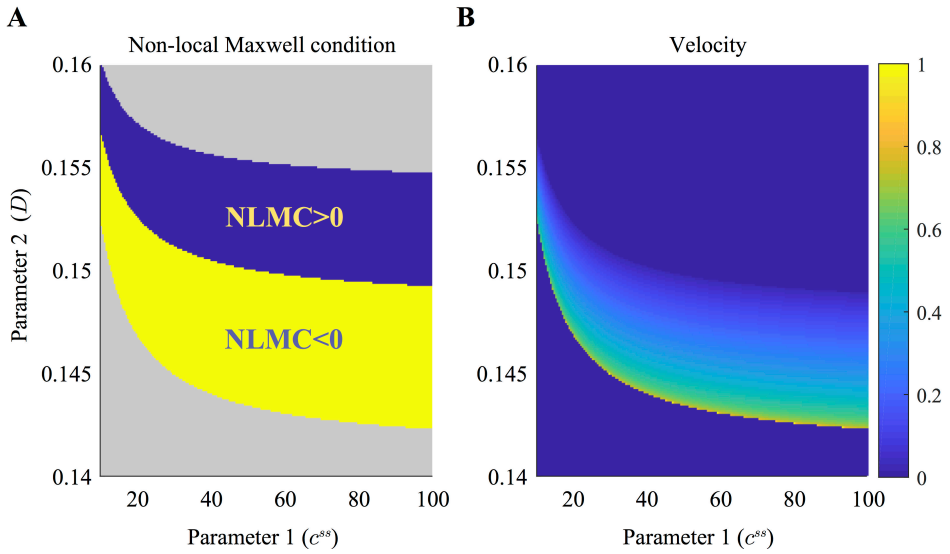

Figure 3.13: Nonlocal Maxwell condition demonstrating emergence of traveling waves. (A) Plot of the sign of the nonlocal Maxwell condition as parameters c^{ss} and D are varied in the system. Gray areas indicate regions where the system is not bistable, and therefore the condition is not applicable. (B) Plot of velocity of the system as parameters c^{ss} and D are varied in the system.

3.6 Concluding remarks

Here we have derived a condition, analogous to the Maxwell condition, for predicting traveling wave solutions to a particular class of integro-PDE occurring in biology. The traveling wave observed here shares several properties with other classes of traveling waves encountered in the field.

Fisher waves are the archetypal traveling wavefront of modern mathematical biology. They arise as solutions to the Fisher-Kolmogorov equation [28, 54]. It is considered the simplest non-linear reaction diffusion equation. When transformed to the wave variable, $z = x - vt$, this equation becomes a second order ODE in z. Linear stability analysis on the two equilibrium solutions showed that there is one stable equilibrium and one saddle node. It also revealed that there exist a c_{min} value below which traveling wave solutions are not

physically relevant (stable equilibrium is a focus). When physiologically relevant traveling waves are observed, it has been show that the observed speed is strongly dependent on the initial conditions [71], putting these waves in a different class than those described here.

The FitzHugh-Nagumo model [29, 73] is a two species system of ODEs which was originally developed as a simplification of the Hodgkin-Huxley action potential model. When diffusion is added to the model, the system produces traveling waves in the form of pulses, as well as oscillations. It is a classic example of traveling waves in excitable media. As in the system described in this work, traveling wave solutions only occur when the corresponding non-spatial (i.e. without diffusion) system is in an excitable parameter regime, which arises from the separation of timescales inherent to the system, and the non-linear feedback within the equations. Within this regime, the existence of traveling wave can be predicted using the classical (local) Maxwell condition. The downstroke of this system has been investigated and it has been found that for different parameters the system can admit both trigger-type and phase-type downstrokes [99], unlike our system.

The Wilson-Cowan model [103, 102] is a neural field model describing the overall evolution of populations of excitatory and inhibitory neurons. While the first description of the model [103] was spatially homogeneous, the spatially structured model [102] rendered the model a system of two integro-PDEs. Varying the strength of connections between these populations, as well as other parameters the model can exhibit a variety of dynamics including traveling wave pulses, damped waves and oscillations. Phase plane analysis on the spatially homogeneous system [103], Wilson and Cowan found that for sufficient strong synapses between excitatory cells, the system exhibits bistability. On the other hand, weak synapses between inhibitory cells gave rise to limit cycle solutions. While the model account for different timescales of activity between excitatory and inhibitory populations, traveling wave solutions do not require the separation of timescales characteristic of traveling waves in excitable media.

A phenomenon known as wave-pinning has been shown to arise in a model of cell polarization [67]. The model consists of a pair of reaction-diffusion equations representing active/inactive forms of a protein with positive feedback to its own activation. When the inactive form of the protein is held constant, and the equation describing dynamics of the active form is bistable, the system exhibits traveling wavefronts [67]. However, when the two equations are coupled the traveling front decelerates and becomes stationary. While there is no separation of timescale in this system, it is crucially dependent on a separation of scales in the diffusion coefficients between the two forms.

3.6.1 Future goals

In greatest generality, we would be ultimately interested in a necessary and sufficient traveling wave condition for the system

$$\frac{\partial a}{\partial t} = f(a, y) \tag{3.6.1}$$

$$0 = g\left(a, y, \frac{\partial^2 y}{\partial x^2}\right). \tag{3.6.2}$$

This would likely encompass a larger class of models describing biological or biochemical systems, and would therefore be more useful to the mathematical biology community as a whole.

Chapter 4

Nuclear shape*

4.1 Introduction

Cardiomyopathies and arrhythmia are conditions with high morbidity and limited therapies. Although a vast number of genes have been discovered to contribute to the etiology of these diseases, translational research, the practical application of genetic knowledge to improve screening, diagnosis, and treatment for affected individuals and their families has been limited. One major obstacle is the lack of understanding of the relationship between genotype and emergent phenotype, the mechanisms by which pathologies occur, and the identification of factors that cause clinical variability between and within families. Our collaborators in the Grosberg (UCI - Department of Biomedical Engineering) and Zargoza (UCI - School of Medicine) labs are currently studying three affected families each with different mutation in the Lamin A/C (LMNA) gene. LMNA, together with LMNB1 and LMNB2, encode the main proteins of the nuclear lamina, the structural matrix of the nuclear envelope that interacts with both chromatin in the cell nucleus and the cytoskeleton [11]. In their experiments, it

*with M. Mehrabi, A. Grosberg, M. Zaragoza and J. Allard

has been obserbed that the nuclei often have a wide variety of geometrical defects, including rounded protrusions which we will refer to as nuclear blebs, as in Figure 4.1. This is a known property of LMNA mutated cell lines [70] (such as in progeria), however the mechanisms by which such defects forms are unclear. It is known that the LMNA mutation impacts the nuclear lamina, which is present at the inner layer of the nuclear membrane. As a key component of the nuclear lamina, lamin plays an important role in nucleus-cytoplasm interaction and signaling through lamin-binding protein complexes including SUN and KASH that span the nuclear membrane [43]. Cells in this line of experiments come from patients with heart disease (*i.e.*, cardiomyopathy and/or arrhythmia), and they exhibit a mutation in a gene that is known to correlate with nuclear defects. In addition, our collaborators have control cells from people without heart diseases from the same family as the patients' cells. Nuclei from both patient and control cell lines have been imaged, and a variety of nuclear shapes in the two types of cells has been found. Nuclear blebbing involves dynamic, complex interactions among many elements: The nuclear lamina, nuclear membranes , membrane-lamin linkers, and chromatin. Preliminary studies have found that both control (fibroblasts of human origin with no mutation) and patient (fibroblasts from patients with the mutation) exhibit some number of defects. We hypothesize a correlation between nuclear shape types and cardiomyopathy and arrhythmia. Therefore we have an ideal system in which to investigate a possible correlation between specific nuclear defects and disease states.

We use mathematical modeling that has potential to test the hypothesis that abnormal nuclear shapes in patients arise due to a mechanical anomaly in the lamin protein due to the mutation in LMNA. This will allow the possibility to differentiate between the type of defects expected under normal biological variability *vs.* in a pathological situation.

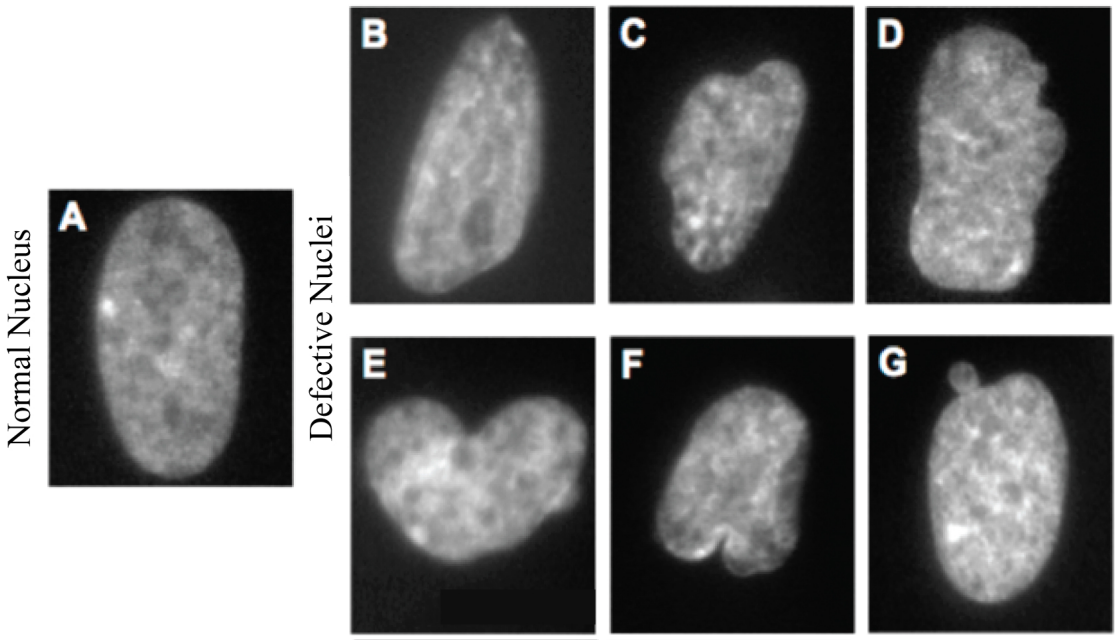

Figure 4.1: Defective nuclei have an irregular shape as compared to normal nuclei. In particular, there may exist one or more protrusions at the boundary resulting in a concave nuclei. Image used with permission [21].

4.2 Model

4.2.1 Statement of the model

We developed a model which consists of 2 dynamic variables representing the line density of lamin A/C, $a(t)$, and lamin B, $b(t)$, as functions of time, t on a simple closed curve in 2D, $s(t)$, enclosing an area, $\mathcal{A}(t)$. The details of lamin A/C (B) assembly and disassembly into the lamina are unknown, we assume usual assembly kinetics and allow for possible feedback in the disassembly terms. It is known that lamin proteins are not confined to the nuclear lamina, but exist in the nucleoplasm where they may be performing other functions, including gene regulation [46, 48]. We will assume there is a pool of nuclear lamins which exchanges dynamically with the the lamins in the nuclear lamina. The resulting equations are:

$$\frac{\partial a}{\partial t} = \frac{k^a_{\text{on}}}{\mathcal{A}(t)} a_{\text{nuc}} - k^a_{\text{off}}(s,b)a \tag{4.2.1}$$

$$\frac{\partial b}{\partial t} = \frac{k^b_{\text{on}}}{\mathcal{A}(t)} b_{\text{nuc}} - k^b_{\text{off}}(s,a)b. \tag{4.2.2}$$

The parameters $k^a_{\text{on}}, k^b_{\text{on}}$ govern assembly of lamin A/C, and lamin B into the lamina, respectfully. The functions $k^a_{\text{off}}(s,b) = k^{0a}_{\text{off}} + \Phi_a(s,b)$ and $k^b_{\text{off}}(s,a) = k^{0b}_{\text{off}} + \Phi_b(s,a)$ describe laminar turnover with possible feedback terms arising from Φ to be explored in future work and will be further discussed in Section 4.3. The nuclear pools of lamin A/C (B) are labeled by $a_{\text{nuc}}(b_{\text{nuc}})$. We therefore have the following conservation of lamin equations:

$$a_{\text{tot}} = \int_0^{\mathcal{L}_0} a(s,t)ds + a_{\text{nuc}} \tag{4.2.3}$$

$$b_{\text{tot}} = \int_0^{\mathcal{L}_0} b(s,t)ds + b_{\text{nuc}}. \tag{4.2.4}$$

Here, $\mathcal{L}_0$ is the length of the perimeter of a nucleus. These equations are coupled to a mechanical description of the lamina via the energy functional:

$$\mathcal{E} = \mathcal{E}_{\text{stretch}} + \mathcal{E}_{\text{pressure}} + \mathcal{E}_{\text{bending}} + \mathcal{E}_{\text{cytoskeleton}} + k_B\mathcal{T}\xi, \tag{4.2.5}$$

where

$$\mathcal{E}_{\text{stretch}} = \int_0^{\mathcal{L}_0} \frac{1}{2}(\mathcal{G}_a(a(s)) + \mathcal{G}_b(b(s))) \left(\left|\left| \frac{\partial \vec{x}}{\partial s} \right|\right| - 1 \right)^2 ds, \tag{4.2.6}$$

$$\mathcal{E}_{\text{pressure}} = \mathcal{P} \left(\frac{\mathcal{A}}{\mathcal{A}_0} - 1 \right)^2, \tag{4.2.7}$$

$$\mathcal{E}_{\text{bending}} = \int_0^{\mathcal{L}_0} \frac{1}{2}(\mathcal{M}_a(a(s)) + \mathcal{M}_b(b(s)) \left|\left| \frac{\partial^2 \vec{x}}{\partial s^2} \right|\right|^2 ds, \tag{4.2.8}$$

$$\mathcal{E}_{\text{cytoskeleton}} = \int_0^{\mathcal{L}_0} \mathcal{F}_{\text{cyto}}(a(s))\Theta(\theta)||\vec{x}||ds, \tag{4.2.9}$$

and

$$\Theta(\theta) = \frac{e^{\text{COS}\,(2\theta)/\sigma_{\text{VM}}}}{\int_0^{2\pi} e^{\text{COS}\,(2\theta)/\sigma_{\text{VM}}} d\theta}.$$

The lamina is modeled as an elastic material where the first term, $\mathcal{E}_{\text{stretch}}$ corresponds to laminar surface tension. The next term, $\mathcal{E}_{\text{pressure}}$ is the intranuclear pressure, possibly due to chromatin. The third term, $\mathcal{E}_{\text{bending}}$ is bending resistance terms due to lamin-lamin cross-linking. It is known that there are non-negligible forces produced by the cellular cytoskeleton (actin and microtubules) which act on the lamins via nuclear transmembrane proteins [40] and so the fourth term, $\mathcal{E}_{\text{cytoskeleton}}$, is due to this. Finally we include a term for thermal fluctuations generalized to 2D, $k_B\mathcal{T}\xi$. A cartoon schematic of the model is shown in Figure 5.2.

Several of the mechanical parameters are in fact functions of the local densities of laminar proteins, thus connecting the mechanical properties of the lamina (and therefore the nucleus) to the mechanical properties of lamin. A complete list of parameter descriptions can be found in Table 4.1.

We nondimensionalized the system by choosing characteristic scales for length, time, energy and amount of lamin. The details of this nondimensionalization procedure can be found in Appendix B. The resulting nondimensional system is expressed by the following system of

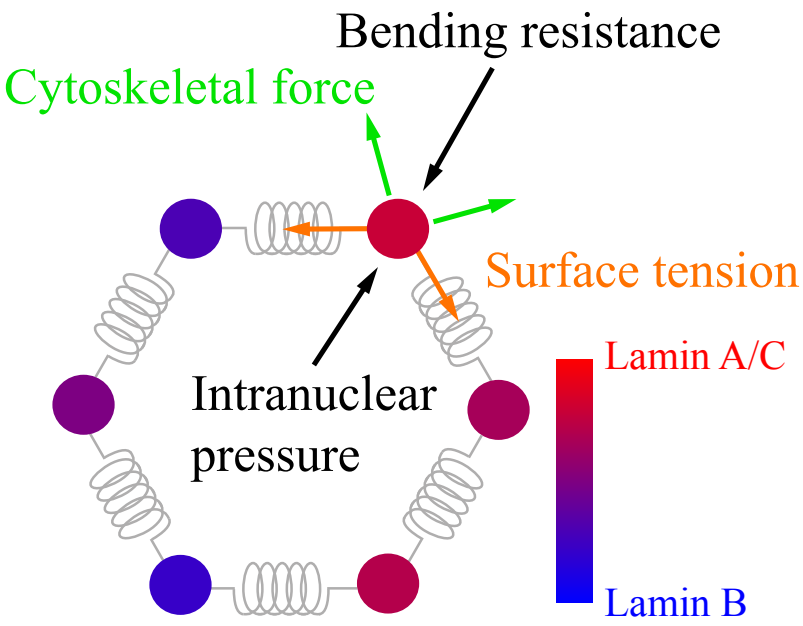

Figure 4.2: Schematic diagram of the model including Lamin A/C/B desities, and the forces acting on the lamina.

Table 4.1: Mechanical parameters.

Symbol	Dimensions	Meaning
$\mathcal{G}_a$	[pN]	Stretch modulus associated with lamin A/C
$\mathcal{G}_b$	[pN]	Stretch modulus associated with lamin B
$\mathcal{P}$	[pNμm]	Bulk modulus
$\mathcal{L}_0$	[μm]	Resting perimeter of nucleus
$\mathcal{M}_a$	[pNμm^2]	Bending modulus associated with lamin A/C
$\mathcal{M}_b$	[pNμm^2]	Bending modulus associated with lamin B
θ	[rad]	Angle
$\mathcal{F}_{\text{cyto}}$	[pN /μm]	Force line density of the cytoskeleton
σ_{VM}	[dimensionless]	Concentration of distribution of cytoskeletal force

equations:

Table 4.2: Nondimensionalized variables.

Symbol	Meaning
A	Laminar nondimensionalized density of Lamin A/C
B	Laminar nondimensionalized density of Lamin B
A_{nuc}	Nucleoplasmic lamin A/C
B_{nuc}	Nucleoplasmic lamin B
S	Nondimesionalized position of the lamina
$\lambda(\tau)$	Nondimesionalized area of nucleus

$$\frac{\partial A}{\partial \tau} = \kappa_{\text{on}} \frac{1}{\lambda(\tau)} A_{\text{nuc}} - (\kappa_{\text{off}} + \phi_A(S, B))A, \tag{4.2.10}$$

$$\frac{\partial B}{\partial \tau} = \frac{1}{\lambda(\tau)} B_{\text{nuc}} - (1 + \phi_B(S, A))B, \tag{4.2.11}$$

$$\tag{4.2.12}$$

with energy

$$E = \int_0^{2\sqrt{\pi}} \frac{1}{2}(G_A(A(S)) + G_B(B(S))) \left(\left| \left| \frac{\partial \vec{\chi}}{\partial S} \right| \right| - 1 \right)^2 dS + \Pi \left(\frac{\lambda(\tau)}{\lambda_0} - 1 \right)^2 \tag{4.2.13}$$

$$+ \int_0^{2\sqrt{\pi}} \frac{1}{2}(M_A(A(S)) + M_B(B(S))) \left| \left| \frac{\partial^2 \vec{\chi}}{\partial S^2} \right| \right|^2 dS \tag{4.2.14}$$

$$+ \int_0^{2\sqrt{\pi}} F_{\text{cyto}}(A(S))\Theta(\theta) \, ||\vec{\chi}|| \, dS + k_B T \xi. \tag{4.2.15}$$

A description of non dimensional variables can be found in Table 4.2 and parameters in Table 4.3.

Table 4.3: Nondimensionalized (ND) parameters.

Symbol	Meaning
κ_{on}	ND rate constant associated with lamin A/C incorporation into the lamina
κ_{off}	ND rate constant associated with lamin A/C dissociation from the lamina
G_A	ND stretch modulus associated with lamin A/C
G_B	ND stretch modulus associated with lamin B
Π	ND bulk modulus
λ_0	Resting non-dimensionalized area of nucleus
M_A	ND bending modulus associated with lamin A/C
M_B	ND bending modulus associated with lamin B
θ	Angle
F_{cyto}	ND force line density of the cytoskeleton

4.2.2 Numerical implementation of the model

The model is implemented in Matlab by discretizing the 2D simple closed curve into a series of nodes connected by linear springs with an elastic modulus dependent on the amount of lamins at the two nodes on either side of each spring. We solve the ODE systems using the forward Euler method. The energy minimization is done using a Markov chain Monte Carlo method known as the Metropolis algorithm. At each step forward in time, $10n$, where $n =$ no. of nodes, single node movements are proposed at random from a uniform distribution. For each node movement, the energy is re-calculated and an acceptance criterion is calculated based on the difference between the current energy state of the system, $\mathcal{E}_{\text{current}}$, and the energy state of the proposed move, $\mathcal{E}_{\text{proposed}}$. If the acceptance criterion $\left(\exp \frac{\mathcal{E}_{\text{current}} - \mathcal{E}_{\text{proposed}}}{k_B T \xi}\right)$ is greater than a randomly generated number on a uniform distribution between 0 and 1, the move is accepted, otherwise the move is rejected. In this way, we accept moves that are energetically favorable with higher probability.

4.2.3 Tuning the model

Many of the mechanical parameters of the model are unknown because they are difficult or impossible to measure experimentally. We therefore have to tune the parameters in

our model using some data. We used data from a series of experiments conducted on rat cardiomyocytes grown on fibronectin islands of various shapes and sizes as shown in Figure 4.3 [25]. The features we extracted from the images are cellular aspect ratio, F-actin OOP (a measure of the anisotropy in the F-actin network), nuclear eccentricity, nuclear area, and nuclear perimeter.

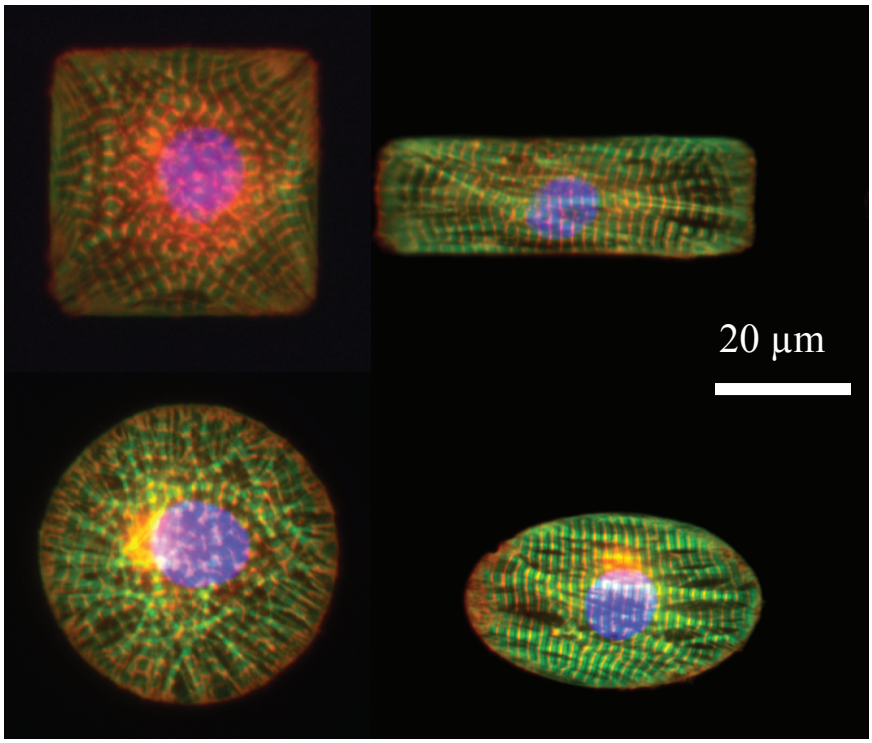

Figure 4.3: Rat cardiomyocytes grown on fibronectin islands of various shapes and sizes. Image used with permission [25].

In order to extract information about the correlations between these features we plotted each against the others in a scatter plot matrix, see Figure 4.4. While most of the data appear uncorrelated, there is a clear correlation between F-actin OOP and nuclear eccentricity (R^2 = 0.42), and other attributes suitable for fitting. In particular, we chose three patterns in the data to fit our model: nuclear area, nuclear perimeter and correlation between F-actin OOP and nuclear eccentricity. We first chose a subset of the cell which have an aspect ratio of 1 and tuned parameters to match the histograms of nuclear area and nuclear perimeter in both mean and standard deviation. This subset of cells was chosen so that we could

Table 4.4: Order of magnitude parameter estimations.

Parameter	Estimate
$\mathcal{G}_a, \mathcal{G}_b$	$10^0 - 10^1$ pN
$\mathcal{P}$	$10^0 - 10^1$ pN$\cdot\mu$m
$\mathcal{L}_0$	28 μm fds
$\mathcal{M}_a, \mathcal{M}_b$	$10^4 - 10^5$ pN$\cdot\mu$m^2]
$\mathcal{F}_{\text{cyto}}$	$10^3 - 10^4$ pN/μm

assume isotropic cytoskeletal force and therefore set it to 0. Once these parameters were tuned (Figure 4.5), we returned to the entire data set and tuned our model to match the eccentricity vs F-actin OOP plot, see Figure 4.6. This gave us an estimate of F_{cyto} which is in fact a ratio of two dimensional quantities, $\mathcal{F}_{\text{cyto}}$ and $\mathcal{G}_b$. Since the traction force of actin has been measured experimentally [56], we were able to back-calculate and to obtain order of magnitude estimates for all our mechanical parameters. These estimates are summarized in Table 4.4.

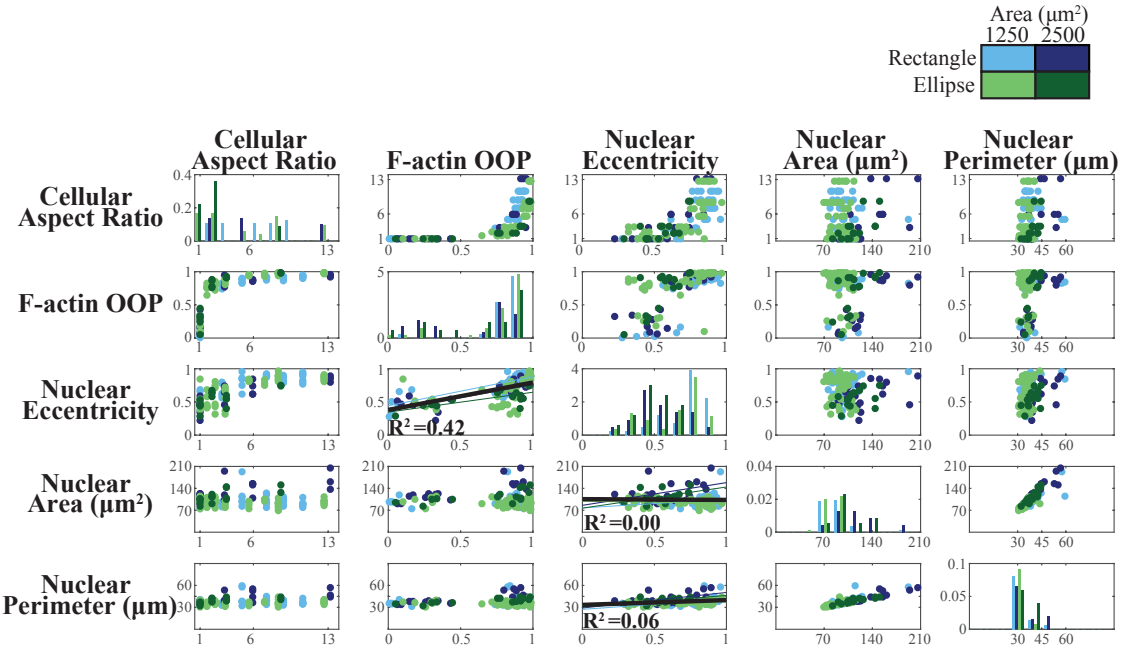

Figure 4.4: Matrix of scatter plots between features of the experimental data. Note that along the diagonal, the distributions of each feature are plotted.

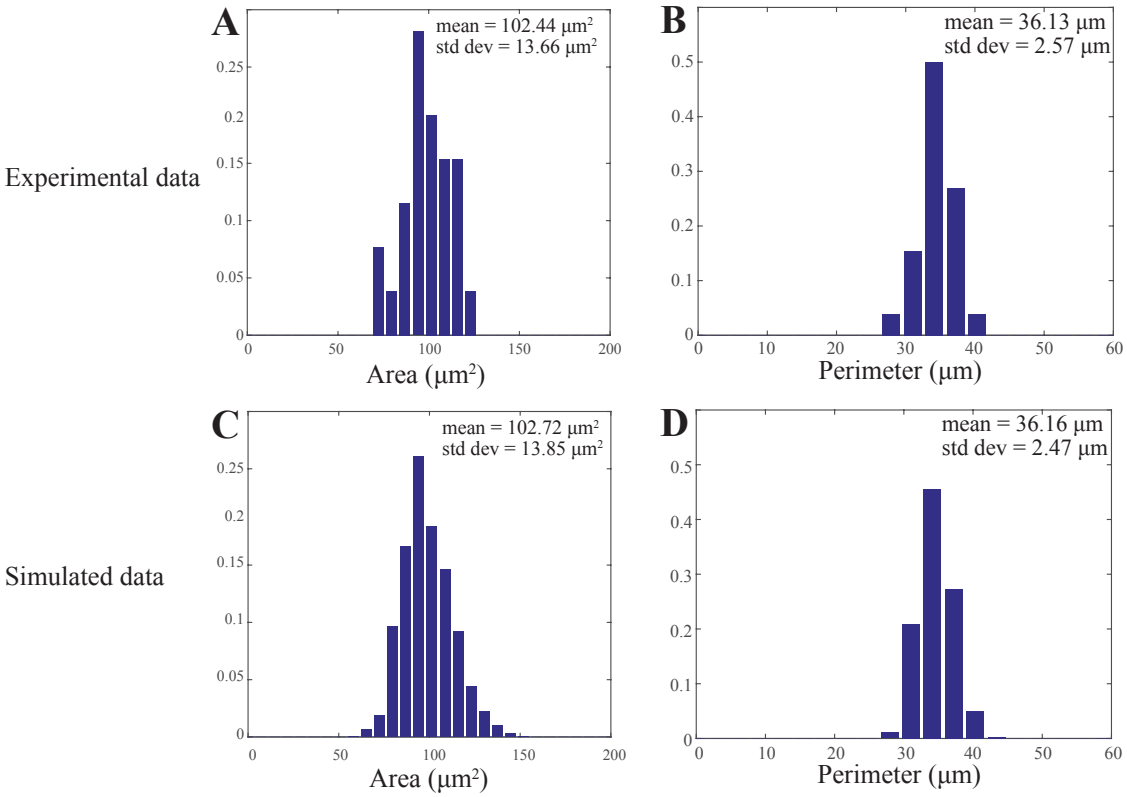

Figure 4.5: Histogram matching model to experimental data. Experimental histograms of nuclear area (A) and nuclear perimeter (B) of cell with aspect ratio 1. Simulated histograms of nuclear area (C) and nuclear perimeter (D) of simulated nuclei with no active cytoskeletal force.

4.3 Future work

The future goal of this work is to reliably reproduce nuclear shape deformations. This requires a symmetry break in the system governing laminar assembly/disassembly dynamics. This might be achieved by including a feedback term in the functions $k_{\text{off}}^{a,b}$. Hypothesized sources of feedback include competition between lamin types, and stress induced feedback. These ideas are shown schematically in Figure 4.7. Once we have established a symmetry break, one could explore perturbations to the model which correspond to physical changes in the lamin A/C protein which can best reproduce patient versus control data. These potential perturbations are summarized in Table 4.5.

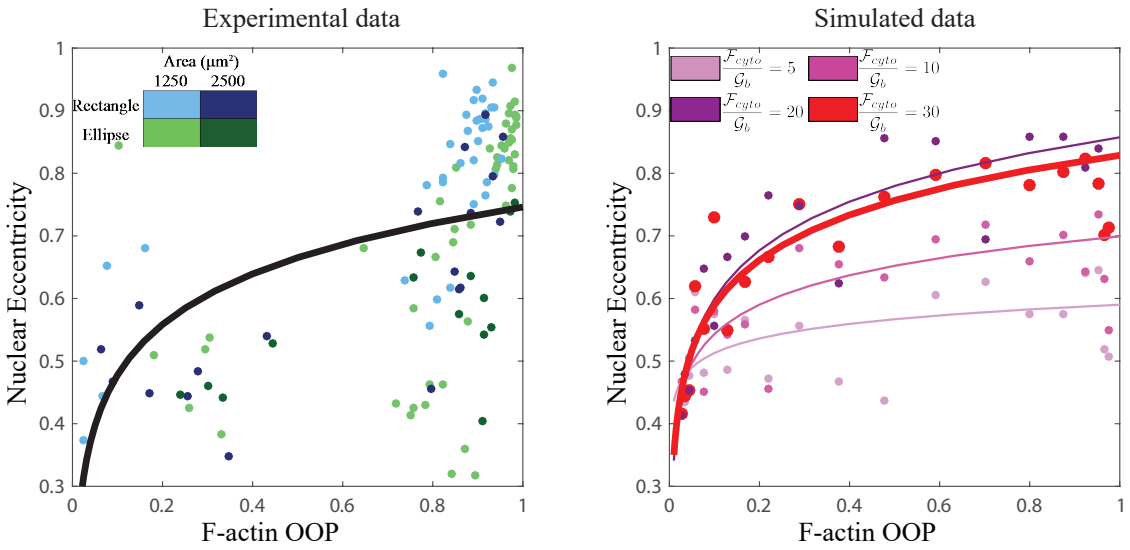

Figure 4.6: F_{cyto} was obtained by matching the correlation between F-actin OOP and nuclear eccentricity observed experimentally.

Table 4.5: Potential perturbations.

Model perturbation	Change in lamin A/C
Decrease total amount of lamin A/C	Haploinsufficiency
Modify assembly/disassembly rates	Abnormal localization of lamin
Modify $\mathcal{G}_a$ (elastic modulus)	Weaken molecular strength of Lamin A/C
Modify $\mathcal{M}_a$ (bending modulus)	Weaken Lamin A/C-Lamin A/C cross-linking
Modify $\mathcal{F}_{cyto}, \sigma_{\text{VM}}$	Weaken transmembrane link
Modify feedback from lamin B	Modify interaction with Lamin B

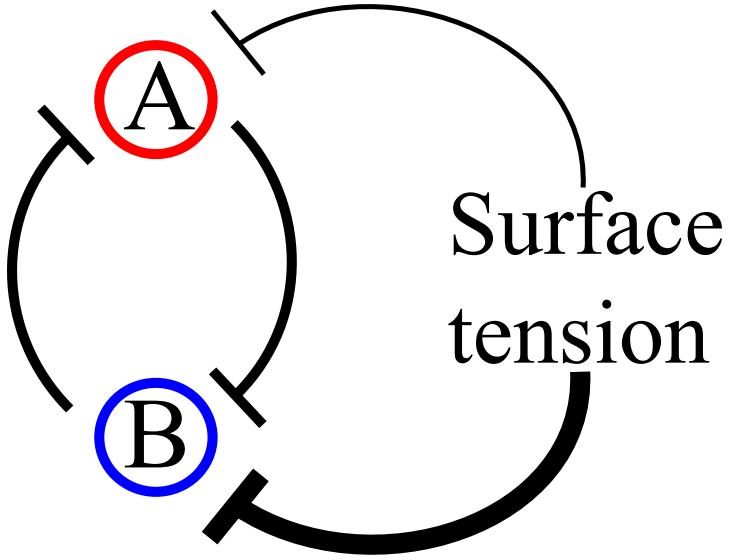

Figure 4.7: Schematic diagram of the possible sources of feedback in the model.

Chapter 5

Model of Nuclear Assembly*

5.1 Introduction

Throughout the lifetime of an organism, particularly during development when cells multiply rapidly, the nuclei must be disassembled before cell division and reassembled after, in a process known as nuclear organogenesis. It has been shown that during nuclear organogenesis, nuclei will expand to a given size and that this size scales with the size of the cell [50, 74]. The mechanisms regulating nuclear size are yet unknown. Our collaborators have used a custom microfluidics device to control for cell size and have observed the growth of the nucleus [7]. In some cases, more than one nucleus becomes fixed in a cell of a given size. From here we can make predictions about how the nucleus is expected to grow under different scaling hypotheses, as in Figure 5.1. The first hypothesis is that nuclear size is driven by genomic content. In this case, we would expect the size of the nucleus to remain constant as the cytoplasmic size varies. Furthermore, we would expect that two nuclei in

*This is the computational portion of a joint experimental-computational work posted in BioRxiv. V. Boudreau, J. Hazel, J.K. Sellinger, P.Chen, K. Manakova, R. Radzyminski, H.G. Garcia, J.Allard, J. Gatlin and P. Maddox. *Nucleo-cytoplasmic trafficking regulates nuclear surface area during nuclear organogenesis.* doi: https://doi.org/10.1101/326140 [7]

a fixed cytoplasmic volume would have twice the surface area and twice the volume, and similarly three nuclei would have 3 times the surface area and three times the volume. This would result in a constant surface area to volume ratio as the number of nuclei are varied. Alternatively, nuclear size might be regulated in a nuclear envelope-limited regime or a volumetric network-limited regime. In this case we would expect that either the total nuclear volume (volumetric network-limited regime) or total nuclear surface area (nuclear envelope-limited regime) would remain constant, as we vary the number of nuclei in a fixed cytoplasmic volume.

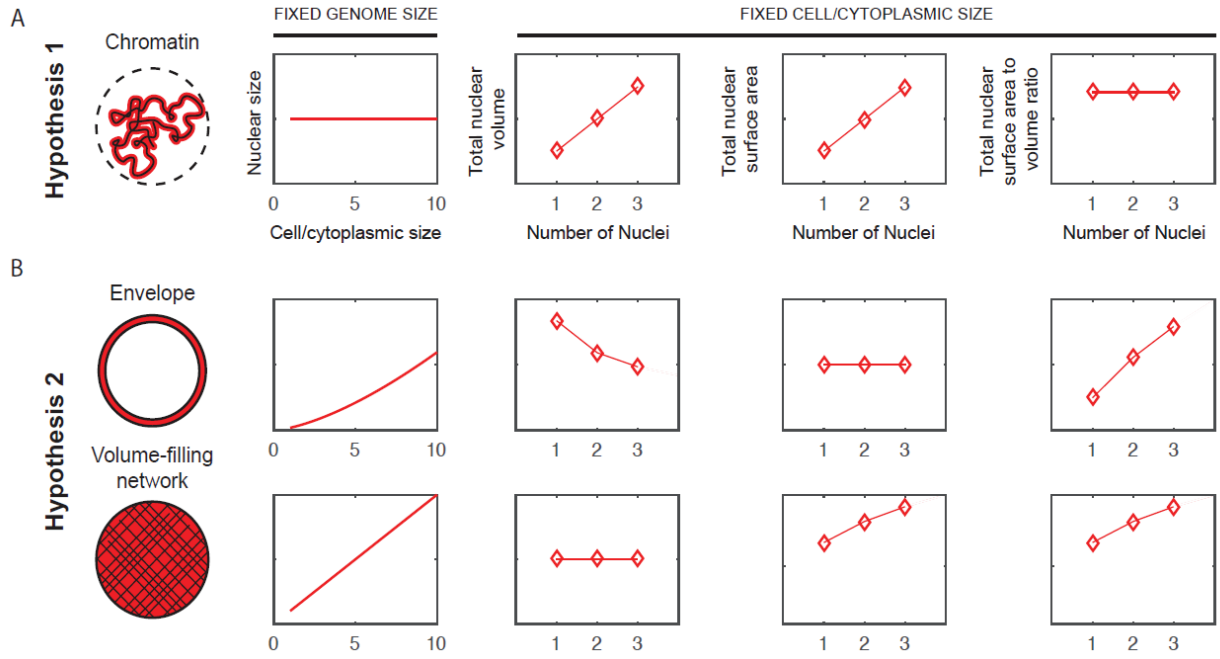

Figure 5.1: Models of nuclear size scaling within a defined cell size predict scaling relationships and nuclear surface area:volume ratios under different regimes. a) In Hypothesis 1, nuclear size is driven by genome size. As cell size/cytoplasmic size increases, nuclear size is constant as genome size is constant. By keeping cell size constant and varying the number of genomes in this regime, nuclear volume and nuclear surface area increase. b) In Hypothesis 2, nuclear size to cell size scaling is independent of genome size. Considering the nucleus as a viscoelastic material composed of a nuclear envelope and a nucleoplasmic volumetric network, nuclear size is hypothesized to be regulated in a nuclear envelope-limited regime (upper panel) or a volumetric network-limited regime (lower panel), where either nuclear surface or nuclear volume regulate nuclear size respectively.

It has been observed that nuclear size does not scale directly with nuclear volume, nuclear

surface area nor with genomic content. Here we have developed a mechano-chemical model of nuclear assembly to study the relative contributions of these three elements to the final nuclear size achieved. The model assumes both the surface factor (proteins which contribute to surface area, *e.g.* lamins) and volume factor (proteins which contribute to nuclear volume *e.g.* NuMA) are uniformly distributed throughout the cytoplasm and must be transported by passive diffusion and microtubule-associated dynein to the nuclear periphery. Once the factor is near the nucleus, it is imported to (and exported from) the nucleus, enabling nuclear growth.

5.2 Basic model equations and assumptions

5.2.1 Mechanics of the nucleus

The nuclear volume $V(t)$ and surface area $S(t)$ are both dynamic quantities. The total mechanical free energy of the nucleus, which determines nuclear shape dynamics, is itself determined by several factors. As our starting point, we assume that this energy has three dominant terms:

$$E = \Delta P_{\text{vol}} V + \Delta P_{\text{chrom}} V + \Delta P_{\text{osmo}} V + \gamma S \tag{5.2.1}$$

where P_{vol} is the hydrostatic pressure due to the hypothesized elastic volumetric network, P_{chrom} is the pressure due to chromatin, P_{osmo} is osmotic pressure, and γ is the surface tension, which includes the full nuclear envelope (membranes and lamina). These are shown in Figure 5.2 (Top). This energy drives changes to nuclear volume according to

$$\frac{dV}{dt} = -\alpha \frac{dE}{dV} \tag{5.2.2}$$

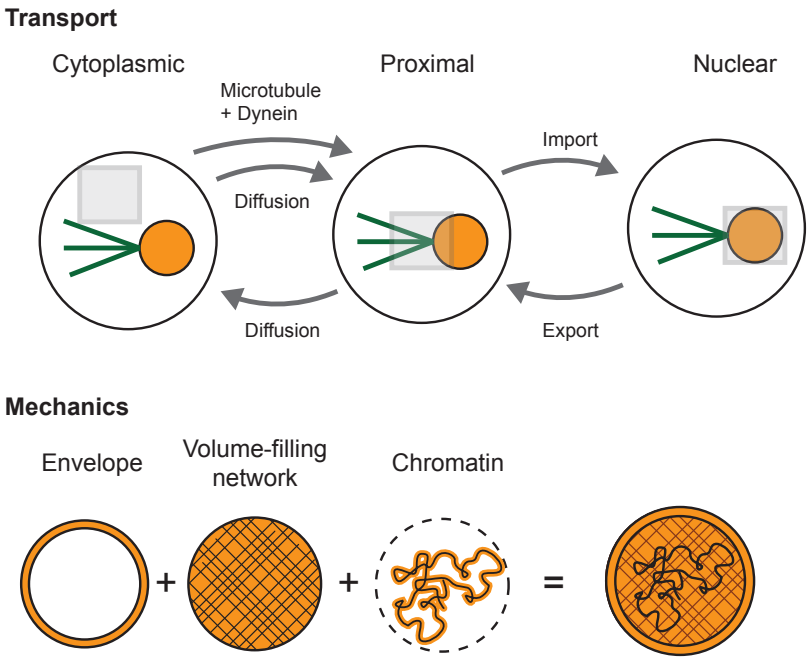

Figure 5.2: (Top) Transport of nuclear assembly factors. Simplified model with three region. Same transport mechanism is assumed for both the volume factor and surface factor. (Bottom) Mechanical factors included in model that (*a priori*) can determine nuclear size.

where α is the hydraulic permeability [53] of the nucleus, which has units of $\mathrm{nm}^3/(\mathrm{Pa}\cdot\mathrm{s})$. In words, (5.2.2) states that the nuclear volume will increase or decrease in order to minimize the free energy, at which point the three forces in (5.2.1) are in balance.

In general, the nucleus might buckle into a non-spherical shape. However, following data from [7], we first formulate the model assuming it remains approximately spherical. This approximation is valid provided we are below the buckling threshold [53]. Combining 5.2.1, 5.2.2, and the spherical approximation, we obtain

$$4\pi r^2 \frac{dr}{dt} = -\alpha \left(\Delta P_{\mathrm{vol}} + P_{\mathrm{chrom}} + \Delta P_{\mathrm{osmo}} + \frac{2\gamma}{r} \right) \tag{5.2.3}$$

where $r(t)$ is the nuclear radius. In absence of precise measurements of the permeability α, we make the reasonable assumption that α is proportional to the surface area, $\alpha = \alpha_0 4\pi r^2$

(canceling the left-hand-side prefactor).

Pressure due to confining chromatin has been estimated to satisfy [69, 88]

$$P_{\text{chrom}} = G_{\text{chrom}}/r^2 \tag{5.2.4}$$

where G_{chrom} is the chromatin compressibility modulus. We treat both the bulk inside the nucleus and the nuclear envelope as elastic materials. Therefore, they have elastic compressibility G_{vol} and extensibility G_{surf}, and the pressure and surface tension are given by

$$\Delta P_{\text{vol}} = G_{\text{vol}} \left(\frac{4}{3}\pi r^3 - V_0 \right) \tag{5.2.5}$$

$$\gamma = G_{\text{surf}} \left(4\pi r^2 - S_0 \right) \tag{5.2.6}$$

where $V_0(t)$ and $S_0(t)$ are the preferred volume and surface area, *i.e.*, the "rest" volume and "rest" area. Note that, *a priori*, we do not assume which term dominates, *i.e.*, it could be that G_{surf} is negligible compared to the bulk volume compressibility.

5.2.2 Transport of nuclear assembly factors

During nuclear assembly, material is added to the nucleus via regulated import at nuclear pore complexes (NPCs). This includes nuclear material destined to assemble throughout the nucleoplasm, such as NuMA [82], and material destined to assemble the envelope, such as lamin A/C and lamin B [38]. We generically refer to these as a nuclear volume factor f^{vol} and nuclear surface factor f^{surf}.

At the beginning of nuclear assembly, these factors have a distribution throughout the cytoplasm. As a first approximation, we divide the cytoplasmic space into two regions: distal to the nucleus and proximal to the nucleus, with volumes V_{cyto} and V_{prox} respectively. This

is shown schematically in Figure 5.2 (Bottom).

Material is transported between these regions by two mechanisms: passive diffusion, which is bi-directional, and active transport by dynein along N_{MT} centrosomal microtubules with velocity v_{dyn}. Once the factor is proximal to the nucleus, its exchange with the nucleus is regulated by NPCs with first-order kinetic rates k_{in} and k_{out} (both with units of $\mu\text{M}^{-1}\,\text{s}^{-1}$ per NPC). This leads to dynamic equations

$$\frac{df^{\text{vol}}_{\text{cyto}}}{dt} = D\left(-\frac{f^{\text{vol}}_{\text{cyto}}}{V_{\text{cyto}}} + \frac{f^{\text{vol}}_{\text{prox}}}{V_{\text{prox}}}\right) - r_{MT}N_{MT}f^{\text{vol}}_{\text{cyto}} \tag{5.2.7}$$

$$\frac{df^{\text{vol}}_{\text{prox}}}{dt} = D\left(+\frac{f^{\text{vol}}_{\text{cyto}}}{V_{\text{cyto}}} - \frac{f^{\text{vol}}_{\text{prox}}}{V_{\text{prox}}}\right) + r_{MT}N_{MT}f^{\text{vol}}_{\text{cyto}} + N_{\text{NPC}}\left(-k^{\text{vol}}_{\text{in}}\frac{f^{\text{vol}}_{\text{prox}}}{V_{\text{prox}}} + k^{\text{vol}}_{\text{out}}\frac{f^{\text{vol}}_{\text{nuc}}}{4/3\pi r^3}\right) \tag{5.2.8}$$

$$\frac{df^{\text{vol}}_{\text{nuc}}}{dt} = N_{\text{NPC}}\left(+k^{\text{vol}}_{\text{in}}\frac{f^{\text{vol}}_{\text{prox}}}{V_{\text{prox}}} - k^{\text{vol}}_{\text{out}}\frac{f^{\text{vol}}_{\text{nuc}}}{4/3\pi r^3}\right). \tag{5.2.9}$$

The diffusion parameter $D = \tilde{D}S_{\text{prox}}$ is the molecular diffusion coefficient (with units of $\text{nm}^2/\,\text{s}$) times the area of interface between the proximal cytoplasmic region and distal cytoplasmic region. The active transport parameter $r_{MT} = v_{\text{dyn}}/l_{\text{prox}}$ is the dynein velocity divided by the mean transport distance between distal and proximal cytoplasmic regions. These definitions of D and r_{MT} assume each molecule of factor is equally likely to be transported actively or by diffusion. We can adjust this assumption by decreasing either (or both) of these parameters.

Similarly for surface factor,

$$\frac{df^{\text{surf}}_{\text{cyto}}}{dt} = D\left(-\frac{f^{\text{surf}}_{\text{cyto}}}{V_{\text{cyto}}} + \frac{f^{\text{surf}}_{\text{prox}}}{V_{\text{prox}}}\right) - r_{MT}N_{MT}f^{\text{surf}}_{\text{cyto}} \tag{5.2.10}$$

$$\frac{df^{\text{surf}}_{\text{prox}}}{dt} = D\left(+\frac{f^{\text{surf}}_{\text{cyto}}}{V_{\text{cyto}}} - \frac{f^{\text{surf}}_{\text{prox}}}{V_{\text{prox}}}\right) + r_{MT}N_{MT}f^{\text{surf}}_{\text{cyto}} + N_{\text{NPC}}\left(-k^{\text{surf}}_{\text{in}}\frac{f^{\text{surf}}_{\text{prox}}}{V_{\text{prox}}} + k^{\text{surf}}_{\text{out}}\frac{f^{\text{surf}}_{\text{nuc}}}{4\pi r^2}\right) \tag{5.2.11}$$

$$\frac{df^{\text{surf}}_{\text{nuc}}}{dt} = N_{\text{NPC}}\left(+k^{\text{surf}}_{\text{in}}\frac{f^{\text{surf}}_{\text{prox}}}{V_{\text{prox}}} - k^{\text{surf}}_{\text{out}}\frac{f^{\text{surf}}_{\text{nuc}}}{4\pi r^2}\right). \tag{5.2.12}$$

Note that the nuclear amount of factor $f^{\text{surf}}_{\text{nuc}}$ scales with nuclear surface area, rather than nuclear volume.

5.3 Parameter estimation and model simplification

Instead of tracking factor amounts in numbers of molecules, we define f^0_{vol} as the amount (i.e., number of molecules) of volume factor required to assemble one unit of nuclear volume, and f^0_{surf} as the amount of surface factor required to assemble one unit of nuclear surface, and set $F_{\text{vol}} = f_{\text{vol}}/f^0_{\text{vol}}$ and $F_{\text{surf}} = f_{\text{surf}}/f^0_{\text{surf}}$. This allows us to re-write the force-balance equation 5.2.3 as

$$\frac{dr}{dt} = \alpha_0\left(G_{\text{vol}}\left(F^{\text{vol}}_{\text{nuc}} - \frac{4}{3}\pi r^3\right) + \frac{G_{\text{chrom}}}{r^2} + \frac{2G_{\text{surf}}}{r}\left(F^{\text{surf}}_{\text{nuc}} - 4\pi r^2\right) + \Delta P_{\text{osmo}}\right). \tag{5.3.1}$$

The units of k_{in} and k_{out} are now s^{-1}.

Table 5.1: Model parameters.

Parameter	Description	Xenopus	HeLa	Source / note
α_0	Per-area hydraulic permeability	$10^{-6}\mu\text{m/Pa}\cdot\text{min}$	$10^{-6}\mu\text{m/Pa}\cdot\text{min}$	[53], see 5.3.2
D	Diffusion rate parameter	$10^3\,\text{s}^{-1}$	$10^3\,\text{s}^{-1}$	Estimated (5.3.1)
N_{MT}	Number of microtubules involved in transport	50	50	Observed here
r_{MT}	Transport rate for microtubule-based delivery	$10^{-3}\,\text{s}^{-1}$	$3\times10^{-4}\,\text{s}^{-1}$	Fit (5.4.3)
G_{vol}	Volumetric factor bulk modulus	$10^4\text{Pa}/\,\mu\text{m}^3$	$5\times10^6\text{Pa}/\,\mu\text{m}^3$	Fit (5.4.2)
G_{chrom}	Chromatin confinement coefficient	$10^9\text{Pa}\,\mu\text{m}^2$	$10^9\text{Pa}\,\mu\text{m}^2$	Fit (5.4.2)
G_{surf}	Surface factor elastic modulus	$5\times10^3\text{pN}/\,\mu\text{m}^3$	$5\times10^3\text{pN}/\,\mu\text{m}^3$	Fit (5.4.2)
V_{cyto}	Volume of cytoplasm, distal region	$6.5\times10^4(\,\mu\text{m}^3)$	$4\times10^3\,\mu\text{m}^3$	Measured
V_{prox}	Volume of nuclear proximal region	$3\times10^3\,\mu\text{m}^3$	$10^3\,\mu\text{m}^3$	Arbitrary
N_{NPC}	Number of nuclear pore complexes	3×10^3	3×10^3	[13]
$k_{\text{in}}^{\text{surf}}$	Import rate of surface factor	$0.25\,\text{s}^{-1}$	$10^{-3}\,\text{s}^{-1}$	Fit (5.4.4)
$k_{\text{out}}^{\text{surf}}$	Export rate of surface factor	$0.05\,\text{s}^{-1}$	$10^{-6}\,\text{s}^{-1}$	Fit (5.4.4)
$k_{\text{in}}^{\text{vol}}$	Import rate of volume factor	$0.65\,\text{s}^{-1}$	$8\times10^{-2}\,\text{s}^{-1}$	Fit (5.4.2)
$k_{\text{out}}^{\text{vol}}$	Export rate of volume factor	$0.05\,\text{s}^{-1}$	$8\times10^{-3}\,\text{s}^{-1}$	Fit (5.4.2)
$F_{\text{tot}}^{\text{vol}}$	Total amount of volume factor	$8\times10^3\,\mu\text{m}^3$	$1.5\times10^3\,\mu\text{m}^3$	Estimated
$F_{\text{tot}}^{\text{surf}}$	Total amount of surface factor	$1.1\times10^4\,\mu\text{m}^2$	$1.1\times10^4\,\mu\text{m}^2$	Estimated

5.3.1 Diffusional delivery rate in cytoplasm to nuclear periphery

We split the cytoplasm into two regions, which we term the cytoplasm (distal to the nucleus) and the proximal region (the nuclear periphery). Diffusive transport between two regions obeys the diffusion equation that simplifies, for the case of two compartments, to

$$\frac{df_1}{dt} \approx a\tilde{D}\left(\frac{c_2 - c_1}{L}\right) = a\frac{\tilde{D}}{L}\left(\frac{f_2}{V_2} - \frac{f_1}{V_1}\right), \tag{5.3.2}$$

where $\tilde{D}$ is the true diffusion coefficient, estimated to be $10\mu\text{m}^2/s$ [45], and c_i is the concentration, f_i is the factor, and V_i is the volume of a given region. L denotes the length over which factor is transported and a is the cross-sectional area separating the regions. To apply this to our cytoplasmic systems, we define $L \approx r_{\text{cell}}$ and $a \approx r_{\text{prox}}^2$. This leads to

$$\frac{df_1}{dt} = \frac{r_{\text{prox}}^2}{r_{\text{cell}}}\tilde{D}\left(\frac{f_2}{V_2} - \frac{f_1}{V_1}\right) \tag{5.3.3}$$

$$= D\left(\frac{f_2}{V_2} - \frac{f_1}{V_1}\right), \tag{5.3.4}$$

where we have defined the diffusion rate parameter

$$D \equiv \frac{r_{\text{prox}}^2}{r_{\text{cell}}}\tilde{D}. \tag{5.3.5}$$

Using $r_{\text{prox}} \approx$ 10-100μm and $r_{\text{cell}} \approx$ 100-10$^3\mu$m, we obtain $D = 10^4\mu\text{m}^3/\text{min}$. This leads us to estimate that $D = 10^3 - 10^5\mu\text{m}^3/\text{min}$.

5.3.2 Hydraulic permeability of nuclear envelope

To estimate the per-area hydraulic permeability α_0, we refer to Kim et al. [53], where α is a constant of proportionality between change in volume and pressure, i.e., $dV/dt = \alpha\Delta P$. They find parameter values $V_{N0} = 805\mu\text{m}^3$, $\overline{\alpha} = 3 \times 10^{-3}\text{min}^{-1}$, and $\mu = 10^4$ Pa, related to

the permeability by their equation

$$\overline{\alpha} = \frac{\alpha\mu}{V_{N0}}. \tag{5.3.6}$$

If the nucleus is spherical, as we assume in this model, the per-area hydraulic permeability is $\alpha = \alpha_0 4\pi r^2$. Combining this with equations

$$\alpha_0 = \frac{\alpha}{4\pi r^2} = \frac{\overline{\alpha} V_{N0}}{\mu 4\pi r^2} \tag{5.3.7}$$

$$\sim 10^{-7} \frac{\mu\mathrm{m}}{\mathrm{Pa}\cdot\mathrm{min}}. \tag{5.3.8}$$

We find that this value of α_0 is large enough that water import and mechanical equilibration is fast enough (during assembly) that nuclear growth is limited by other factors, specifically transport of material to the nuclear periphery and import of this material into the nucleus.

5.4 Simulation results

5.4.1 Numerical simulation of model and fitting to experimental data

We simulate the model, which is a systems of 7 ordinary differential equations given by (5.3.1) and (5.2.7-5.2.12), with 15 parameters. We begin simulating at $t = 0$, which we identify as the anaphase-to-telophase transition, after the nuclear envelope is sufficiently formed so that transport in and out is regulated via nuclear pore complexes. At this time, we observe that the nucleus has size $r(0) = r_0 = 4.18\,\mu$m. We assume that it is in mechanical equilibrium with $f_{nuc}^{\mathrm{vol}}(0) = 4/3\pi r_0^3$ and $f_{nuc}^{\mathrm{surf}}(0) = 4\pi r_0^2$, and that an equal concentration of the remaining factor are in the proximal and distal cytoplasmic pools. Of the 15 parameters, 6 are well-

constrained by direct observation or by estimated from the literature, see Table 5.1. We explore ranges for the remaining 8 parameters as discussed in the sections below. From the seven dynamic variables (nuclear radius, and surface factor and volume factor amounts in each of three spatial compartments), we can further compute nuclear surface area, cross-sectional area and volume, and the concentration (amount per volume) of surface and volume factors. A sample time series produced by the simulation is shown in Figure 5.3.

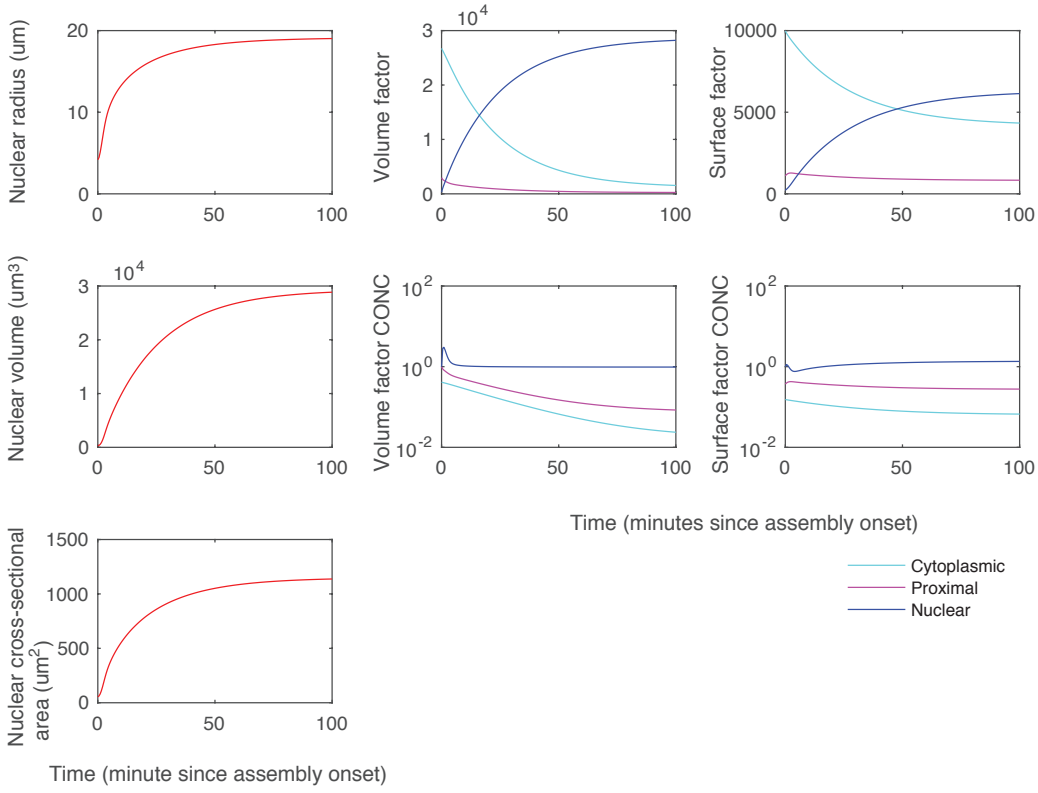

Figure 5.3: Sample time series produced by the simulation.

5.4.2 Continuum of behavior between volume-dominated and surface-dominated regimes

We modify the model so that N_{nuc} nuclei share a common peripheral space and common pools of surface and volume factors. We then simulate the model until it reaches a steady state. The parameters with the least-well constrained values are the three mechanical moduli, specifically the surface factor compressibility G_{vol}, the surface factor compressibility G_{surf}, and the chromatic confinement coefficient G_{chrom}, so we perform exploration in these three parameters.

We first explore the model under the hypothesis that nuclear size is determined by a competition between volume and surface factors, without contribution from genomic content. We do this by setting the chromatin confinement coefficient $G_{\text{chrom}} = 0$. Resulting nuclear scaling is shown in Figure 5.4. When the volume factor modulus is low compared to surface factor modulus (left top and bottom), the total nuclear surface area is constant. This necessarily implies a decreasing total nuclear volume. When the volume factor modulus is high compared to the surface factor modulus (right top and bottom), the total surface volume is constant. This necessarily implies an increasing total nuclear surface area. Note that this model cannot give rise to total nuclear volume that increases with number of nuclei. For this reason, our simulations argue against this hypothesis.

We next simulate the model under the hypothesis that nuclear size is determined by a competition between surface factor, volume factor and chromatin, as shown in Figure 5.5. To match the nuclear sizes in obtain in experiments by our collaborators, we find best-fit parameters shown in Table 5.1. We find that agreement arises when the surface factor modulus is low, and therefore nuclear size is primarily determined by the remaining two factors, volume factor and chromatin.

To match the growth speed, i.e., the approach to this steady state, observed in Xenopus, we

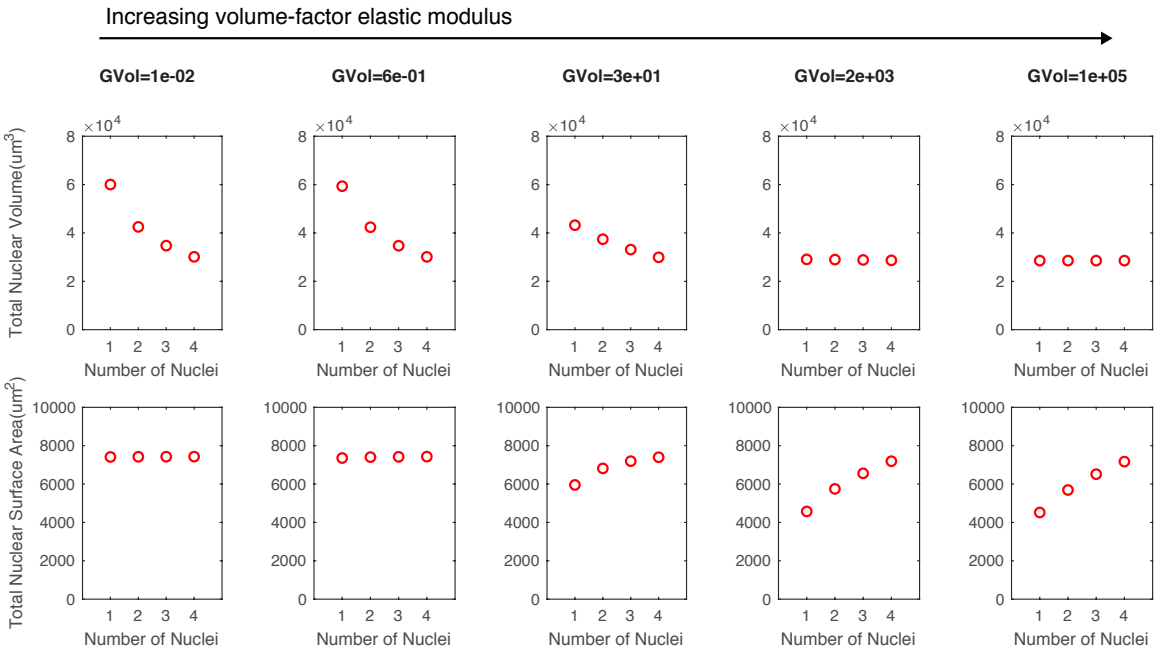

Figure 5.4: Nuclear size scaling as the ratio of G_{vol} (units of $\text{Pa}/\,\mu\text{m}^3$)) to G_{surf} ($\text{pN}/\,\text{nm}^3$), with no chromatin effect ($G_{\text{chrom}} = 0$).

find that $k_{\text{in}}^{\text{vol}} \sim 0.65\,\text{s}^{-1}$. Note that the growth speed is approximately independent of $k_{\text{in}}^{\text{surf}}$ since the system is close to the volume-limited regime.

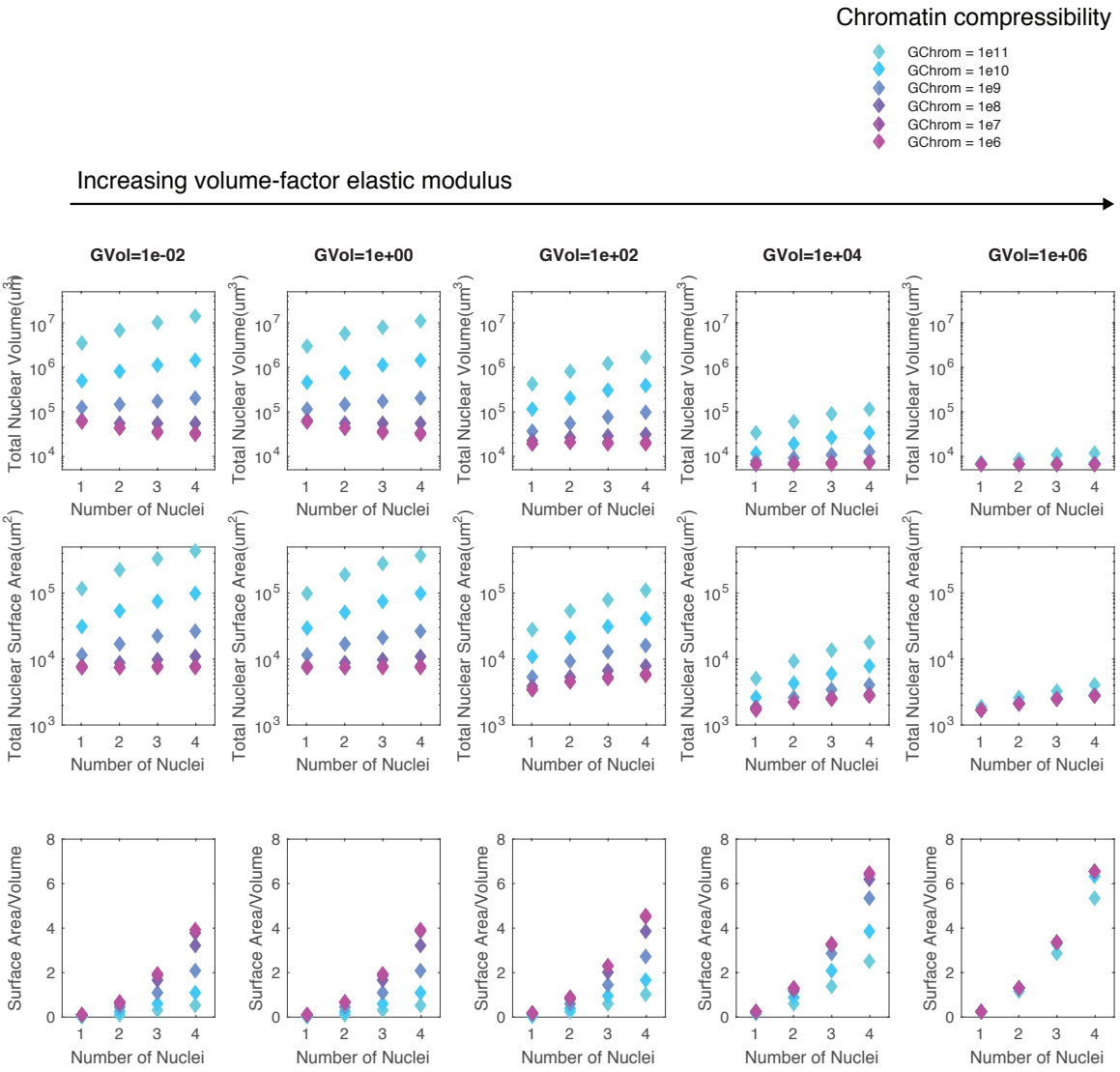

Figure 5.5: Nuclear size scaling with $G_{\text{chrom}} = 0$ (purple) and for increasing G_{chrom} (units of $\text{Pa} \cdot \mu\text{m}^2$, color axis). Note the log scale.

5.4.3 Roles of diffusive and active delivery to nuclear periphery

Experiments have shown that inhibition of microtubule/dynein-based transport, e.g., using nocodazole, reduce the nuclear volume by approximately half [41]. Roughly speaking, this suggests that half of delivery to the nuclear periphery is based on this active mechanism and, in the context of this model, suggests the remaining half of delivery is due to passive diffusion. In Figure 5.6, we simulate the model with $N_{\mathrm{MT}} = 0$ to mimic the nocodazole experiment (red curve and bar). We then simulate the control $N_{\mathrm{MT}} = 50$ and find that, to reproduce the two-fold change, we must assume a per-microtubule delivery rate of r_{MT} $10^{-3}\,\mathrm{s}^{-1}$.

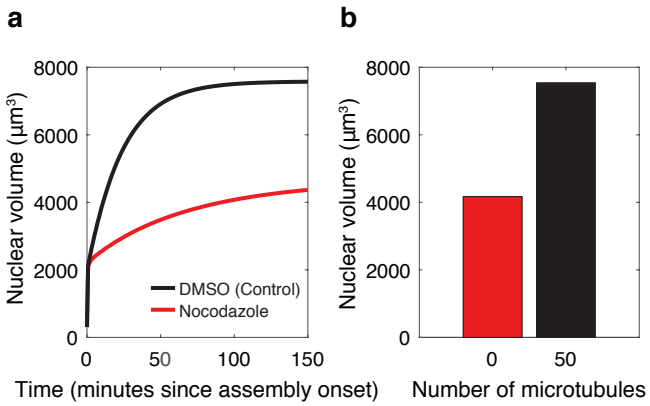

Figure 5.6: Microtubule/dynein-based transport inhibition implies relative importance of diffusive to active transport of material to nuclear-proximal region. (a) Steady-state nuclear size with and without microtubule/dynein-based transport. This constrains the parameter for microtubule/dynein transport rate, r_{MT} $10^{-3}\,\mathrm{s}^{-1}$. (b) Time series of nuclear volume with and without microtubule/dynein-based transport.

5.4.4 Nuclear export inhibition in HeLa

Finally, we simulate the inhibition of nuclear export through nuclear pore complexes by reducing $k_{\mathrm{out}}^{\mathrm{surf}}$ and $k_{\mathrm{out}}^{\mathrm{vol}}$ by half. In agreement with intuition, this leads to larger nuclear size. However, counter-intuitively, this leads to a decrease in the concentration of surface factor in the nucleus, see Figure 5.7.

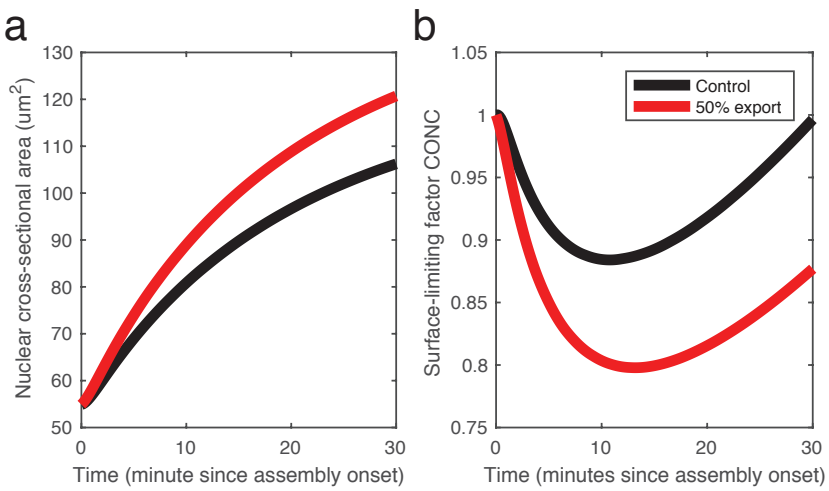

Figure 5.7: Export inhibition leads to larger nucleus size but lower concentration of surface factor in the nucleus. a) Nuclear radius as a function of time. b) Nuclear surface factor concentration over time.

We note that although the time series shown are for specific choices of parameters, this behavior is generic under two conditions: First, if the nucleus is volume-limited, and second, if the the surface factor is import-dominated or, in the language of biochemistry, has a high affinity for the nucleus. In these two cases, reducing export leads to a larger nucleus because more volume factor is imported. Meanwhile, since all of the surface factor was already in the nucleus, the export inhibition cannot lead to more surface factor. Instead, the same amount is distributed over a larger volume, thus reducing its concentration.

At these parameters, at early times, the concentration of surface factor initially drops. At these times, the nucleus is small, therefore relatively small increases in size lead to dilution of surface factor and thus decrease in its concentration.

5.5 Discussion

Here we have explicitly dissected nuclear volume, nuclear surface area and cell size scaling relationships by altering the number of nuclei in a defined cytoplasmic volume. In [7] it was found that none of nuclear surface area, nuclear volume nor genomic content scale directly with cell size. Here, we developed a mathematical model based on prior biochemical knowledge that is dependent on microtubule and dynein-based cargo transport, nucleo-cytoplasmic trafficking, hydrostatic pressure, osmotic pressure and nuclear envelope surface tension. Our model recapitulates nuclear expansion and the scaling relationship between nuclear surface area and cell size observed in vitro [7].

Chapter 6

Discussion

In this dissertation, we discuss four projects related to biological membranes and their interactions with protein networks. Each of the projects is discussed separately in the following four paragraphs.

Because of their mechanical nature, cellular blebs inform us about general cell surface mechanics including membrane dynamics, pressure propagation throughout the cytoplasm, and the architecture and dynamics of the actin cortex. Mathematical models including detailed fluid dynamics have previously been used to understand bleb expansion. In Chapter 2, we developed mathematical models on longer timescales that recapitulate the full bleb life cycle, including both expansion and healing by cortex reformation in 2D and 3D, in terms of experimentally accessible biophysical parameters such as myosin contractility, osmotic pressure, and turnover of actin and ezrin. The model provides conditions under which blebbing occurs, and naturally gives rise to traveling blebs. The model predicts conditions under which blebs travel or remain stationary, and predict the bleb traveling velocity, a quantity that has remained elusive in previous models. As previous studies have used blebs as reporters of membrane tension and pressure dynamics within the cell, we have used our system to inves-

tigate various pressure equilibration models and dynamic, non-uniform membrane tension to account for the shape of a traveling bleb. We also find that traveling blebs tend to expand in all directions unless otherwise constrained, suggesting the importance of cell surface heterogeneity. This was the main challenge of this project (breaking symmetry within our system). This is a feature central to the field of cell polarization and there has been much effort dedicated to understanding the mechanism by which this occurs both theoretically and experimentally [36]. This work has been published in Biophysical Journal [Manakova et al. *Cell surface mechanochemistry and the determinants of bleb formation, healing, and travel velocity.* Biophys J, 110 (2016), pp. 1636-1647].

The types of equations which arise from this type of biomechanical modeling are often non-classical and therefore little is known about them in general. In Chapter 3, we elucidated some features of one particular class of equations arising from our bleb model. An important element in our bleb model is the existence of travelling wave solutions. For some classical mathematical models, for example reaction-diffusion systems, the conditions allowing for travelling waves solutions are well established. This is not the case for our non-diffusion-like system of equations and therefore we are studying the existence of traveling wave solution for our non-local class of models. We derive a necessary condition for the existence of traveling wave solution and demonstrate sufficiency numerically. We used classic tools of mathematical analysis such as bifurcation analysis, and characterized the transitions between the types of solutions. We found that our system exhibits a Hopf bifurcation in conjunction with what is known as a canard explosion. Canard explosions are characterized by a sudden jump from a single steady state solution to large amplitude oscillations for very small changes in the bifurcation parameter. These types of analyses can be applied to a wide range of non-local models in biology. Non-local models frequently arise in the field of ecological population dynamics as in [37, 112], as well as in neural field models [103, 102].

An important application of these mechano-chemical models is to the identification of altered

protein mechanics in disease states. Often diseases can be linked to a genetic mutation, but the specific effects that the mutation has on the gene product is much more difficult to resolve. We collaborated with the Grosberg and Zaragoza labs to study a mutation in LMNA gene which codes for the lamin A/C proteins. Lamin A/C proteins perform many functions in the nucleus, including localizing to the nuclear lamina, a network of proteins associated with the nuclear membrane which is thought to provide mechanical support to the nucleus. Patients with a mutated LMNA gene can suffer from a variety of disorders, collectively termed laminopathies. A common feature of all laminopathies is altered nuclear shape containing more bumps or "blebs." Nuclear blebs are also found in normal cells to some extent and a key step in learning about the mechanisms of the ensuing diseases is to understand how much nuclear defect is due to normal cell to cell variability and how much is due to the mutation. The underlying mechanism responsible for producing these nuclear defects is unknown. We developed a mathematical model of the nuclear lamina in 2D. We include mechanical properties such as surface tension, bending rigidity, and cytoskeletal forces. These laminar mechanical properties come from the mechanical properties of the lamin protein itself. Using this model we have developed a pipeline to infer unknown parameter values (representing biophysical properties) from measurable ones. This will help to identify which particular mechanical defect explains the differences we observe between patient and control cells. In [32], the authors use a similar technique by using a model to connect an external applied force to the internal turgor pressure of Arabidopsis cells, *in vivo*, thereby disentangling it from the mechanical response of the cell wall.

Nuclear organogenesis is a crucial part of cell development, however the mechanisms regulating nuclear assembly are unknown. In particular, it is unclear how the nucleus develops to a particular size. In general, it is known that nuclear size tends to scale with cell size. In Chapter 5, we used a mathematical model to explore to the relative influences of nuclear volume, nuclear surface area and genomic content on the size of the nucleus. The model assumes a uniform cytoplasmic distribution of all factors contributing to nuclear volume and

surface area. These factors move towards the nucleus through a combination of diffusion and microtubule-associated dynein whereupon they are imported to the nucleus at a particular rate. By matching to data collected by our collaborators, we explored the relative influences of various forces and mechanical properties of the nucleus in regulating its final size. We have found that nuclear size is primarily determined by volume factors and chromatin (genomic content) and less so by nuclear surface factors. Similar models may be applied to a wide range of biological systems as size control is an prominent feature at all scales of the biological world. At all stages of development, the sizes of organelles, cells, tissues, organs must be tightly regulated to ensure proper function. Misregulation of size at different scales often coincides with disease [100].

While these project contain many similarities, they are distinct in terms of the goals they are designed to achieve as well as the corresponding data available. Our project on cellular blebs sought to elucidate the mechanisms behind bleb formation, expansion and healing in both time and in space. By modeling only a small patch of space, we were able to to reduce the dimensionality of a fundamentally 3D phenomenon down to 2D and 1D, while maintaining the qualitative properties of the system. This reduction then enabled us to perform the analyses of Chapter 3. On the other hand, the data on nuclear shapes in Chapter 4 is 3D in nature, but contained no temporal information. Therefore, our modeling strategy was different in that we were able to ignore time dynamics completely and model the system at steady state. The data available for the the nuclear assembly project of Chapter 5 was also 3D in nature, but in this case we were able to exploit to reported spherical symmetry of the system and describe the size of the nucleus by a single variable, the radius. The main goal of the nuclear shape project of Chapter 4 was to identify molecular defects, represented in the model as biophysical parameters, which may contribute to the nuclear shape abnormalities observed in the disease states. For this reason, it was important for us to use the model to infer physiological values of those parameters. In contrast, the goal of the nuclear assembly project was to determine the relative influences of the various forces

on the nucleus in determining its overall size, rather than absolute physiological values.

Bibliography

[1] Ricard Alert, Jaume Casademunt, Jan Brugués, and Pierre Sens. Model for Probing Membrane-Cortex Adhesion by Micropipette Aspiration and Fluctuation Spectroscopy. *Biophysj*, 108(8):1878–1886, apr 2015.

[2] Jun Allard and Alex Mogilner. Traveling waves in actin dynamics and cell motility. *Current Opinion In Cell Biology*, 25(1):1–9, sep 2012.

[3] Jun F Allard, Omer Dushek, Daniel Coombs, and P Anton Van Der Merwe. Mechanical Modulation of Receptor-Ligand Interactions at Cell-Cell Interfaces. *Biophysical Journal*, 102(6):1265–1273, mar 2012.

[4] David A Baum and Buzz Baum. An inside-out origin for the eukaryotic cell. *BMC biology*, 12(1):76, 2014.

[5] William M Bement, Marcin Leda, Alison M Moe, Angela M Kita, Matthew E Larson, Adriana E Golding, Courtney Pfeuti, Kuan-Chung Su, Ann L Miller, Andrew B Goryachev, and Others. Activator-inhibitor coupling between Rho signalling and actin assembly makes the cell cortex an excitable medium. *Nature Cell Biology*, 2015.

[6] Maté Biro, Yves Romeo, Sonja Kroschwald, Miia Bovellan, Annett Boden, Joseph Tcherkezian, Philippe P Roux, Guillaume Charras, and Ewa K Paluch. Cell cortex composition and homeostasis resolved by integrating proteomics and quantitative imaging. *Cytoskeleton (Hoboken, N.J.)*, 70(11):741–754, nov 2013.

[7] Vincent Boudreau, James Hazel, Jacob K Sellinger, Pan Chen, Kathryn Manakova, Rochelle Radzyminski, Hernan G Garcia, Jun Allard, Jesse Gatlin, and Paul S Maddox. Nucleo-cytoplasmic trafficking regulates nuclear surface area during nuclear organogenesis. *bioRxiv*, page 326140, 2018.

[8] Miia Bovellan, Yves Romeo, Maté Biro, Annett Boden, Priyamvada Chugh, Amina Yonis, Malti Vaghela, Marco Fritzsche, Dale Moulding, Richard Thorogate, Antoine Jégou, Adrian J Thrasher, Guillaume Romet-Lemonne, Philippe P Roux, Ewa K Paluch, and Guillaume Charras. Cellular Control of Cortical Actin Nucleation. *Current biology : CB*, 24(14):1628–1635, jul 2014.

[9] N F Britton. Threshold phenomena and solitary traveling waves in a class of reaction-diffusion systems. *Siam Journal on Applied Mathematics*, 1982.

[10] N. F. Britton. Threshold Phenomena and Solitary Traveling Waves in a Class of Reaction-Diffusion Systems. *SIAM Journal on Applied Mathematics*, 42(1):188, 1982. ISSN 00361399. doi: 10.1137/0142015. URL `http://link.aip.org/link/SMJMAP/v42/i1/p188/s1{&}Agg=doi`.

[11] Brian C. Capell and Francis S. Collins. Human laminopathies: nuclei gone genetically awry. *Nature Reviews Genetics*, 7(12):940–952, 2006. ISSN 1471-0056. doi: 10.1038/nrg1906. URL `http://www.nature.com/doifinder/10.1038/nrg1906`.

[12] Andreas Carlson and L Mahadevan. Elastohydrodynamics and kinetics of protein patterning in the immunological synapse. may 2015.

[13] Bastien Cautain, Richard Hill, Nuria De Pedro, and Wolfgang Link. Components and regulation of nuclear transport processes, 2015. ISSN 17424658.

[14] G T Charras. A short history of blebbing. *Journal of microscopy*, 231(3):466–478, sep 2008.

[15] Guillaume Charras and Ewa Paluch. Blebs lead the way: how to migrate without lamellipodia. *Nature Reviews Molecular Cell Biology*, 9(9):730–736, sep 2008.

[16] Guillaume T Charras, Justin C Yarrow, Mike A Horton, L Mahadevan, and T J Mitchison. Non-equilibration of hydrostatic pressure in blebbing cells. *Nature*, 435 (7040):365–369, may 2005.

[17] Guillaume T Charras, Margaret Coughlin, Timothy J Mitchison, and L Mahadevan. Life and times of a cellular bleb. *Biophysical Journal*, 94(5):1836–1853, mar 2008.

[18] Guillaume T Charras, Timothy J Mitchison, and L Mahadevan. Animal cell hydraulics. *Journal of Cell Science*, 122(Pt 18):3233–3241, sep 2009.

[19] Andrew G Clark, Kai Dierkes, and Ewa K Paluch. Monitoring Actin Cortex Thickness in Live Cells. *Biophysj*, 105(3):570–580, aug 2013.

[20] Andrew G Clark, Ortrud Wartlick, Guillaume Salbreux, and Ewa K Paluch. Stresses at the Cell Surface during Animal Cell Review Morphogenesis. *Current biology : CB*, 24(10):R484—-R494, may 2014.

[21] Jason Q Core, Mehrsa Mehrabi, Zachery R Robinson, Alexander R Ochs, Linda A McCarthy, Michael V Zaragoza, and Anna Grosberg. Age of heart disease presentation and dysmorphic nuclei in patients with lmna mutations. *PloS one*, 12(11):e0188256, 2017.

[22] Gaudenz Danuser, Jun Allard, and Alex Mogilner. Mathematical Modeling of Eukaryotic Cell Migration: Insights Beyond Experiments. *Annual Review of Cell and Developmental Biology*, 29(1):130802122809007, nov 2012.

[23] Marc Diener. The canard unchained or how fast/slow dynamical systems bifurcate. *The Mathematical Intelligencer*, 1984. ISSN 03436993. doi: 10.1007/BF03024127.

[24] Terrence M Dobrowsky, Brian R Daniels, Robert F Siliciano, Sean X Sun, and Denis Wirtz. Organization of Cellular Receptors into a Nanoscale Junction during HIV-1 Adhesion. *PLoS Computational Biology*, 6(7):e1000855, jul 2010.

[25] Nancy K. Drew, Nicholas E. Johnsen, Jason Q. Core, and Anna Grosberg. Multiscale Characterization of Engineered Cardiac Tissue Architecture. *Journal of Biomechanical Engineering*, 138(11):111003, 2016. ISSN 0148-0731. doi: 10.1115/1.4034656. URL `http://biomechanical.asmedigitalcollection.asme.org/article.aspx?doi=10.1115/1.4034656`.

[26] L Edelstein-Keshet. Mathematical models in biology. 1988.

[27] John Edward and E Mathematical. *Mathematical Modelling of Cell Aggregation in Liver Tissue Engineering*. PhD thesis, 2006.

[28] R. A. FISHER. the Wave of Advance of Advantageous Genes. *Annals of Eugenics*, 7(4):355–369, 1937. ISSN 20501420. doi: 10.1111/j.1469-1809.1937.tb02153.x. URL `http://doi.wiley.com/10.1111/j.1469-1809.1937.tb02153.x`.

[29] Richard FitzHugh. Impulses and Physiological States in Theoretical Models of Nerve Membrane. *Biophysical Journal*, 1(6):445–466, 1961. ISSN 00063495. doi: 10.1016/S0006-3495(61)86902-6. URL `http://dx.doi.org/10.1016/S0006-3495(61)86902-6`.

[30] Richard FitzHugh. Impulses and Physiological States in Theoretical Models of Nerve Membrane. *Biophysical Journal*, 1(6):445–466, jul 1961.

[31] Ben Fogelson and Alex Mogilner. Computational Estimates of Membrane Flow and Tension Gradient in Motile Cells. *PLoS ONE*, 9(1):e84524, jan 2014.

[32] Elham Forouzesh, Ashwani Goel, Sally A. MacKenzie, and Joseph A. Turner. In vivo extraction of Arabidopsis cell turgor pressure using nanoindentation in conjunction with finite element modeling. *Plant Journal*, 2013. ISSN 09607412. doi: 10.1111/tpj.12042.

[33] Peter Friedl and Katarina Wolf. Tumour-cell invasion and migration: diversity and escape mechanisms. *Nature Reviews Cancer*, 3(5):362–374, may 2003.

[34] Marco Fritzsche, Richard Thorogate, and Guillaume Charras. Quantitative Analysis of Ezrin Turnover Dynamics in the Actin Cortex. *Biophysj*, 106(2):343–353, jan 2014.

[35] N Fujinami and T Kageyama. Circus movement in dissociated embryonic cells of a teleost, Oryzias latipes. *Journal of Cell Science*, 19(1):169–182, oct 1975.

[36] Andrew B. Goryachev and Marcin Leda. Many roads to symmetry breaking: molecular mechanisms and theoretical models of yeast cell polarity. *Molecular Biology of the Cell*, 2017. ISSN 1059-1524. doi: 10.1091/mbc.E16-10-0739.

[37] S. A. Gourley, M. A. J. Chaplain, and F. A. Davidson. Spatio-temporal pattern formation in a nonlocal reaction-diffusion equation. *Dynamical Systems*, 16(2):173–192, 2001. ISSN 1468-9367. doi: 10.1080/14689360116914. URL `http://www.tandfonline.com/doi/abs/10.1080/14689360116914`.

[38] Yosef Gruenbaum and Roland Foisner. Lamins: Nuclear Intermediate Filament Proteins with Fundamental Functions in Nuclear Mechanics and Genome Regulation. *Annual Review of Biochemistry*, 2015. ISSN 0066-4154. doi: 10.1146/annurev-biochem-060614-034115.

[39] Edouard Hannezo, Bo Dong, Pierre Recho, Jean-François Joanny, and Shigeo Hayashi. Cortical instability drives periodic supracellular actin pattern formation in epithelial tubes. *Proceedings Of The National Academy Of Sciences Of The United States Of America*, 112(28):8620–8625, jul 2015.

[40] Farhana Haque, Daniela Mazzeo, Jennifer T. Patel, Dawn T. Smallwood, Juliet A. Ellis, Catherine M. Shanahan, and Sue Shackleton. Mammalian SUN protein interaction networks at the inner nuclear membrane and their role in laminopathy disease processes. *Journal of Biological Chemistry*, 285(5):3487–3498, 2010. ISSN 00219258. doi: 10.1074/jbc.M109.071910.

[41] Yuki Hara and Christoph A. Merten. Dynein-Based Accumulation of Membranes Regulates Nuclear Expansion in Xenopus laevis Egg Extracts. *Developmental Cell*, 2015. ISSN 18781551. doi: 10.1016/j.devcel.2015.04.016.

[42] W Helfrich. *Elastic properties of lipid bilayers: theory and possible experiments.* Zeitschrift f{ü}r Naturforschung. Teil C: Biochemie, 1973.

[43] C. Y. Ho and J. Lammerding. Lamins at a glance. *Journal of Cell Science*, 125 (9):2087–2093, 2012. ISSN 0021-9533. doi: 10.1242/jcs.087288. URL `http://jcs.biologists.org/cgi/doi/10.1242/jcs.087288`.

[44] Andrew R Houk, Alexandra Jilkine, Cecile O Mejean, Rostislav Boltyanskiy, Eric R Dufresne, Sigurd B Angenent, Steven J Altschuler, Lani F Wu, and Orion D Weiner. Membrane Tension Maintains Cell Polarity by Confining Signals to the Leading Edge during Neutrophil Migration. *Cell*, 148(1-2):175–188, jan 2012.

[45] J Howard and RL Clark. Mechanics of Motor Proteins and the Cytoskeleton. *Applied Mechanics Reviews*, 2002. ISSN 00036900. doi: 10.1115/1.1451234.

[46] P Hozák, A M Sasseville, Y Raymond, and P R Cook. Lamin proteins form an internal nucleoskeleton as well as a peripheral lamina in human cells. *Journal of cell science*, 108 (Pt 2:635–644, 1995. ISSN 0021-9533.

[47] Chuan-Hsiang Huang, Ming Tang, Changji Shi, Pablo A Iglesias, and Peter N Devreotes. An excitable signal integrator couples to an idling cytoskeletal oscillator to drive cell migration. *Nature Cell Biology*, 15(11):1307–1316, oct 2013.

[48] Christopher J. Hutchison. Lamins: building blocks or regulators of gene expression? *Nature Reviews Molecular Cell Biology*, 3(11):848–858, 2002. ISSN 1471-0072. doi: 10.1038/nrm950. URL http://www.nature.com/doifinder/10.1038/nrm950.

[49] Timon Idema, T Idema, J O Dubuis, Julien O Dubuis, L Kang, Louis Kang, M Lisa Manning, M L Manning, P C Nelson, Philip C Nelson, Tom C Lubensky, and Andrea J Liu. The syncytial Drosophila embryo as a mechanically excitable medium. *PLoS ONE*, 2013.

[50] P. Jorgensen, N. P. Edgington, B. L. Schneider, I. Rupes, M. Tyers, and B. Futcher. The Size of the Nucleus Increases as Yeast Cells Grow. *Molecular Biology of the Cell*, 2007. ISSN 1059-1524. doi: 10.1091/mbc.E06-10-0973.

[51] M Kapustina, T C Elston, and K Jacobson. Compression and dilation of the membrane-cortex layer generates rapid changes in cell shape. *Journal Of Cell Biology*, 200(1): 95–108, jan 2013.

[52] Cheryl A. Kerfeld, Clement Aussignargues, Jan Zarzycki, Fei Cai, and Markus Sutter. Bacterial microcompartments. *Nature Reviews Microbiology*, 2018. ISSN 17401534. doi: 10.1038/nrmicro.2018.10.

[53] D.-H. Kim, B. Li, F. Si, J. M. Phillip, D. Wirtz, and S. X. Sun. Volume regulation and shape bifurcation in the cell nucleus. *Journal of Cell Science*, 2016. ISSN 0021-9533. doi: 10.1242/jcs.185173.

[54] A. Kolmogorov, I. Petrovskii, and N. Piscunov. A study of the equation of diffusion with increase in the quantity of matter, and its application to a biological problem. *Byul. Moskovskogo Gos. Univ.*, 1(6):1–25, 1937. URL http://books.google.com/books?id=ikN59GkYJKIC&lpg=PP1&dq=A.N.%20Kolmogorov%3A%20Selected%20Works&client=firefox-a&pg=PA242#v=onepage&q=&f=false.

[55] Shigeru Kondo and Takashi Miura. Reaction-Diffusion Model as a Framework for Understanding Biological Pattern Formation. *Science*, 329(5999):1616 LP – 1620, sep 2010. URL http://science.sciencemag.org/content/329/5999/1616.abstract.

[56] Po Ling Kuo, Hyungsuk Lee, Mark Anthony Bray, Nicholas A. Geisse, Yen Tsung Huang, William J. Adams, Sean P. Sheehy, and Kevin K. Parker. Myocyte shape regulates lateral registry of sarcomeres and contractility. *American Journal of Pathology*, 181(6):2030–2037, 2012. ISSN 00029440. doi: 10.1016/j.ajpath.2012.08.045. URL http://dx.doi.org/10.1016/j.ajpath.2012.08.045.

[57] Yuri A Kuznetsov. *Elements of applied bifurcation theory*, volume 112. Springer Science & Business Media, 2013.

[58] C. T. Lee, M. F. Hoopes, J. Diehl, W. Gilliland, G. Huxel, E. V. Leaver, K. Mccann, J. Umbanhowar, and A. Mogilner. Non-local concepts and models in biology. *Journal of Theoretical Biology*, 210(2):201–219, 2001. ISSN 00225193. doi: 10.1006/jtbi.2000.2287.

[59] J Lee, A Ishihara, J A Theriot, and K Jacobson. Principles of locomotion for simple-shaped cells. *Nature*, 362(6416):167–171, 1993.

[60] Natascha Leijnse, Lene B Oddershede, and Poul M Bendix. An updated look at actin dynamics in filopodia. *Cytoskeleton (Hoboken, N.J.)*, 72(2):71–79, feb 2015.

[61] F Y Lim, K-H Chiam, and L Mahadevan. The size, shape, and dynamics of cellular blebs. *Epl*, 100(2):28004, oct 2012.

[62] Jian Liu, Yidi Sun, George F Oster, and David G Drubin. Mechanochemical crosstalk during endocytic vesicle formation. *Current Opinion In Cell Biology*, 22(1):36–43, feb 2010.

[63] Jeremy S Logue, Alexander X Cartagena-Rivera, Michelle A Baird, Michael W Davidson, Richard S Chadwick, and Clare M Waterman. Erk regulation of actin capping and bundling by Eps8 promotes cortex tension and leader bleb-based migration. *eLife*, 4, jul 2015.

[64] Weiwei Luo, Cheng han Yu, Zi Zhao Lieu, Jun Allard, Alex Mogilner, Michael P. Sheetz, and Alexander D. Bershadsky. Analysis of the local organization and dynamics of cellular actin networks. *Journal of Cell Biology*, 2013. ISSN 00219525. doi: 10.1083/jcb.201210123.

[65] Emad Moeendarbary, Léo Valon, Marco Fritzsche, Andrew R Harris, Dale A Moulding, Adrian J Thrasher, Eleanor Stride, L Mahadevan, and Guillaume T Charras. The cytoplasm of living cells behaves as a poroelastic material. *Nature materials*, 12(3): 253, 2013.

[66] Alexander Mogilner and Leah Edelstein-Keshet. A non-local model for a swarm. pages 534–570, 1999.

[67] Yoichiro Mori, Alexandra Jilkine, and Leah Edelstein-Keshet. Wave-pinning and cell polarity from a bistable reaction-diffusion system. *Biophysical Journal*, 94(9):3684–3697, may 2008.

[68] Yoichiro Mori, Alexandra Jilkine, and Leah Edelstein-Keshet. Wave-pinning and cell polarity from a bistable reaction-diffusion system. *Biophysical Journal*, 94(9):3684–3697, may 2008.

[69] Greg Morrison and D. Thirumalai. Semiflexible chains in confined spaces. *Physical Review E - Statistical, Nonlinear, and Soft Matter Physics*, 2009. ISSN 15393755. doi: 10.1103/PhysRevE.79.011924.

[70] Antoine Muchir, Baziel G Van Engelen, Martin Lammens, John M Mislow, Elizabeth McNally, Ketty Schwartz, and Gisèle Bonne. Nuclear envelope alterations in fibroblasts from lgmd1b patients carrying nonsense y259x heterozygous or homozygous mutation in lamin a/c gene. *Experimental cell research*, 291(2):352–362, 2003.

[71] J D Murray. *Mathematical Biology : I . An Introduction , Third Edition*, volume 1. 2002. ISBN 0387952233. doi: 10.1086/421587. URL http://books.google.com/books?hl=en{&}lr={&}id=4WbpP90Gk1YC{&}oi=fnd{&}pg=PR7{&}dq=Mathematical+Biology+:+I+.+An+Introduction{&}ots=7pV6xaDATm{&}sig=Puq3bu3Ob8z657v1tgna4E51b-Y.

[72] James D Murray. *Mathematical Biology*. Springer Berlin Heidelberg, Berlin, Heidelberg, 1989.

[73] J. Nagumo, S. Arimoto, and S. Yoshizawa. An Active Pulse Transmission Line Simulating Nerve Axon*. *Proceedings of the IRE*, 50(10):2061–2070, 1962. ISSN 00968390. doi: 10.1109/JRPROC.1962.288235.

[74] Frank R. Neumann and Paul Nurse. Nuclear size control in fission yeast. *Journal of Cell Biology*, 2007. ISSN 00219525. doi: 10.1083/jcb.200708054.

[75] E C Olson. Onset of electrical excitability during a period of circus plasma membrane movements in differentiating Xenopus neurons. *Journal of Neuroscience*, 16(16):5117–5129, aug 1996.

[76] Ewa K Paluch and Erez Raz. The role and regulation of blebs in cell migration. *Current Opinion In Cell Biology*, 25(5):582–590, oct 2013.

[77] Matthew J Paszek, Christopher C DuFort, Olivier Rossier, Russell Bainer, Janna K Mouw, Kamil Godula, Jason E Hudak, Jonathon N Lakins, Amanda C Wijekoon, Luke Cassereau, Matthew G Rubashkin, Mark J Magbanua, Kurt S Thorn, Michael W Davidson, Hope S Rugo, John W Park, Daniel A Hammer, Grégory Giannone, Carolyn R Bertozzi, and Valerie M Weaver. The cancer glycocalyx mechanically primes integrin-mediated growth and survival. *Nature*, 511(7509):319–325, apr 2015.

[78] Barak Peleg, Andrea Disanza, Giorgio Scita, and Nir Gov. Propagating Cell-Membrane Waves Driven by Curved Activators of Actin Polymerization. *PLoS ONE*, 6(4):e18635, apr 2011.

[79] B. Peng, V. Gaspar, and K. Showalter. False Bifurcations in Chemical Systems: Canards. *Philosophical Transactions of the Royal Society A: Mathematical, Physical and Engineering Sciences*, 337(1646):275–289, 1991. ISSN 1364-503X. doi: 10.1098/rsta.1991.0123. URL http://rsta.royalsocietypublishing.org/cgi/doi/10.1098/rsta.1991.0123.

[80] Julia Peukes and Timo Betz. Direct Measurement of the Cortical Tension during the Growth of Membrane Blebs. *Biophysj*, 107(8):1810–1820, oct 2014.

[81] Shuyan Qi, Michelle Krogsgaard, Mark M Davis, and Arup K Chakraborty. Molecular flexibility can influence the stimulatory ability of receptor-ligand interactions at cell-cell junctions. *Proceedings Of The National Academy Of Sciences Of The United States Of America*, 103(12):4416–4421, mar 2006.

[82] Andreea E. Radulescu and Don W. Cleveland. NuMA after 30 years: The matrix revisited, 2010. ISSN 09628924.

[83] Padmini Rangamani, Ayelet Benjamini, Ashutosh Agrawal, Berend Smit, David J Steigmann, and George Oster. Small scale membrane mechanics. *Biomechanics and Modeling in Mechanobiology*, oct 2013.

[84] Gillian L Ryan, Heather M Petroccia, N Watanabe, and Dimitrios Vavylonis. Excitable Actin Dynamics in Lamellipodial Protrusion and Retraction. *Biophysical Journal*, 102 (7):1493–1502, apr 2012.

[85] Gillian L Ryan, Naoki WATANABE, and Dimitrios Vavylonis. A review of models of fluctuating protrusion and retraction patterns at the leading edge of motile cells. *Cytoskeleton (Hoboken, N.J.)*, 69(4):195–206, feb 2012.

[86] G Salbreux, J Prost, and J F Joanny. Hydrodynamics of Cellular Cortical Flows and the Formation of Contractile Rings. *Physical Review Letters*, 103(5):58102, jul 2009.

[87] Jakub Sedzinski, Maté Biro, Annelie Oswald, Jean-Yves Tinevez, Guillaume Salbreux, and Ewa Paluch. Polar actomyosin contractility destabilizes the position of the cytokinetic furrow. *Nature*, 476(7361):462–466, aug 2011.

[88] Mark R. Smyda and Stephen C. Harvey. The entropic cost of polymer confinement. *Journal of Physical Chemistry B*, 2012. ISSN 15205207. doi: 10.1021/jp302807r.

[89] William Stillwell. Introduction to Biological Membranes. In *An Introduction to Biological Membranes*. 2013. ISBN 9780444521538. doi: 10.1016/B978-0-444-52153-8.00001-5.

[90] W Strychalski and R D Guy. A computational model of bleb formation. *Mathematical Medicine and Biology*, 30(2):115–130, jun 2013.

[91] W Strychalski and R D Guy. Intracellular Pressure Dynamics in Blebbing Cells . 2015.

[92] Wanda Strychalski and Robert D Guy. Intracellular Pressure Dynamics in Blebbing Cells. *Biophysj*, 110(5):1168–1179, March 2016.

[93] Wanda Strychalski, Calina A Copos, Owen L Lewis, and Robert D Guy. A poroelastic immersed boundary method with applications to cell biology. *Journal of Computational Physics*, 282(C):77–97, feb 2015.

[94] Pekka Taimen, Katrin Pfleghaar, Takeshi Shimi, Dorothee Möller, Kfir Ben-Harush, Michael R Erdos, Stephen A Adam, Harald Herrmann, Ohad Medalia, Francis S Collins, et al. A progeria mutation reveals functions for lamin a in nuclear assembly, architecture, and chromosome organization. *Proceedings of the National Academy of Sciences*, 106(49):20788–20793, 2009.

[95] Alessandro Taloni, Elena Kardash, Oguz Umut Salman, Lev Truskinovsky, Stefano Zapperi, and Caterina A. M. La Porta. Volume changes during active shape fluctuations in cells. *Phys. Rev. Lett.*, 114:208101, May 2015. doi: 10.1103/PhysRevLett.114.208101. URL `https://link.aps.org/doi/10.1103/PhysRevLett.114.208101`.

[96] Jonathan N Thon, Hannah Macleod, Antonija Jurak Begonja, Jie Zhu, Kun-Chun Lee, Alex Mogilner, John H Hartwig, and Joseph E Italiano. Microtubule and cortical forces determine platelet size during vascular platelet production. *Nature Communications*, 3:852–859, may 2012.

[97] Jean-Yves Tinevez, Ulrike Schulze, Guillaume Salbreux, Julia Roensch, Jean-François Joanny, and Ewa Paluch. Role of cortical tension in bleb growth. *Proceedings Of The National Academy Of Sciences Of The United States Of America*, 106(44):18581–18586, nov 2009.

[98] A. M. Turing. The chemical basis of morphogenesis. *Philosophical Transactions of the Royal Society of London*, 52(1-2):153–197, 1952. ISSN 00928240. doi: 10.1007/BF02459572.

[99] John J. Tyson and James P. Keener. Singular perturbation theory of traveling waves in excitable media (a review). *Physica D: Nonlinear Phenomena*, 32(3):327–361, 1988. ISSN 01672789. doi: 10.1016/0167-2789(88)90062-0.

[100] David Wake, Iswar Hariharan, and Rebecca Heald. *Size control in biology: from organelles to organisms*. Cold Spring Harbor Laboratory Press, 2015.

[101] Richard J. Wheeler and Anthony A. Hyman. Controlling compartmentalization by non-membrane-bound organelles, 2018. ISSN 14712970.

[102] H. R. Wilson and J. D. Cowan. A mathematical theory of the functional dynamics of cortical and thalamic nervous tissue. *Biological Cybernetics*, 13(2):55–80, 1973. ISSN 0340-1200. doi: 10.1007/BF00288786. URL `http://www.springerlink.com/content/m28540k4769650u4/abstract/`.

[103] Hugh R. Wilson and Jack D. Cowan. Excitatory and Inhibitory Interactions in Localized Populations of Model Neurons. *Biophysical Journal*, 12(1):1–24, 1972. ISSN 00063495. doi: 10.1016/S0006-3495(72)86068-5. URL `http://dx.doi.org/10.1016/S0006-3495(72)86068-5`.

[104] Steven Wise, Junseok Kim, and John Lowengrub. Solving the regularized, strongly anisotropic cahnhilliard equation by an adaptive nonlinear multigrid method. *Journal of Computational Physics*, 226(1):414 – 446, 2007. ISSN 0021-9991. doi: http://dx.doi.org/10.1016/j.jcp.2007.04.020. URL `http://www.sciencedirect.com/science/article/pii/S0021999107001647`.

[105] R Wollman and T Meyer. Coordinated oscillations in cortical actin and Ca2+ correlate with cycles of vesicle secretion. *Nature Cell Biology*, 14(12):1261–1269, nov 2012.

[106] T E Woolley, E A Gaffney, S L Waters, J M Oliver, R E Baker, and A Goriely. Three mechanical models for blebbing and multi-blebbing. *IMA Journal of Applied Mathematics*, 79(4):636–660, jul 2014.

[107] Thomas E Woolley, Eamonn A Gaffney, James M Oliver, Ruth E Baker, Sarah L Waters, and Alain Goriely. Cellular blebs: pressure-driven, axisymmetric, membrane protrusions. *Biomechanics and Modeling in Mechanobiology*, 13(2):463–476, jul 2013.

[108] Thomas E Woolley, Eamonn A Gaffney, and Alain Goriely. Membrane shrinkage and cortex remodelling are predicted to work in harmony to retract blebs. *Royal Society Open Science*, 2(7):150115–150184, jul 2015.

[109] Yuan Xiong, Chuan-Hsiang Huang, Pablo A Iglesias, and Peter N Devreotes. Cells navigate with a local-excitation, global-inhibition-biased excitable network. *Proceedings Of The National Academy Of Sciences Of The United States Of America*, 107(40): 17079–17086, oct 2010.

[110] Ai Kia Yip, Keng-Hwee Chiam, and Paul Matsudaira. Traction stress analysis and modeling reveal that amoeboid migration in confined spaces is accompanied by expansive forces and requires the structural integrity of the membrane-cortex interactions. *Integr. Biol.*, 7:1196–1211, 2015. doi: 10.1039/C4IB00245H. URL `http://dx.doi.org/10.1039/C4IB00245H`.

[111] Jennifer Young and Sorin Mitran. A numerical model of cellular blebbing: A volume-conserving, fluid{\textendash}structure interaction model of the entire cell. *Journal of Biomechanics*, 43(2):210–220, jan 2010.

[112] Jianshe Yu and Shanshan Chen. Dynamics of a strongly nonlocal reaction diffusion population model Dynamics of a strongly nonlocal reaction diffusion. 2004. doi: 10.1088/0951-7715/17/1/018.

[113] Cheng Zhu. Mechanochemitry: A Molecular Biomechanics View of Mechanosensing. *Annals of Biomedical Engineering*, 42(2):388–404, sep 2013.

[114] Laura Zonia and Teun Munnik. Life under pressure: hydrostatic pressure in cell growth and function. *Trends in Plant Science*, 2007. ISSN 13601385. doi: 10.1016/j.tplants.2007.01.006.

Appendix A

Cell surface mechanochemistry and the determinants of bleb formation, healing and travel velocity

A.1 Summary of experimental predictions

The model makes several testable predictions. For convenience, we tabulate these predictions here. Note that these predictions presume that the cell is exhibiting blebs before the perturbation.

Table A.1: Model predictions for experimental perturbations.

Experimental perturbation	Parameter	Prediction
Increasing hydrostatic pressure	$P \uparrow$	Larger blebs
Increasing molecular size of adhesion molecules	$D \uparrow$	Abolish blebbing
Decreasing molecular size of adhesion molecules	$D \downarrow$	Slower bleb healing
Increasing myosin contractility	$M \uparrow$	Abolish blebbing
Decreasing myosin contractility	$M \downarrow$	Slower bleb healing
Increasing membrane tension	$\gamma_M \uparrow$	Faster bleb travel
Increasing abundance of adhesions	$k_{\text{on}} \uparrow$	Slower bleb travel

A.2 Details of geometry of cortical and cytoplasmic actin

In 3D, the cell surface and cortex are curved, discontinuous two-dimensional manifolds and the cytoplasm is a 3D field. In full generality, the cortex and cytoplasmic actin network have a density at each point in space. We assume that actin-myosin contractility is isotropic and generates local stress proportional to the local density of cortical actin c. This stress therefore has two components: a tangential component due to connection with nearby cortex

$$\sigma_t = \sigma_m w_c c \nabla y_C, \tag{A.2.1}$$

and a normal stress due to connection with the cytoplasmic actin network

$$\sigma_n = \sigma_m c y_C. \tag{A.2.2}$$

We find that the normal contractile force is necessary for asymmetric bleb healing, as occurs during bleb travel. This necessity can be understood from Figure A.1: In the absence of cytoplasmic actin, the tangential stress pulls the membrane tangentially, but there is no force driving the cortex into the place of the cell.

Our goal is to understand in 3D. To this end, we find it informative to study simplified 2D systems and 1D systems as an analytical tool. The 2D model is equivalent to either the geometries shown in Figure A.1C or D. The 1D model, which we refer to as the ODE model in the Chapter 2, corresponds to the geometry shown in Figure A.1E.

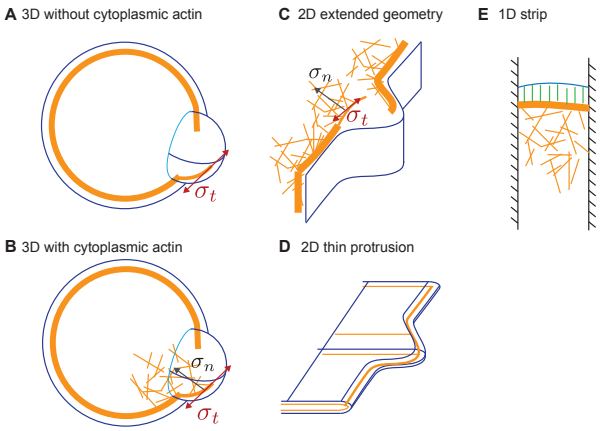

Figure A.1: Approximations of cortex and cytoplasmic actin geometry in 3D. (A-B) Bleb geometry in 3D including only tangential cortical contractility (A), and both tangential and normal contractility (B). (C-D) Representation of 2D model. (E) Hypothetical 1D "non-spatial" model corresponding to ODE system used in this project.

Table A.2: Estimates of parameters used in nondimensionalization.

Model parameter	Estimated value	Source
r	$0.1/s$	[34]
k_{on}	$100/\,\mu\text{m}^2 \cdot \text{s}$	[17]
k_{off}	$1/s$	[34]
κ	$10\,\text{pN}/\mu m$	[17]
σ_m	$0.1\text{Pa}/\,\mu\text{m}^2$	[17]
$\hat{\Pi}$	$100\text{Pa}/\,\mu\text{m}$	[17]
y_M^0	$3\,\mu\text{m}$	[19]
γ_M	$100\,\text{pN}/\,\mu\text{m}$	[80]

A.3 Parameter estimation

Using these estimates, the correspondence between dimensional and nondimensional parameters are given by

$$x = \chi \cdot 0.2\,\mu\text{m} \tag{A.3.1}$$

$$t = \tau \cdot 10s \tag{A.3.2}$$

$$a = A \cdot 100/\mu m^2 \tag{A.3.3}$$

$$y_M = Y_M \cdot 3\,\mu\text{m} \tag{A.3.4}$$

$$y_C = Y_C \cdot 3\,\mu\text{m}. \tag{A.3.5}$$

Note that model parameters not included in Table A.2 do not impact the nondimensionalization.

To perform the parameter-space exploration in Figure 2.5, we used ranges shown in Table A.3.

Table A.3: Dimensional parameters with ranges explored in simulation.

Parameter	Range explored for velocity plot
ω	$0.0004 - 0.0006$ [A.U.] $\cdot\,\text{s}^{-1}$
r	$0.01 - 0.25\ \text{s}^{-1}$
k_{on}	$95 - 140\,\mu\text{m}^{-2}\text{s}^{-1}$
k_{off}	$0.5 - 1.05\ \text{s}^{-1}$
δ	$0.14 - 0.17\,\mu\text{m}$
κ	$9 - 13\ \text{pN}/\,\mu\text{m}$
f_0	$5 - 20$ pN
σ_m	$550 - 725$ Pa/ [A.U.]
$\hat{\Pi}$	$65 - 105\ \text{Pa}/\,\mu\text{m}$
γ_M	$10 - 400\ \text{pN}/\,\mu\text{m}$

A.4 Model variants

A.4.1 Bending

The inclusion of higher-order derivatives in the mechanical energy transform the system into a higher-order boundary value problem. For example, the bending energy term transforms the membrane shape equation to a fourth-order equation. We simulate the base model with the addition of bending terms $B > 0$, where the nondimensional bending modulus is $B \equiv \beta/\gamma x_c^3$. Results are shown in Figure A.2. We find that the excitable parameter regime and traveling parameter regimes are unchanged. For $B = 100$, the velocity of travel is increased by approximately two-fold and healing is delayed compared to no bending.

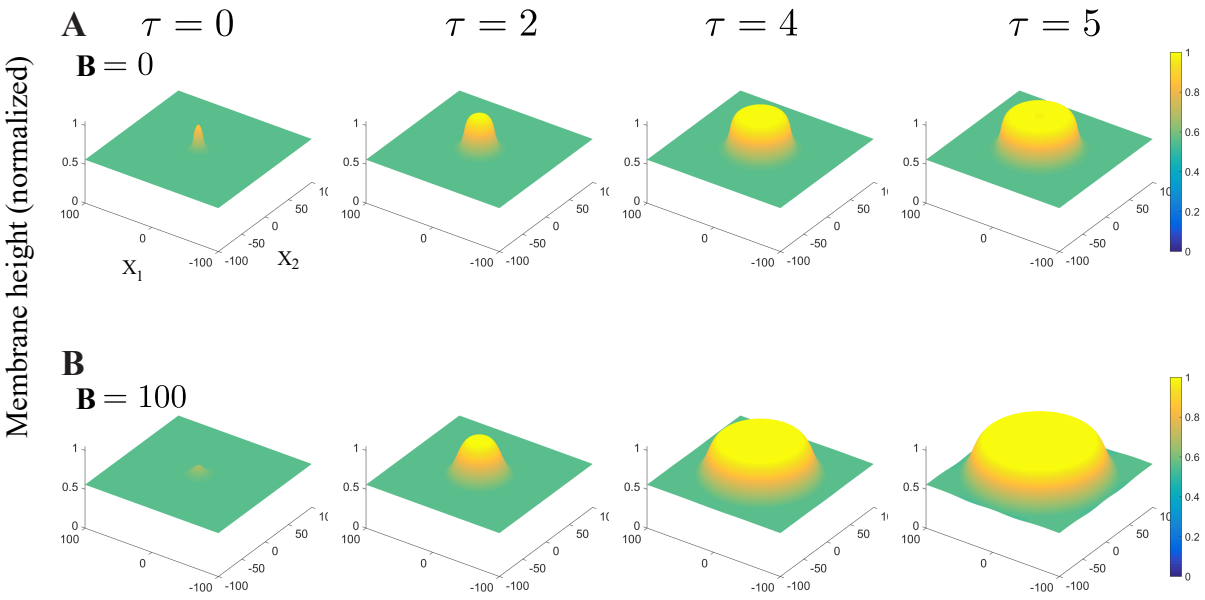

Figure A.2: Influence of membrane bending rigidity. (A) Traveling bleb on a uniform surface with no bending energy $B = 0$. (B) Traveling bleb with large bending rigidity $B = 100$. The bleb velocity is increased by approximately two-fold and healing is delayed (but eventually occurs, not shown).

A.4.2 Part-local, part-global pressure models

In the Main Text, we present models in which pressure is either purely global (one quantity is shared among the entire domain) or purely local (a local increase in y_M leads to a local drop in pressure, and no where else). However, recent evidence from computational models [91] suggests that in a poroelastic cytoplasm, local membrane extension may lead to a large local pressure drop and a smaller global pressure drop. To address this possibility, we simulate model variants in which the pressure drop is part local and part global.

- Local-global additive:

$$\Pi(x_1, x_2) = \hat{\Pi}\left(\left(1 - \frac{y_M(x_1, x_2)}{y_M^0}\right) + \epsilon_p \iint \left(1 - \frac{y_M(\tilde{x}_1, \tilde{x}_2)}{y_M^0}\right) d\tilde{x}_1 d\tilde{x}_2\right) \quad \text{(A.4.1)}$$

- Local-global multiplicative pressure:

$$\Pi(x_1, x_2) = \hat{\Pi} \cdot \left(1 - \frac{y_M(x_1, x_2)}{y_M^0}\right) \cdot \iint \left(1 - \frac{y_M(\tilde{x}_1, \tilde{x}_2)}{y_M^0}\right) d\tilde{x}_1 d\tilde{x}_2 \quad \text{(A.4.2)}$$

Results are shown in Figure A.3. As expected, when the global component of pressure drop is small, simulation results are similar to purely-local pressure, with blebs expanding outward as an expanding annulus. As intermediate global components, the global pressure drop is enough to collapse the bleb as its area increases. No symmetry breaking is observed.

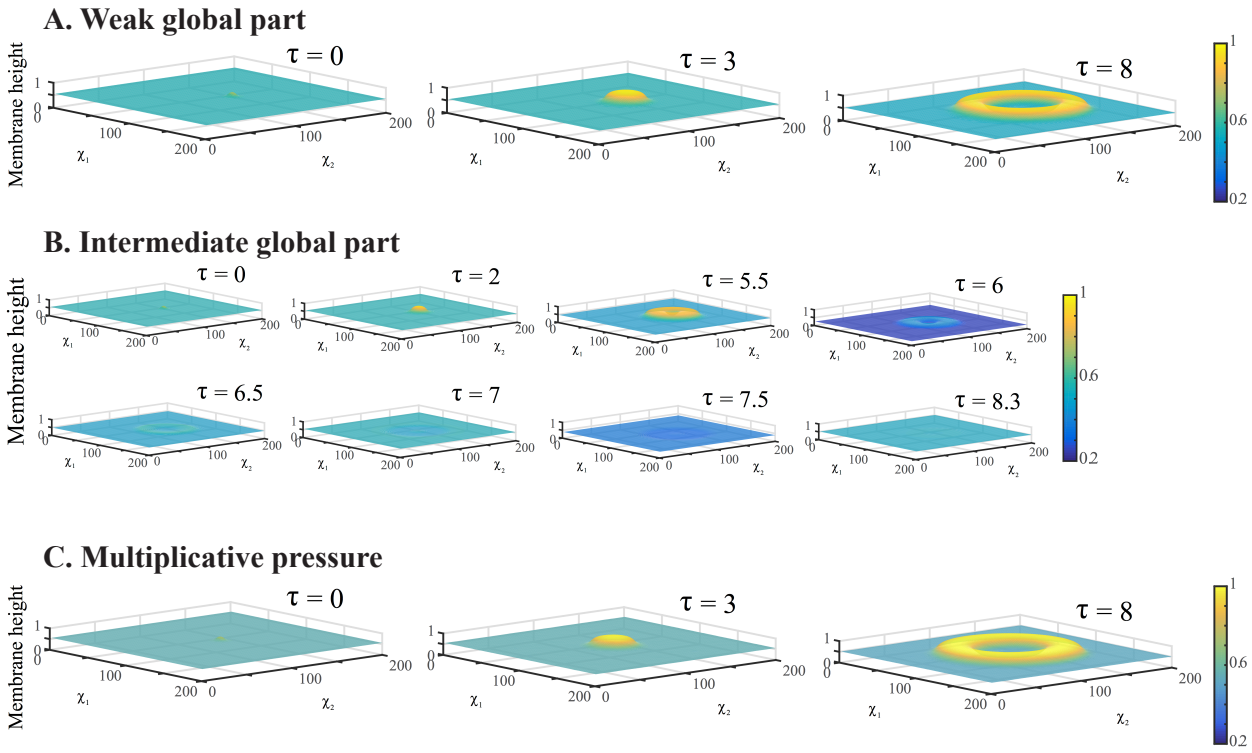

Figure A.3: Simulations assuming that local membrane protrusion leads to both local and global pressure drops. (A) Additive pressure Eq. A.4.1 with weak global part, $\epsilon_p = 0.1$. (B) Additive pressure with intermediate global part, $\epsilon_p = 0.18$. (C) Multiplicative pressure.

A.5 Details of numerical method

A.5.1 Base model

The base model, Eqs. 10-13, comprise a two-dimensional boundary value problem of elliptic type at each instant in time, coupled to two first-order (in time) partial differential equations. To solve the base model, we discretize space into a uniform grid of width $\Delta\chi = 0.1$ and time step size $\Delta\tau = 0.01$. We use a standard five-point stencil finite difference method in space and forward-Euler in time.

A.5.2 Non-uniform tension

The inclusion of non-uniform tension changes the boundary value problem to a non-uniform elliptic equation. The equations takes the form

$$P = f(\chi_1, \chi_2) Y_M(\chi_1, \chi_2) - \nabla \cdot (\Gamma(\chi_1, \chi_2) \nabla Y_M(\chi_1, \chi_2)) \tag{A.5.1}$$

where f and Γ are spatially varying. We use a uniform grid in space and set $\Delta\chi = 0.1$. The functions f, Y_M and Γ all live at cell edges ($f|_{i,j} = f(i\Delta\chi,\ j\Delta\chi),\quad i = 1, 2, ..., 2000$) and we impose periodic boundary conditions. The parameter functions f and Γ must be interpolated to the edges, which we do by uniform averaging. The resulting discretization stencil is given by

$$\begin{aligned} P = &\left(f|_{i,j} + \frac{1}{2\Delta x^2} \left(\Gamma|_{i+1,j} + \Gamma|_{i-1,j} + \Gamma|_{i,j+1} + \Gamma|_{i,j-1} + 4\Gamma|_{i,j}\right)\right) \mathbf{Y_M}|_{\mathbf{i,j}} \\ &- \frac{1}{2\Delta x^2} \left((\Gamma|_{i+1,j} + \Gamma|_{i,j})\mathbf{Y_M}|_{\mathbf{i+1,j}} + (\mathbf{\Gamma}|_{\mathbf{i,j}} + \mathbf{\Gamma}|_{\mathbf{i,j-1}})\mathbf{Y_M}|_{\mathbf{i-1,j}}\right) \\ &- \frac{1}{2\Delta x^2}((\Gamma|_{i,j} + \Gamma|_{i,j+1})\mathbf{Y_M}|_{\mathbf{i,j+1}} + (\mathbf{\Gamma}|_{\mathbf{i,j}} + \mathbf{\Gamma}|_{\mathbf{i,j-1}})\mathbf{Y_M}|_{\mathbf{i,j-1}}) \end{aligned}$$

Since this equation remains linear, it can be written into a sparse matrix and solved as a linear system.

A.5.3 Higher-order models including bending forces

Adding higher order terms, including bending forces, transforms the boundary value problem into a higher-order boundary value problem. The bending term, in particular, introduces a fourth-order bilaplacian operator. This significantly increases the computational cost of solving the equations, therefore we use a more sophisticated solver described here. We solve

the following equations:

$$\frac{\partial C}{\partial \tau} = \Omega A - C \tag{A.5.2}$$

$$\epsilon \frac{\partial A}{\partial \tau} = \frac{C}{1+C} \exp\left(-\left(\frac{1}{D}\frac{MC}{A+MC}Y_M\right)\right) - A \exp\left(\frac{1}{F_0}\frac{MC}{A+MC}Y_M\right) \tag{A.5.3}$$

$$P = hY_m - \nabla \cdot (\Gamma \nabla Y_M) + B\nabla^4 Y_M \tag{A.5.4}$$

$$h = \frac{AMC}{A+MC} + P, \tag{A.5.5}$$

where $\Omega = 57, \epsilon = 0.1, D = 0.15, F_0 = 1, M = 0.007$ and $P = 0.1$. In non-uniform tension models, $B = 0$ and the non-uniform tension term $\Gamma = 1 + \theta C$ where $\theta = 0.1$ or $\theta = 0.2$. For bending models, $\Gamma = 1$ and $B \in \{10^{-2}, 10^{-1}, 1, 10^1, 10^2\}$.

All variables satisfy periodic conditions at all boundaries. The initial condition for Y_M and C is their steady state value $Y_M^{ss} = 0.5582$ and $C^{ss} = 15.8236$. A is also set to steady state $A^{ss} = 0.2776$ except where the bleb is triggered on a 5χ x 5χ patch where $A = 0$.

The system is solved in a square computational domain $[-200, 200]^2$. The domain is initialized to a 64×64 mesh with a maximum of 5 refinement levels. At the finest level, grid length is $400/(64 \times 2^5) \approx 0.2$. The time step is 10^{-2}.

We use the implicit second order Crank-Nicholson scheme for time discretization in eqs. (A.5.2) and (A.5.3). Spatial derivatives are discretized using central difference approximations. eq. (A.5.4) is reformulated as a system of two second order equations. Block structured Cartesian refinement is used to efficiently resolve the multiple spatial scales. In particular, the mesh is refined in regions with large spatial gradients of Y_M (typically around the bleb). The equations at implicit time level are solved by the adaptive nonlinear multigrid method developed in [104].

Appendix B

Nuclear shape

B.1 Nondimensionalization

Characteristic scales

$$a^c = b_{\text{tot}}/\mathcal{L}_0$$

$$b^c = b_{\text{tot}}/\mathcal{L}_0$$

$$a^c_{\text{nuc}} = \frac{k^{0b}_{\text{off}}}{k^b_{\text{on}}} \frac{b_{\text{tot}}}{\mathcal{L}_0} \frac{\mathcal{L}_0^2}{4\pi}$$

$$b^c_{\text{nuc}} = \frac{k^{0b}_{\text{off}}}{k^b_{\text{on}}} \frac{b_{\text{tot}}}{\mathcal{L}_0} \frac{\mathcal{L}_0^2}{4\pi}$$

$$t^c = 1/k^{0b}_{\text{off}}$$

$$s^c = \mathcal{L}_0/(2\sqrt{\pi})$$

$$\mathcal{E}^c = \mathcal{G}_b(b^c)\mathcal{L}_0/(2\sqrt{\pi})$$

Let

$$A = a/a^c$$
$$B = b/b^c$$
$$A_{\text{nuc}} = a_{\text{nuc}}/a^c_{\text{nuc}}$$
$$B_{\text{nuc}} = b_{\text{nuc}}/b^c_{\text{nuc}}$$
$$\tau = t/t^c$$
$$S = s/s^c$$
$$\vec{\chi} = \vec{x}/s^c$$
$$E = \mathcal{E}/\mathcal{E}^c$$

Then

$$\begin{aligned}
\frac{\partial A}{\partial \tau} &= \frac{\mathcal{L}_0}{b_{\text{tot}} k^{0b}_{\text{off}}} \left(\frac{k^a_{\text{on}}}{\mathcal{A}(t)} A_{\text{nuc}} \frac{k^{0b}_{\text{off}}}{k^b_{\text{on}}} \frac{b_{\text{tot}}}{\mathcal{L}_0} \frac{\mathcal{L}_0^2}{4\pi} - k^a_{\text{off}}(s,b) A \frac{b_{\text{tot}}}{\mathcal{L}_0} \right) = \frac{k^a_{\text{on}}}{k^b_{\text{on}}} \frac{\mathcal{L}_0^2}{4\pi \mathcal{A}(t)} A_{\text{nuc}} - \frac{k^a_{\text{off}}(s,b)}{k^{0b}_{\text{off}}} A \\
\frac{\partial B}{\partial \tau} &= \frac{\mathcal{L}_0}{b_{\text{tot}} k^{0b}_{\text{off}}} \left(\frac{k^b_{\text{on}}}{\mathcal{A}(t)} B_{nuc} \frac{k^{0b}_{\text{off}}}{k^b_{\text{on}}} \frac{b_{\text{tot}}}{\mathcal{L}_0} \frac{\mathcal{L}_0^2}{4\pi} - k^b_{\text{off}}(s,a) B \frac{b_{\text{tot}}}{\mathcal{L}_0} \right) = \frac{\mathcal{L}_0^2}{4\pi \mathcal{A}(t)} B_{\text{nuc}} - \frac{k^b_{\text{off}}(s,b)}{k^{0b}_{\text{off}}} B \\
&\rightarrow \quad \text{let } \kappa_{\text{on}} = \frac{k^a_{\text{on}}}{k^b_{\text{on}}}, \lambda(\tau) = \frac{4\pi \mathcal{A}(t)}{\mathcal{L}_0^2}, \phi_A(S,B) = \frac{\Phi_a(S,B)}{k^{0b}_{\text{off}}}, \phi_B(S,A) = \frac{\Phi_b(S,A)}{k^{0b}_{\text{off}}}, \kappa_{\text{off}} = \frac{k^{0a}_{\text{off}}}{k^{0b}_{\text{off}}} \\
\Rightarrow \frac{\partial A}{\partial \tau} &= \kappa_{\text{on}} \frac{1}{\lambda(\tau)} A_{\text{nuc}} - (\kappa_{\text{off}} + \phi_A(S,B)) A, \\
\frac{\partial B}{\partial \tau} &= \frac{1}{\lambda(\tau)} B_{\text{nuc}} - (1 + \phi_B(S,A)) B
\end{aligned}$$

And

$$
\begin{aligned}
E &= \frac{\mathcal{E}_{\text{stretch}} + \mathcal{E}_{\text{pressure}} + \mathcal{E}_{\text{bending}} + \mathcal{E}_{\text{cytoskeleton}} + k_B\mathcal{T}\xi}{\mathcal{G}_b(b^c)\mathcal{L}_0/(2\sqrt{\pi})} \\
E_{\text{stretch}} &= \frac{\int_0^{\mathcal{L}_0} \frac{1}{2}(\mathcal{G}_a(a(s)) + \mathcal{G}_b(b(s)))\left(\left|\left|\frac{\partial\vec{x}}{\partial s}\right|\right| - 1\right)^2 ds}{\mathcal{G}_b(b^c)\mathcal{L}_0/(2\sqrt{\pi})} \\
&= \frac{\int_0^{2\sqrt{\pi}} \frac{1}{2}(\mathcal{G}_a(A(S)a^c) + \mathcal{G}_b(B(S)b^c))\left(\left|\left|\frac{\partial\vec{\chi}}{\partial S}\right|\right| - 1\right)^2 \frac{\mathcal{L}_0}{2\sqrt{\pi}} dS}{\mathcal{G}_b(b^c)\mathcal{L}_0/(2\sqrt{\pi})} \\
&\text{let } G_A(A(S)) = \frac{\mathcal{G}_a(A(S)a^c)}{\mathcal{G}_b(b^c)}, G_B(B(S)) = \frac{\mathcal{G}_b(B(S)b^c)}{\mathcal{G}_b(b^c)} \\
\Rightarrow E_{\text{stretch}} &= \int_0^{2\sqrt{\pi}} \frac{1}{2}(G_A(A(S)) + G_B(B(S)))\left(\left|\left|\frac{\partial\vec{\chi}}{\partial S}\right|\right| - 1\right)^2 dS \\
E_{\text{pressure}} &= \frac{\mathcal{P}\left(\frac{\lambda(\tau)}{\lambda_0} - 1\right)^2}{\mathcal{G}_b(b^c))\mathcal{L}_0/(2\sqrt{\pi})} = \Pi\left(\frac{\lambda(\tau)}{\lambda_0} - 1\right)^2 \\
&\text{where } \lambda_0 = \frac{4\pi\mathcal{A}_0}{\mathcal{L}_0^2}, \text{and let } \Pi = \frac{\mathcal{P}}{\mathcal{G}_b(b^c))\mathcal{L}_0/(2\sqrt{\pi})} \\
E_{\text{bending}} &= \frac{\int_0^{\mathcal{L}_0} \frac{1}{2}(\mathcal{M}_a(a(s)) + \mathcal{M}_b(b(s)))\left|\left|\frac{\partial^2\vec{x}}{\partial s^2}\right|\right|^2 ds}{\mathcal{G}_b(b^c)\mathcal{L}_0/(2\sqrt{\pi})} \\
&= \frac{\int_0^{2\sqrt{\pi}} \frac{1}{2}(\mathcal{M}_a(A(S)a^c) + \mathcal{M}_b(B(S)b^c)\left|\left|\frac{2\sqrt{\pi}}{\mathcal{L}_0}\frac{\partial^2\vec{\chi}}{\partial S^2}\right|\right|^2 \frac{\mathcal{L}_0}{2\sqrt{\pi}} dS}{\mathcal{G}_b(b^c)\mathcal{L}_0/(2\sqrt{\pi})} \\
&\text{let } M_A(A(S)) = \frac{4\pi\mathcal{M}_a(A(S)a^c)}{\mathcal{G}_b(b^c)\mathcal{L}_0^2}, M_B(B(S)) = \frac{4\pi\mathcal{M}_b(B(S)b^c)}{\mathcal{G}_b(b^c)\mathcal{L}_0^2} \\
\Rightarrow E_{\text{bending}} &= \int_0^{2\sqrt{\pi}} \frac{1}{2}(M_A(A(S)) + M_B(B(S)))\left|\left|\frac{\partial^2\vec{\chi}}{\partial S^2}\right|\right|^2 dS \\
E_{\text{cytoskeleton}} &= \frac{\int_0^{\mathcal{L}_0} \mathcal{F}_{\text{cyto}}(a(s))\Theta(\theta)||\vec{x}||ds}{\mathcal{G}_b(b^c)\mathcal{L}_0/(2\sqrt{\pi})} \\
&= \frac{\int_0^{2\sqrt{\pi}} \mathcal{F}_{\text{cyto}}(A(S)a^c)\Theta(\theta)\left|\left|\frac{\mathcal{L}_0}{2\sqrt{\pi}}\vec{\chi}\right|\right|\frac{\mathcal{L}_0}{2\sqrt{\pi}} dS}{\mathcal{G}_b(b^c)\mathcal{L}_0/(2\sqrt{\pi})} \\
&\text{let } F_{\text{cyto}}(A(S)) = \frac{\mathcal{F}_{\text{cyto}}(A(S)a^c)\mathcal{L}_0}{2\sqrt{\pi}\mathcal{G}_b(b^c)}
\end{aligned}
$$

$$\Rightarrow E_{\text{cytoskeleton}} = \int_0^{2\sqrt{\pi}} F_{\text{cyto}}(A(S))\Theta(\theta)\,||\vec{\chi}||\,dS$$

$$\text{let } k_BT = \frac{k_B\mathcal{T}}{\mathcal{G}_b(b^c)\mathcal{L}_0/(2\sqrt{\pi})}$$

$$\Rightarrow E = E_{\text{stretch}} + E_{\text{pressure}} + E_{\text{bending}} + E_{\text{cytoskeleton}} + k_BT\xi$$